

Mesoscale Study of Tropical Sub-Cloud Layer

By
Omar Ruiz

Department of Atmospheric Science
Colorado State University
Fort Collins, Colorado

September 1975



**Department of
Atmospheric Science**

Paper No. 237

MESOSCALE STUDY OF THE TROPICAL SUB-CLOUD LAYER

BY

Omar Ruiz

Department of Atmospheric Science

Colorado State University

Fort Collins, Colorado

80523

September, 1975

Atmospheric Science Paper No. 237

ABSTRACT

MESOSCALE STUDY OF THE TROPICAL SUB-CLOUD LAYER

Aircraft, rawinsonde, radar, rainfall, synoptic data acquired during the 1972 Venezuelan International Meteorological and Hydrological Experiment (VIMHEX 1972) are used to study both undisturbed and disturbed conditions. Horizontal divergences calculated from aircraft wind measurements on undisturbed days at 850 mb were as small as the errors in the measurements. In the cloudy areas penetrated by the aircraft, the wind, humidity and temperature were found well correlated and their variability are probably representative of mesoscale patterns in the tropics. The associated variations in the above parameters were significant and measurable even in relatively undisturbed conditions. They show evidence for coupling between the cloud layer and the sub-cloud layer.

A meso-synoptic disturbance on September 1-2, 1972 centered on the data network area is analyzed in detail. Serial rawinsondes combined with research aircraft data show dramatic vertical transports through cloud base; and the drying and stabilization of the sub-cloud layer by downdrafts.

A structure of the system which permitted unsaturated, rain cooled, downdrafts, similar to that documented by Zipser, 1969, is proposed.

ACKNOWLEDGEMENTS

The author wishes to express his most sincere gratitude to Dr. Alan K. Betts for proposing and directing this research and giving countless hours of guidance and encouragement. Dr. W. Schubert and Dr. M. A. Stevens served on his M.S. Committee and offered encouragement. Additional appreciation is extended to Ms. Julia Ruiz, Ms. Susan Kuehl, Ms. Polly Martin and Mr. Rick Miller for their invaluable assistance in the manuscript typing, data reduction and computer programming.

The author is grateful to the Venezuelan Air Force for the school assignment which provided the opportunity for this research to be done.

This research was supported by the Global Atmospheric Research Program of the National Science Foundation under Grant OCD72-01406. The VIMHEX II field experiment was additionally supported by the office of Naval Research under Contract No. 014-68A-0493-002, the Facilities Laboratory of the National Center for Atmospheric Research, and the Meteorological Service of the Venezuelan Air Force.

TITLE:

MESOSCALE STRUCTURE OF THE TROPICAL SUB-CLOUD LAYER

TABLE OF CONTENTS

	<u>PAGE</u>
ABSTRACT	iii
ACKNOWLEDGEMENTS	v
TABLE OF CONTENTS	vi
LIST OF TABLES	viii
LIST OF FIGURES	ix
SYMBOL LIST	xiii
1. INTRODUCTION	1
1.1 General	1
1.2 Previous Studies	2
1.3 Objective and Content of this Thesis	4
2. THE EXPERIMENT	6
2.1 General Considerations	6
2.2 Synoptic Climatology of Summer 1972 at Carrizal	10
2.3 The Queen Air Aircraft and Instrumentation	22
2.4 Aircraft Data Reduction and Corrections	28
3. ANALYSIS AND RESULTS OF DATA COLLECTED AT MESOSCALE	36
3.1 Introduction	36
3.2 Single Station Analysis for the Days Chosen	38
3.3 The Aircraft Data	59
4. MESOSYNOPTIC STRUCTURE OF SEPTEMBER 1-2 DISTURBANCE	101
4.1 Introduction	101
4.2 The September 1-2 Disturbance	101
4.3 Synoptic Situation	102
4.4 Storm Structure	105

TABLE OF CONTENTS

	<u>PAGE</u>
4.5 Sub-Cloud and Upper Layer Winds	109
4.6 Structure of the Rain-Cooled Air	109
4.7 The Downdraft and Its Associated Convective Systems	116
5. SUMMARY AND CONCLUSIONS	123
REFERENCES	127
APPENDIX	130

LIST OF TABLES

<u>TABLE</u>	<u>PAGE</u>	
2.1	Convective regimes and rainfall for VIMHEX II.	20
2.2A	Queen Air specifications.	23
2.2B	Basic meteorological instrumentation aboard the Queen Air.	24
3.1	Echo and precipitation data during the aircraft mission periods.	46
3.2	Date, time, prevailing conditions and soundings launched during the aircraft mission periods.	63
3.3	Values of horizontal divergence and vorticity determined from aircraft measurements on the August days.	67
3.4A-E	Mean and standard deviation of θ , θ_e , r and wind (direction and speed) at 850 mb from the aircraft measurement missions (August 21, 22, 29, 30 and September 1).	84 to 88

LIST OF FIGURES

<u>FIGURE</u>		<u>PAGE</u>
1.1	Model sub-cloud layer structure for undisturbed conditions suggested by VIMHEX II data (Dugan, 1973).	3
2.1	Location of Headquarters during VIMHEX II.	6
2.2	Area covered by radar and location of different raingauges in and adjacent to the study area.	8
2.3	Comparison of monthly mean θ for the months of June, July, August and six days of September.	11
2.4	Comparison of monthly mean θ_e for the months of June, July, August and six days of September.	12
2.5	Comparison of monthly mean mixing ratio (r) for the months of June, July, August and six days of September.	13
2.6	Comparison of monthly mean u and v components of the wind for June, July, August and six days of September.	14
2.7a-d	Comparison of mean monthly hodographs for June, July, August and six days of September.	15-16
2.8a	Comparison between reverse flow potential temperature (θ_{RF}) and the Rosemount potential temperature (θ_P).	29
2.8b	Comparison between reverse flow potential temperature (θ_{RF}) and the potential temperature (θ_S) of the sounding.	29
2.9	Correction curves used to correct the aircraft data to 850 mb.	32
2.10	Wind velocity triangles for before and after a sharp change in aircraft heading, showing how instrumentation errors affect their geometry. The measured wind velocities, W_{m1} and W_{m2} , are found to differ following a sharp turn, but the actual wind, W , remains the same (for legend of symbols, see List of Symbols).	33
3.1	Vertical and time variation of the potential temperature (θ), equivalent potential temperature (θ_e), mixing ratio (r), and cloud base for August 21.	39
3.2	Vertical and time variation of the potential temperature (θ), equivalent potential temperature (θ_e), mixing ratio (r), and cloud base for August 29.	40
3.3a	Vertical and time variation of the potential temperature (θ), equivalent potential temperature (θ_e), mixing ratio (r), and cloud base for September 1.	41

LIST OF FIGURES - Continued

<u>FIGURE</u>		<u>PAGE</u>
3.3b	Vertical and time variation of the potential temperature (θ), equivalent potential temperature (θ_e), mixing ratio (r), and cloud base for September 2.	42
3.4a	1400-1500 hourly echo and average rainfall composite chart for August 21.	47
3.4b	1500-1600 hourly echo and average rainfall composite chart for August 21.	47
3.4c	1600-1700 hourly echo and average rainfall composite chart for August 21.	48
3.4d	1700-1800 hourly echo and average rainfall composite chart for August 21.	48
3.4e	1800-1900 hourly echo and average rainfall composite chart for August 21.	49
3.4f	Daily echo and average rainfall composite chart for August 21.	50
3.5a	1200-1300 hourly echo and average rainfall composite chart for August 29.	51
3.5b	1300-1400 hourly echo and average rainfall composite chart for August 29.	51
3.5c	1400-1500 hourly echo and average rainfall composite chart for August 29.	52
3.5d	1500-1600 hourly echo and average rainfall composite chart for August 29.	52
3.5e	Daily echo and average rainfall composite chart for August 29.	53
3.6a	1400-1500 hourly echo and average rainfall composite chart for September 1.	54
3.6b	1500-1600 hourly echo and average rainfall composite chart for September 1.	54
3.6c	1600-1700 hourly echo and average rainfall composite chart for September 1.	55
3.6d	1700-1800 hourly echo and average rainfall composite chart for September 1.	55
3.6e	Average daily isohyct chart and maximum area of the radar echo for September 1.	56

LIST OF FIGURES - Continued

<u>FIGURE</u>		<u>PAGE</u>
3.7	Average daily isohyct chart and maximum area of the radar echo for September 2.	57
3.8	Scales and geographical situation for the north-south ($\cdot\cdot \text{---}$), circle (---) and cloverleaf (---) aircraft patterns.	61
3.9	Conventional notation for the aircraft cloverleaf pattern used in the horizontal divergence and vorticity calculations.	64
3.10	Graphical linear interpolation used at each corner of the aircraft cloverleaf pattern in the horizontal divergence and vorticity calculations.	65
3.11a	Streamlines analysis for August 21.	70
3.11b	Mixing ratio analysis for August 21.	71
3.12a	Streamlines analysis for August 22.	72
3.12b	Mixing ratio analysis for August 22.	73
3.13a	Streamlines analysis for August 29.	74
3.13b	Mixing ratio analysis for August 29.	75
3.14a	Streamlines analysis for August 30.	76
3.14b	Mixing ratio analysis for August 30.	77
3.15a	Streamlines analysis for September 1.	78
3.15b	Mixing ratio analysis for September 1.	79
3.16	Conventional notation for the aircraft cloverleaf pattern used in the study of the variability of θ , θ_e , r and wind (direction and speed) at ~ 850 mb.	82
3.17	Variations of T , θ , θ_e , r and relative wind as measured by the aircraft through clouds and rain at 850 mb on August 21 (1740-1758 LST).	92
3.18	As above (3.17) for August 21 (1800-1813 LST).	94
3.19	As above (3.17) for August 29 (1316-1325 LST).	96
3.20	As above (3.17) for September 1 (1715-1725 LST).	98

LIST OF FIGURES - Continued

<u>FIGURE</u>		<u>PAGE</u>
4.1	Height pattern on 200 mb surface at 1200 Z (0800 LST) September 1, 1972.	103
4.2	As above (4.1) for 500 mb surface.	103
4.3	As above (4.1) for 850 mb surface.	104
4.4	Height pattern on 200 mb surface at 0000Z (2000 LST) September 1, 1972.	106
4.5	As above (4.4) for 500 mb surface.	106
4.6	As above (4.4) for 850 mb surface.	107
4.7	Height pattern on 200 mb surface at 1200 Z (0800 LST) September 2, 1972.	107
4.8	As above (4.7) for 500 mb surface.	108
4.9	As above (4.7) for 850 mb surface.	108
4.10a	Half hourly average values of wind (direction and speed) and pressure at the surface at Carrizal from 1200 LST (September 1) to 1200 LST (September 2).	110
4.10b	Half hourly average values of temperature and relative humidity at the surface at Carrizal for the above times.	111
4.10c	Accumulative rainfall at the surface at Carrizal for the above times.	112
4.11	Time cross-section at Carrizal from 1000 LST (September 1) to 1707 LST (September 2).	113
4.12	Variations of the wind (direction and speed) as measured by the aircraft during a north-south flight carried out on September 2.	115
4.13	Vertical and time variation of θ and θ_e before and after the September 1-2 mesosynoptic disturbance in a tephigram.	117
4.14	Schematic structure of cloud system illustrating the mechanism of production of large scale downdrafts.	121

LIST OF SYMBOLS

T	Temperature
θ	Potential temperature
θ_e	Equivalent potential temperature
θ_{es}	Saturation equivalent potential temperature
r	Mixing Ratio
θ_{RF}	Reverse flow potential temperature
θ_R	Rosemount potential temperature
LCL	Lifting Condensation Level
RH	Relative humidity
$ \overrightarrow{TAS} $	True airspeed (magnitude)
$ \overrightarrow{IAS} $	Indicated airspeed (magnitude)
ρ_0	Standard density
ρ	Density
T_{amb}	Ambient temperature
T_{rec}	Recovery temperature
T_s	Static temperature
T_t	Total temperature
rf	Recovery factor
T_e	Standard temperature
P	Ambient (absolute) pressure
P_e	Standard Pressure
\vec{W}	(Actual) wind vector
\overrightarrow{TAS}	True airspeed vector
\overrightarrow{GS}	Ground speed vector
$\overrightarrow{T_c}$	True airspeed correction vector
$\vec{\delta}_c$	Drift angle correction vector

LIST OF SYMBOLS - Continued

δ	Drift angle in degrees ($\delta > 0$ - for right drift)
δ_c	Drift angle correction in degrees
δ_m	Measured drift angle in degrees
TR	Track angle in degrees
THdg	True heading in degrees
MHdg	Magnetic heading in degrees
VAR	Magnetic variation in degrees
Subscript "1"	Refers to leg "1"
Subscript "2"	Refers to leg "2" (reciprocal)
Subscript "m"	Measured or recorded
∇_h	Two-dimensional divergence operator
ϵ	Perimeter
A	Area
V_n	Horizontal component of the wind normal to the perimeter (ϵ)
V_τ	Horizontal component of the wind tangent to the perimeter (ϵ)
t	Time

1. INTRODUCTION

1.1 General

In the tropical atmosphere, the boundary layer is defined as a region in which dynamical and thermodynamic effects of the surface can be measured. Depending on the weather conditions, the extent of the boundary layer may vary. Thus, it is convenient to differentiate between undisturbed and disturbed conditions. During the former, the boundary layer extends from the surface to the trade wind inversion while in the latter the situation is quite different. In disturbed conditions, cloud-induced mixing reaches below cloud base and may couple sea-land surface processes with the high troposphere (Garstang and Betts, 1974). By this definition, the boundary layer can include both processes at the air-surface (land-sea) interface and cumulus convection extending through the entire tropical troposphere. This introduction does not attempt to cover such field. Instead, it does concentrate on work that deals with the interaction between the cloud layer and the underlying subcloud layer and surface.

The structure of the sub-cloud layer for the undisturbed trade wind atmosphere has been documented by Riehl et al (1951), Malkus (1956), while Dugan (1973) has shown the occurrence of a similar structure over Venezuela.

The sub-cloud layer can be divided into three sub-layers. The lowest is the constant flux layer and is located in the first tens of meters above the earth's surface. Here, fluxes of vertical momentum, latent, and sensible heat are considered constant with height. Extending from this layer up to approximately 500 m in the sub-cloud layer is the mixed layer. This is so named because the temperature lapse rate is nearly dry adiabatic and the vertical gradient of water vapor mixing ratio is nearly zero. Topping the

mixed layer and extending into the lower cloud layer is the transition layer. This is characterized by almost constant temperature distribution and decrease of moisture.

1.2 Previous Studies

In recent years, emphasis on the structure and function of the sub-cloud layer has shifted from undisturbed to disturbed atmospheric states. It has been observed (Garstang, 1967) that fluxes of sensible and latent heat from the sea increase significantly during disturbances. At the same time, Riehl (1968) has suggested that the convergence in the sub-cloud layer fields associated with traveling disturbances serves to concentrate energy, which was acquired from the sea at an earlier time, in such a way as to make it available to the disturbance. It has also been suggested that downdrafts associated with these disturbances can modify the sub-cloud layer so that it is no longer a source of energy for the disturbance.

Results obtained from BOMEX (1969) and the South Florida Seeding Experiment of 1971 have shown how the dynamic and thermodynamic structure of the sub-cloud layer change when cloud convective activity increases. Those studies among many others have not yet shown the extent of the differences between the continental and oceanic sub-cloud layers.

Dugan (1973) and Betts et al (1974) in an observational study based on VIMHEX II, report clear evidence of cloud "roots" in the sub-cloud layer. In Fig. 1.1, Dugan presents evidence of modification of the subcloud layer by convection. It is important to note that from this report, the mixed layer characterized by constant θ is in fact, slightly unstable during most of the convective period below Z^* and becomes stable above Z^* . From the above studies, it would seem that the structure of the sub-cloud layer and the character of the sea surface may be controlled by interaction with

the cloud layer. However, Pennell and Lemone (1974) have observed, in a study of moderately cloudy areas (roughly 40 km in width), a layer of strong wind shear near cloud base. This, coupled with corresponding minima in the turbulence quantities, suggests a weak coupling, on the turbulence scale, between the cloud and sub-cloud layers.

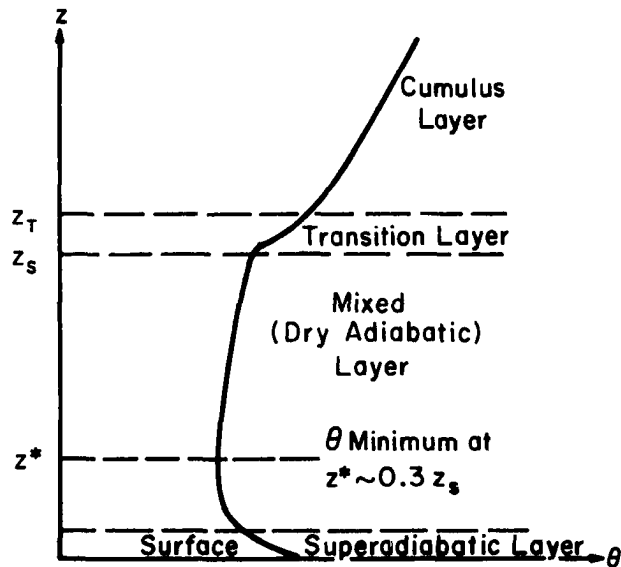


Figure 1.1 Model sub-cloud layer structure for undisturbed conditions suggested by VIMHEX II data (Dugan, 1973).

Models for a well mixed convective sub-cloud layer have recently experienced a period of rapid development. Betts (1971, 1973a), Deardorff (1972), Tennekes (1973), and Carson (1973) have all proposed mixed layer models based on earlier works by Ball (1960) and Lilly (1968). These models have shown how the height of the convective boundary layer is controlled in the absence of precipitation primarily by large-scale subsidence and the radiative and surface fluxes.

Arakawa and Schubert (1974) have modified the model of Betts for use in their cumulus ensemble parameterization theory. They distinguish mixed layer height from cloud-base height, since in their theory, the cloud base mass flux (and cloud population) are determined by an integral constraint

over the whole cloud layer, whereas Betts (1973a) determined the convective mass flux through cloud base by a cloud-base boundary condition.

No adequate model exists for the transformation of the sub-cloud layer by precipitating convection primarily because the precipitation process and the downdraft circulation process are only now being observationally described and adequately understood.

1.3 Objective and Content of this Thesis

The purpose of the research presented here is to provide modelers of the tropical atmosphere with information of the mesoscale structure and variation of the sub-cloud layer observed during the Second Venezuelan International Meteorological and Hydrological Experiment (VIMHEX II) in 1972.

There are three main objectives of this study. The first objective is to describe the structure and characteristics of the mesofield at the top of the sub-cloud layer during both disturbed and undisturbed conditions by the use, mainly, of aircraft data. In addition, the local state of the atmosphere could be specified by rainfall recorded within the experimental area scanned by a 10 cm calibrated weather radar and by rawinsonde soundings.

The second objective is to utilize the data for comparison with similar measurements from sounding data. The above comparison helps to validate the measurements presented herein.

The third objective is to present the meso-synoptic structure of a rather strong disturbance observed over Venezuela on September 1-2, 1972, as well as the role of organized convective downdrafts.

Details of the experiment (VIMHEX II) from which the data were extracted, as well as a description and correction of the different sources of data are the subject of Chapter 2. The chapter also includes a summary of the "Synoptic Climatology" for the experimental time period.

Chapter 3 deals with the mesoscale structure, the time dependence and significance of the variability of different measured parameters in the sub-cloud layer. A section containing comments about thermodynamic and dynamic features at cumulus-scale has also been included.

In Chapter 4, a well-documented example of the heaviest rainfall of summer 1972 (mentioned earlier) is described.

2. THE EXPERIMENT

2.1 General Considerations

The Second Venezuela International Meteorological and Hydrologic Experiment (VIMHEX II) was conducted from June to early September, 1972. Headquarters were located at Carrizal, ($9^{\circ}22.8'$ N and $66^{\circ}55.0'$ W), and at Maracay ($10^{\circ}15'$ N and $67^{\circ}39'$ W), in the north central section of the country, approximately 150 km southwest of Caracas, Venezuela (Fig.2.1).

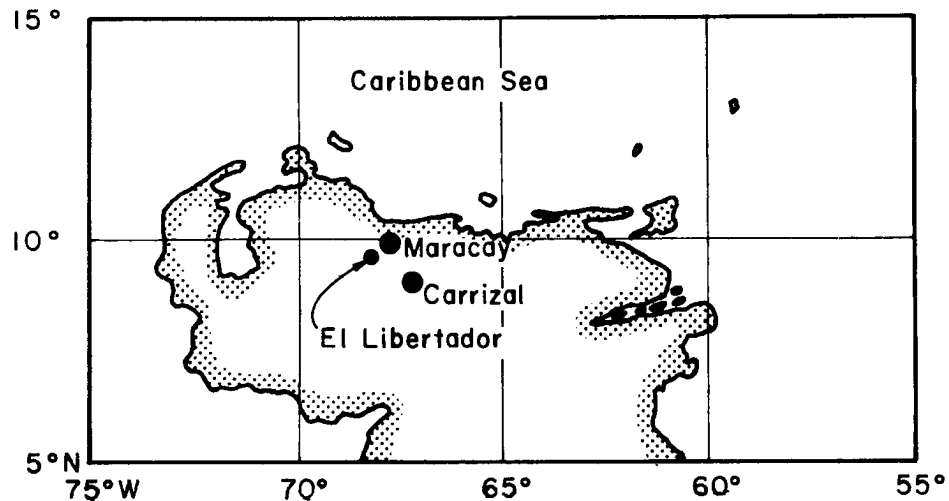


Figure 2.1 Location of Headquarters during VIMHEX II.

Located at Carrizal were a GMD-1 radiosonde unit and modified 10 cm M-33 radar with a 2° beam width and return signal attenuation capabilities. The radiosonde soundings were the principle means of measuring the state of the atmosphere. For this, the new VIZ-National Weather Service 1290 series radiosonde was used. Riehl and Betts (1972) and Betts et al (1974) have shown that this new instrument has overcome the systematic humidity errors found to exist in the old model used in VIMHEX I (carried out in northeastern Venezuela during June to September 1969). There were 327 soundings taken which fall into three categories:

1. Routine soundings taken on a twice-daily basis.
2. Sequences of soundings taken on several days when convection was suppressed.
3. Special soundings which were made before, during and after each convective precipitation event.

The radar system consisted of an observer and camera scope system set at a horizontal range of 90 km. At the first sign of cumulonimbus convection, the camera scope was activated and the radar was operated in a continuous sweep PPI mode with a base sweep of 2° in elevation. A data acquisition sequence lasting approximately five minutes was started every fifteen minutes. The sequence consisted of photographing a calibrated 10-inch diameter scope at a series of elevation steps beginning at a base elevation of 2° and a series of signal attenuations. This information was recorded on 35 mm film. The data were reduced by projecting the film on a microfilm reader to a scale of 1 cm to 10 km. By tracing the individual echo perimeters at 2° and zero return attenuation at each fifteen minute interval a composite of the storm system as it moved across the field of observation was obtained.

The rainfall which occurred over the area covered by radar was estimated from rainfall collected in a network of raingauges. Daily rainfall at 69 locations was collected. Daily rainfall over the area, and at 17 locations values for the amount of rainfall occurring in five minute intervals were tabulated. In order to estimate the average daily rainfall over the study region, two precipitation indices were computed daily from the raingauge data collected each morning. They are the line precipitation index and the area precipitation index. For details, see Betts and Stevens (1974).

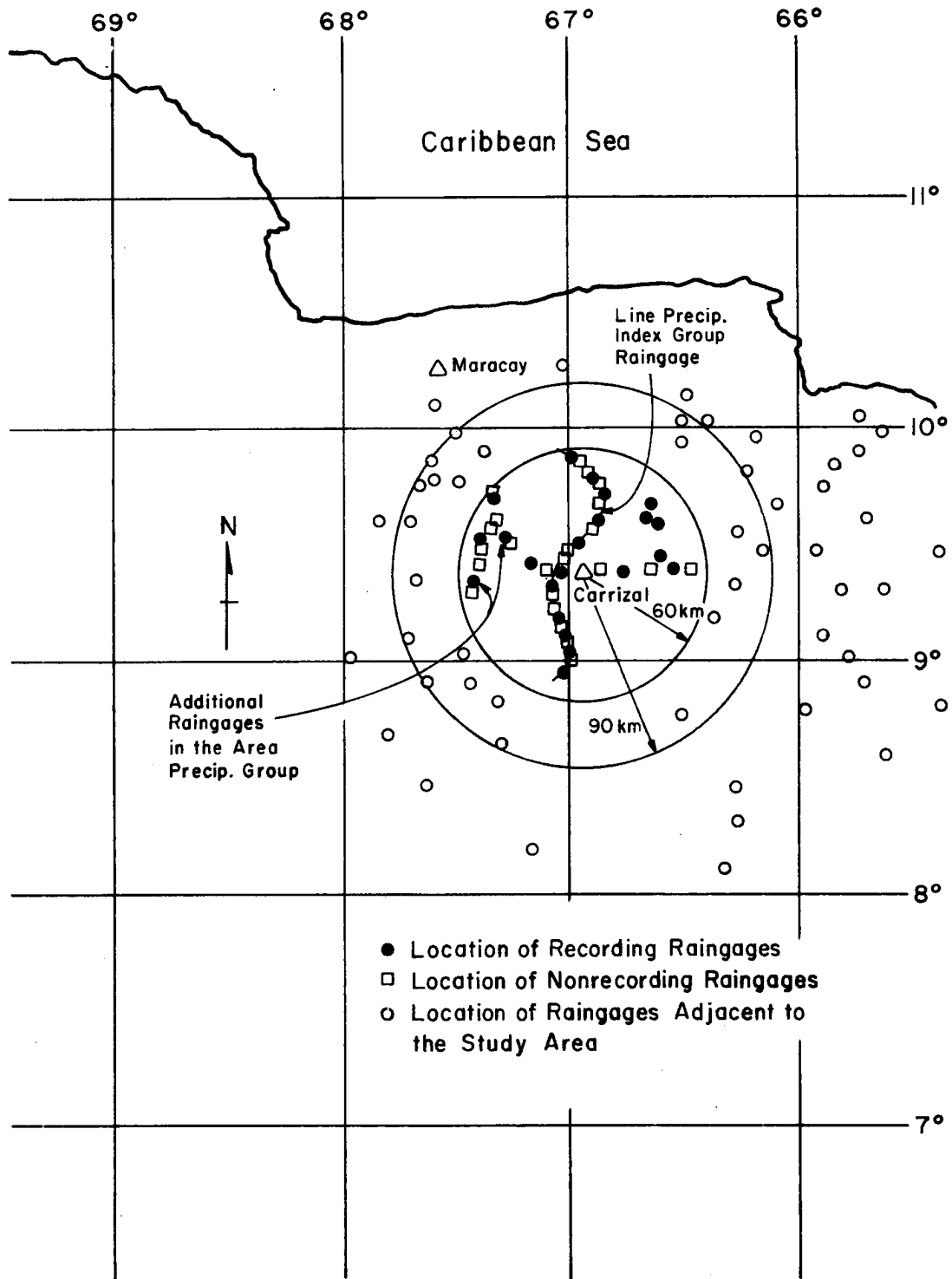


Figure 2.2 Area covered by radar and location of different raingages in and adjacent to the study area.

Figure 2.2 shows the area covered by radar and the location of different raingauges in and adjacent to the study area. Indicated also are the raingauges used to compute the above indices.

The operation center for the NCAR Queen Air aircraft N306D and Sabreliner N307D was located near Maracay, at the Venezuelan Air Force Base "El Libertador" (Fig. 2.1) from July 29 to September 6 of 1972 carrying out twenty-eight and fifteen missions, respectively.

The observations for this study were taken from the data collected at Carrizal (radiosonde, radar and rainfall), at Maracay (satellites and synoptic charts) as well as the NCAR Queen Air aircraft N306D data. The Sabreliner N307D data (at 300 mb) were not used because this study is concentrated on the sub-cloud layer. (The N307D data was also limited by frequent system failures.)

2.2 Synoptic Climatology of Summer 1972 at Carrizal

Statistical summaries of the main variables and comparisons of means in time and space are presented in this section.

Because the months of June, July and August were abnormally dry, those months and September (six days) have been treated separately.

2.2.1 Representativeness of the Study Period.

The annual average rainfall for Carrizal is about 1200 mm. The rainy season occurs during May through October averaging 160-200 mm per month and the dry season during November through April with 25-75 mm per month.

The June, July and August rainfall 1972 were the lowest recorded for each of those months since 1960. The extreme month was August 1972, when slightly more than 60 mm fell, which is approximately 100 mm below average.

2.2.2 Mean Monthly Values of Main Variables.

The method used was to select a time of day, 1000 LST, as a reference time and consider a sounding taken within a certain interval of that time, say 0900-1100 LST as a reference sounding. A sounding was normally taken at about 1000 LST every day.

Figure 2.3 shows a comparison of the 1000 LST monthly mean potential temperature (θ) for the months of June, July, August and the six days of September.

Figure 2.4 as above (2.3) for the equivalent potential temperature (θ_e).

Figure 2.5 as above (2.3) for the mixing ratio (r). Figure 2.6 as above (2.3) for the u and v components of the wind and Figure 2.7A to 2.7D shows the monthly mean wind hodographs for the months of June, July, August and the six days of September.

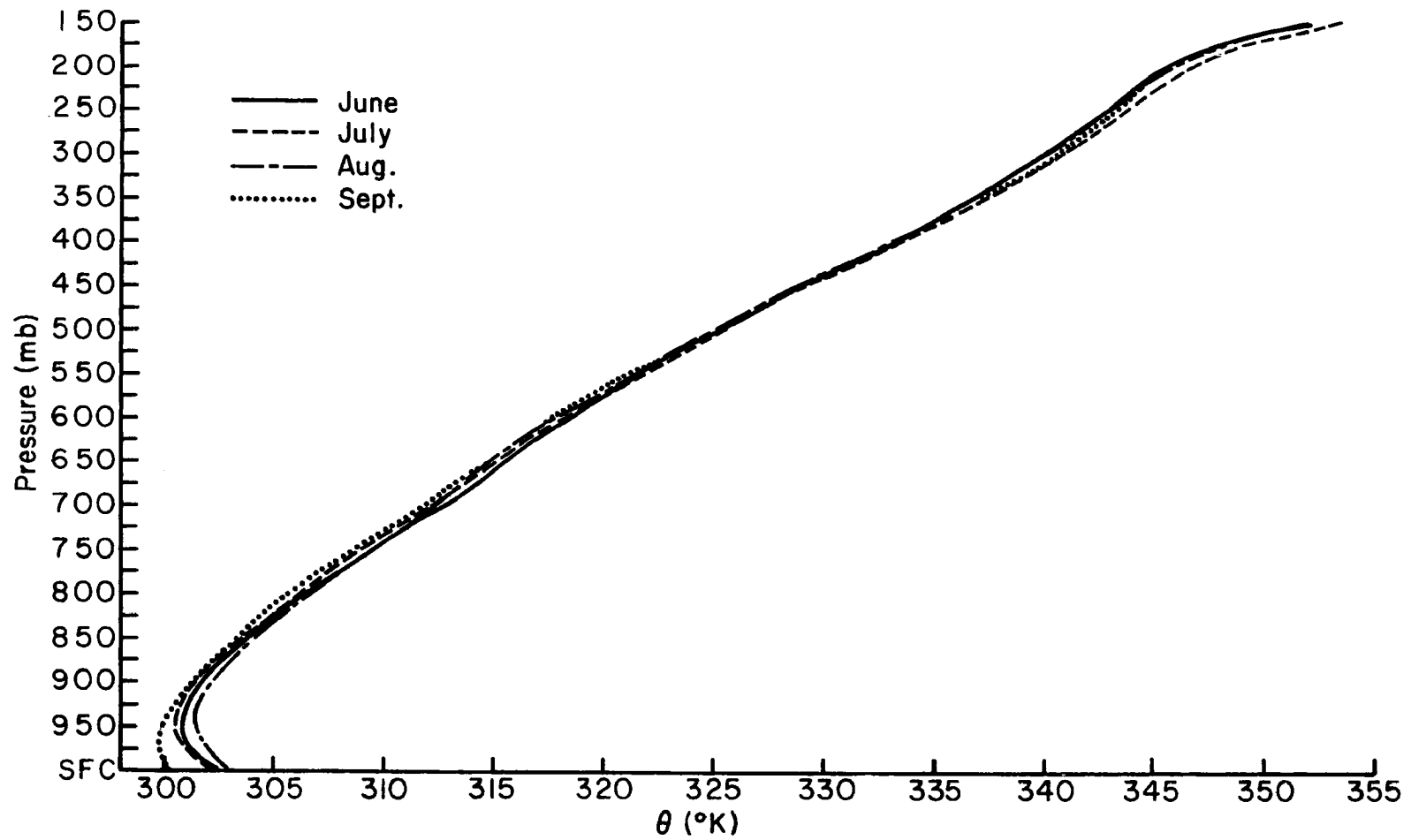


Figure 2.3 Comparison of monthly mean θ for the months of June, July, August and six days of September.

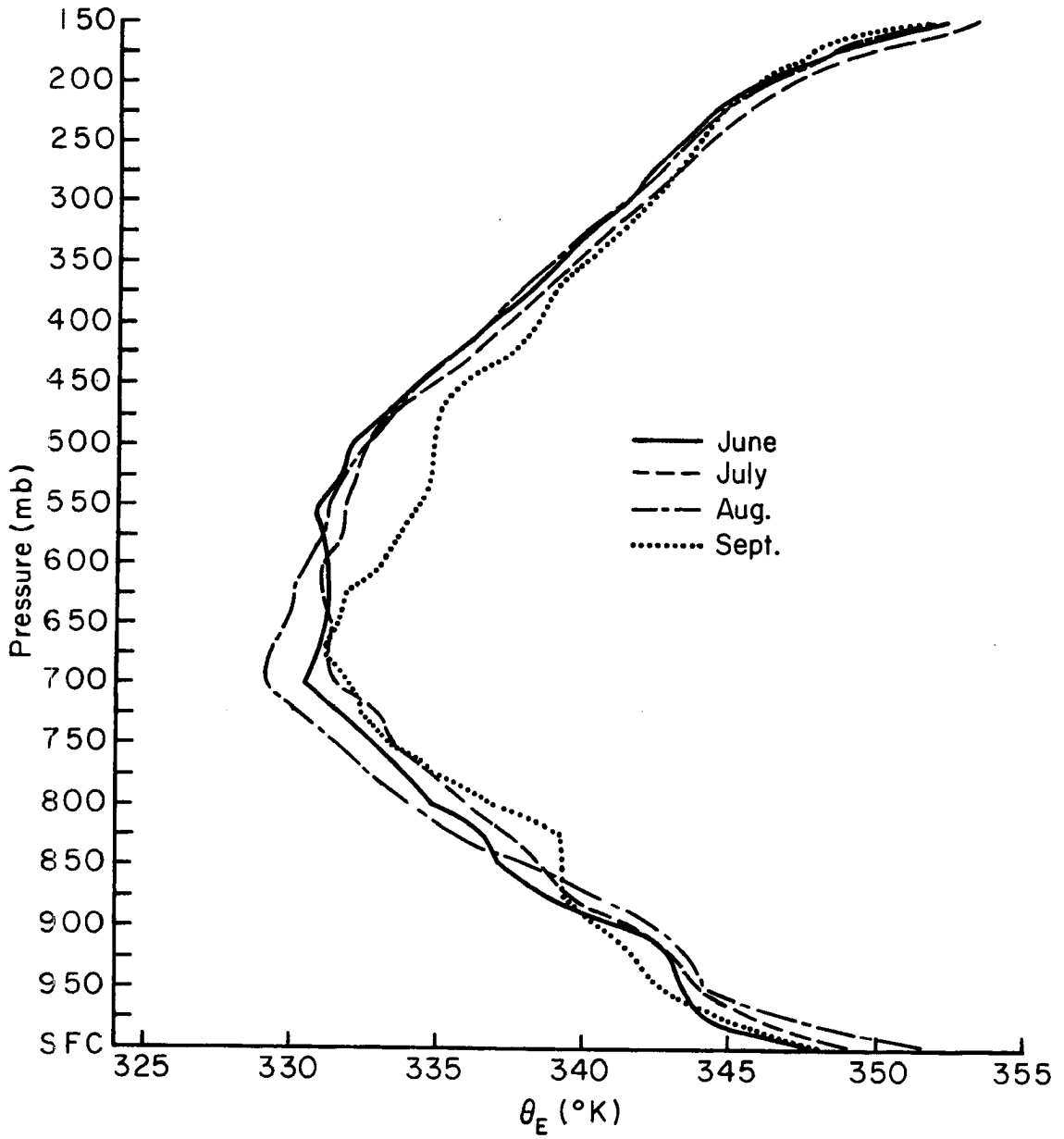


Figure 2.4 Comparison of monthly mean θ_e for the months of June, July, August and six days of September.

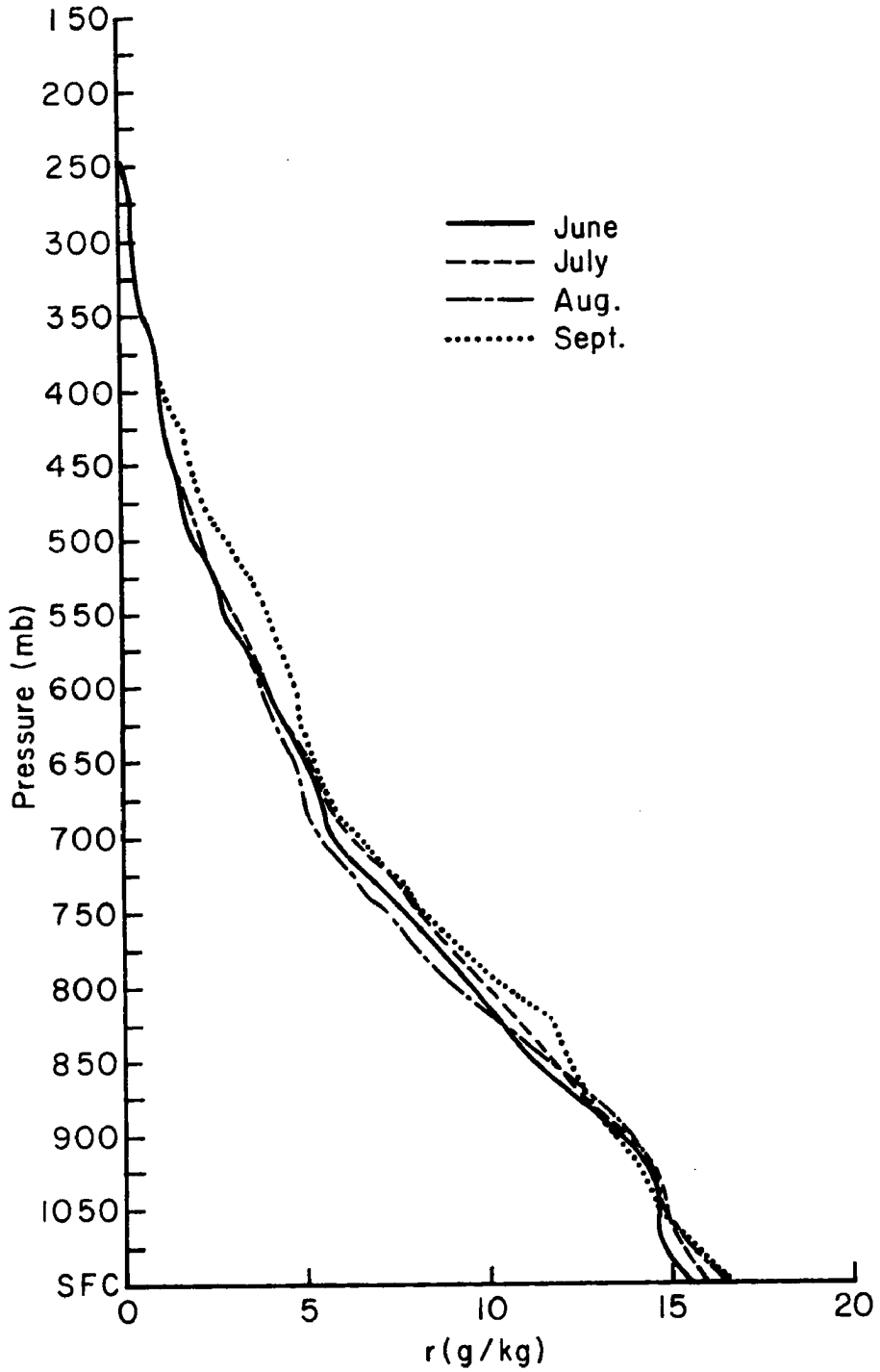


Figure 2.5 Comparison of monthly mean mixing ratio (r) for the months of June, July, August and six days of September.

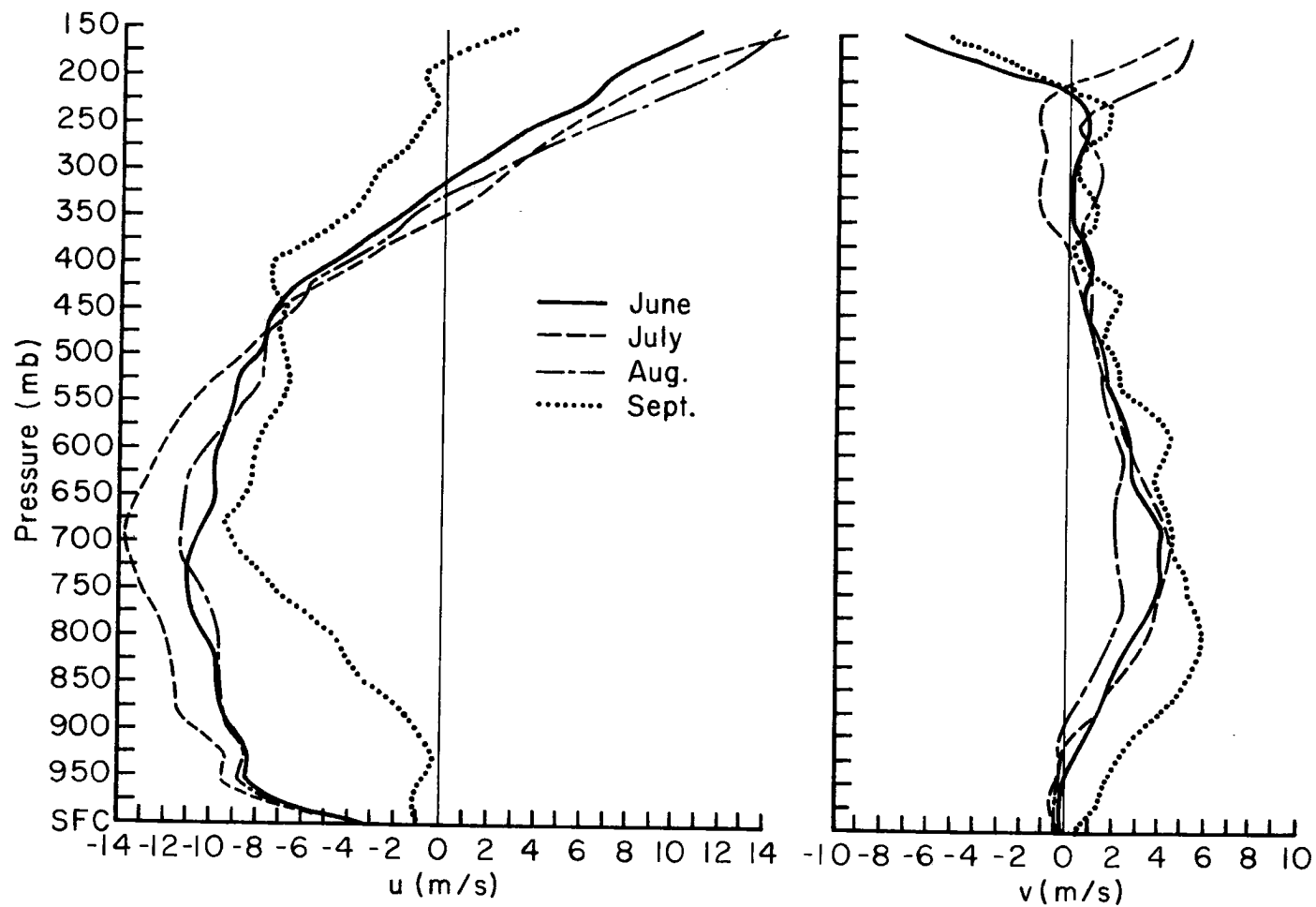


Figure 2.6 Comparison of monthly mean u and v components of the wind for June, July, August and six days of September.

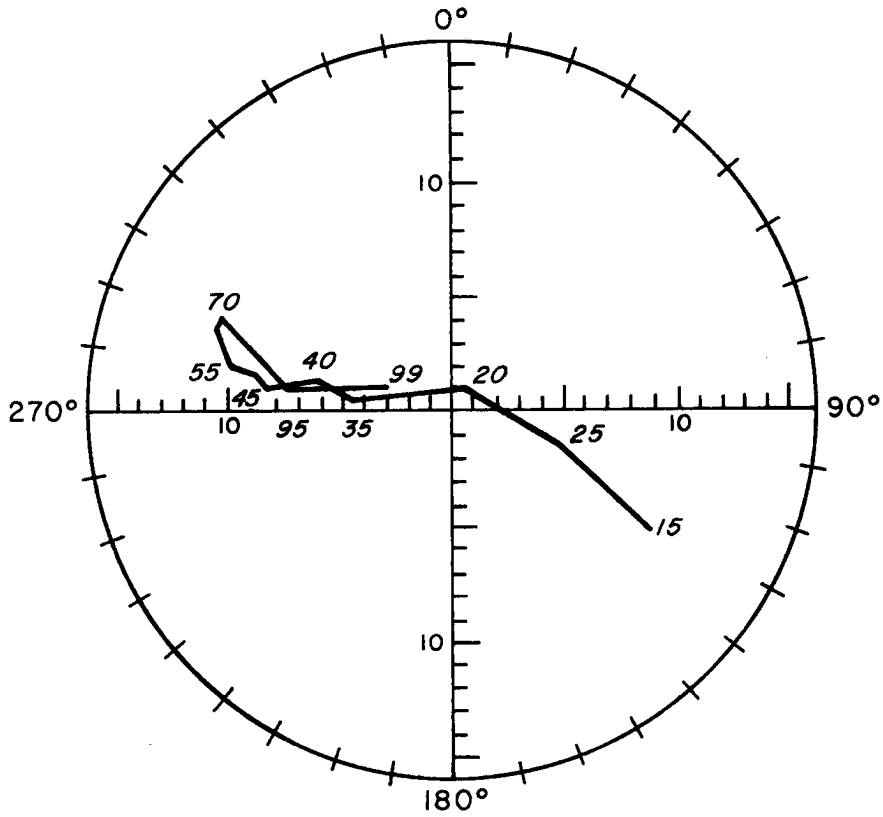


Fig. 2.7a
June

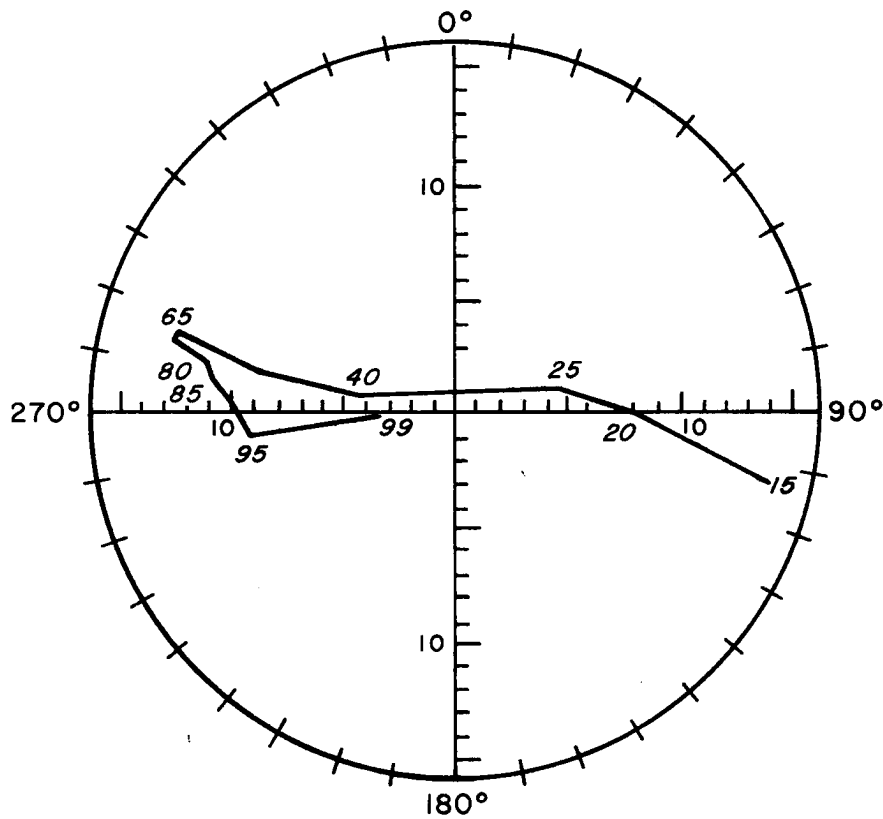


Fig. 2.7b
July

Figures 2.7a & b Comparison of mean monthly hodographs for June and July.

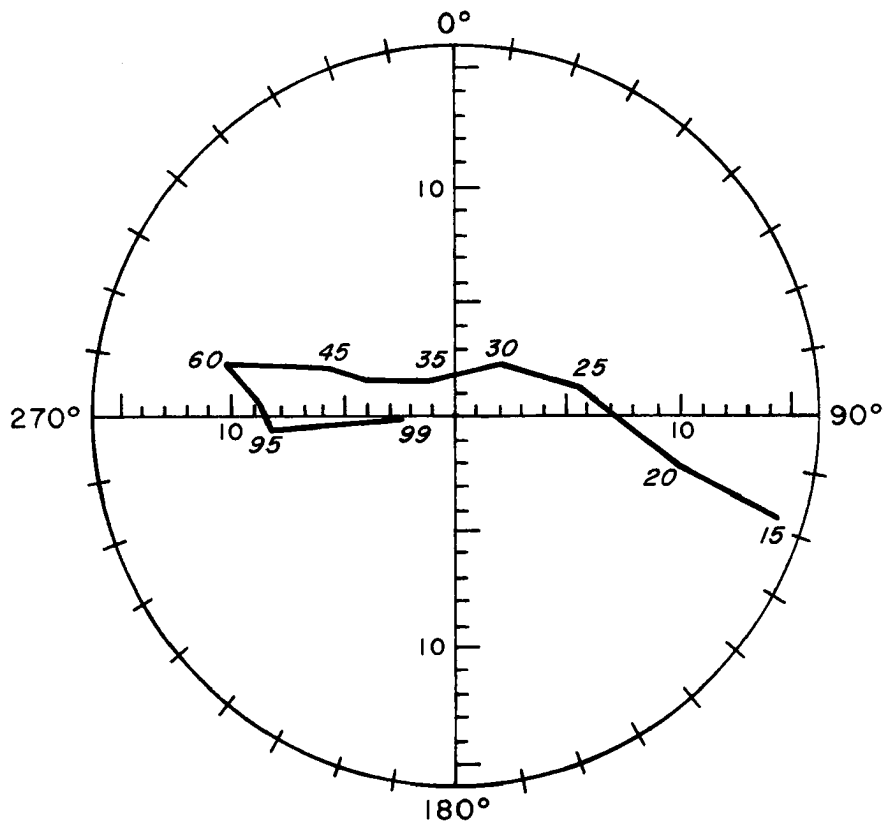


Fig. 2.7c
August

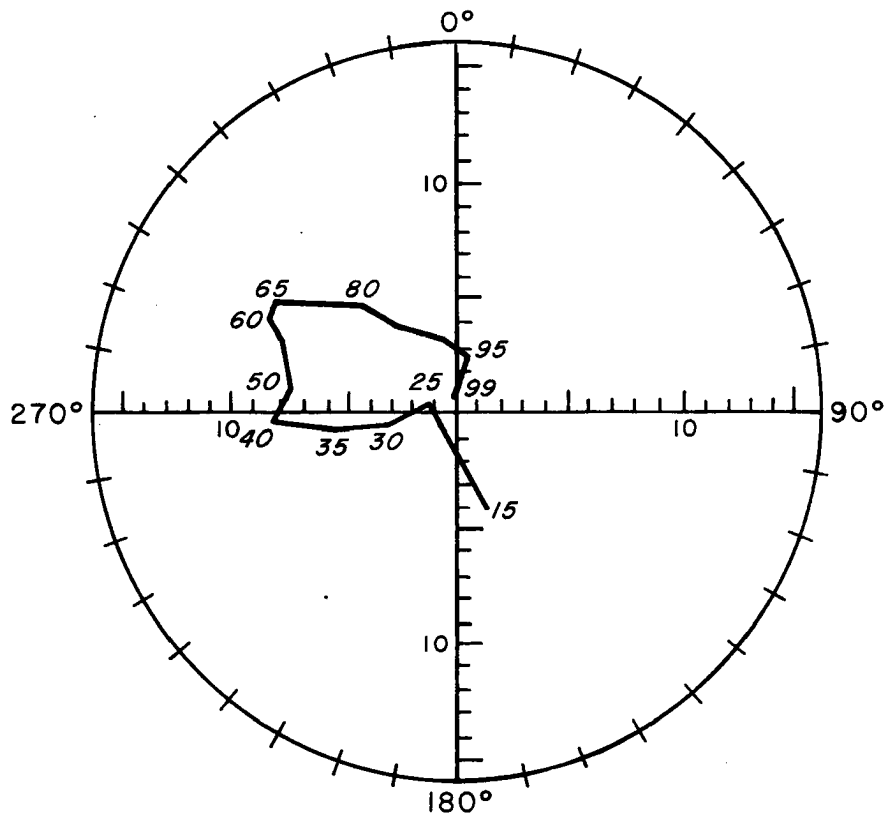


Fig. 2.7d
September

Figure 2.7c & d Comparison of mean monthly hodographs for August and six days of September.

The most striking differences in these variables for the above time periods are:

i) The potential temperature shows an increase in the lowest layers from June to August up to 800 mb while September, for the same layer, shows a decrease of 2°K. From 800 mb up to 150 mb there is no significant difference in this variable for the four months.

ii) The θ_e shows an increase at surface from June to September and then a decrease in all months up to 625 mb where an increase is observed in all months up to 150 mb. Of significance is the observed decrease of θ_e in the month of August from 825 mb to 575 mb and the increase in θ_e in the six days of September from 675 mb up to 300 mb. The former is associated with the lowest recorded rainfall during the month of August, while the latter is associated with the increase of precipitation during that period.

iii) At the surface, there is an increase in the mixing ratio from June to September. From 825 mb to 585 mb, the month of August shows a similar feature to the equivalent potential temperature as well as the six days of September from 850 mb to 380 mb.

iv) From surface to 340 mb, easterly winds are observed from June to August. The six days of September show easterly winds up to 180 mb. Above these levels, up to 150 mb, westerly winds are observed for the above time periods. The observed decrease in the wind below 450 mb and the increase above up to 200 mb for the six days of September is noticeable in comparison with the months of June, July and August.

Northerly wind components are observed in June, July and August from surface to 960 mb, 910 mb and 885 mb respectively. From those levels up to 215 mb, 375 mb and 150 mb, southerly wind components are observed for the same mentioned months. The month of July shows a northerly component

from 375 mb to 200 mb and after that a southerly component is observed. The month of June shows a northerly component from 215 mb up to 150 mb and finally, the six days of September show a southerly component from surface to 215 mb and from there to 150 mb a northerly component is observed.

2.2.3 Observed Storm Parameters and Mean Storm Statistics During the Period June 19, 1972 to September 6, 1972

2.2.3A Observed Storm Parameters

Several storm parameters were determined for the above period (Betts and Stevens, 1974). They are defined briefly next:

- i) The start time of the echo is the local time at which the echo was first recorded by the radar data acquisition system.
- ii) The peak time of the echo is the local time when the storm was estimated to have reached "peak" activity.
- iii) The end time of the echo is the local time of the last visible radar echo from the storm.
- iv) The echo lifetime is the difference between the end time and start time of the echo.

The initial and final location of the echo are described by the azimuth (degree clockwise centroid from north) and horizontal range of the echo centroid. These initial and final locations were chosen so that the vector joining them is representative of the mean echo track and velocity over its lifetime. Thus, the local time of initial and final location differ occasionally from the start time.

- v) The direction and speed of the mean echo motion were determined from the echo track length and track time. The track length and track direction are the horizontal distance and direction between the initial and

final locations, respectively. The echo track speed is the track length divided by the difference between the initial and final location times.

vi) The two final storm parameters, which represent the echo life cycle data are maximum area and height of the storm echo; the former is the area of the echo at the 2° antenna elevation and the latter is the maximum height of a particular echo observed by an antenna elevation sequence.

These values for the storms on the days analyzed are tabulated later in Table 3.1.

2.2.3B Mean Statistics

For the 159 storms for which values of life time, growth time, decay time, maximum area, and maximum height are available, averages of storm data were computed. These averages are given in the following table.

Mean Storm Characteristics

Life time	141 min.
Growth time	69 min.
Decay time	72 min.
Direction (deg.)	98°
Speed (m/s)	8.6
Maximum area	695 sq. km
Maximum height	10.4 km

A significant correlation was found between the maximum area and the life time of a storm. On the average, large storms last longer. The above authors also showed that there is little correlation between echo height and either lifetime or area for this class of storm system (Areas > 100 km²).

Because the general storm motion was from east to west, the line precipitation index is considered to be a better estimate, on the average, of the study area rainfall than the area precipitation index.

2.2.4 Categorization of Convection

The VIMHEX II data period was categorized in terms of the intensity of the Convection. The daily rainfall index determined from the gauges was used to objectively categorize each day of the experiment as a "dry" or a "wet" day (Table 2.1).

The categories of rainfall were chosen so as to give four roughly equal groups of days. There were more soundings on disturbed days since the study of them had the highest priority.

Table 2.1 Convective Regimes and Rainfall

Convective Regime	Rainfall Index Range (mm)	Number of Days	Number of Soundings
I Dry	< 0.1	23	44
II Diurnal Convection	0.1 - 1.0	27	67
III Enhanced Convection	1.0 - 5.0	28	103
IV Disturbed	> 5.0	21	91

Betts (1974) in his study of "Thermodynamic Classification of Tropical Convective Soundings", by using the same above data, has shown the following features; resulting from averages of the four regimes:

i) From dry to disturbed days, there is a uniform trend towards a cooler, moister atmosphere (see his Figs. 1 and 2).

ii) Apart from the lowest 100 mb, the resulting θ_e of the atmosphere has an increasing trend with increasing precipitation.

iii) The difference in temperature, mixing ratio and θ_e between disturbed and dry averages (see his Fig. 3) shows that the average temperature difference at 500 mb is still only about -1°C ($\theta_{es} = -2.7^\circ\text{K}$).

As the author has pointed out, these are average results, and the scatter in individual soundings is large. Thus, it is still often not possible to use the above mentioned stratification shown by a single sounding as a predictive or diagnostic tool in the tropics. This may be possible on a daily basis given many soundings, but for predictive purposes, there is the additional problem that strong disturbances are often preceded by a strong subsidence zone (see, for example, Chapter 4, for the September 1-2 case).

2.3 The Queen Air Aircraft and Instrumentation

The Queen Air Aircraft, from the National Center for Atmospheric Research (NCAR) with a flight and scientific crew, participated in the Venezuelan International Meteorological and Hydrological Experiment (VIMHEX II) in 1972. This study made extensive use of the data collected by this group. Specifically, the temperature, dew point, wind speed and direction were used.

The Queen Air specifications and performance can be found in Table 2.2a and the sensors routinely carried on this aircraft, together with details such as manufacturer and model number, range, accuracy and response can be found in Table 2.2b.

The data recording system used on the aircraft during 1972 was the ARIS I System (Aircraft Research Instrumentation System). It monitored 64 channels, eight times a second, and recorded them on magnetic tape. Twenty-two parameters were reported by ARIS. NCAR processed the data after the experiment and made it available for this research in the form of one-minute averages on magnetic tape and microfilm. The data acquired by the aircraft proved to be a very useful set of observations. Some limitations on this study were imposed by the use of one minute average data. Some of the peculiarities of each sensor are discussed below.

The temperature sensors were a reverse flow and a Rosemount type with a time constant of six to ten seconds in the former and one second in the latter. The difficulty associated with temperature measurements in clear air from aircraft, as well as the main problem with all aircraft measurements, is simply due to the aircraft motion. If a sensor (resistance wire, thermocouple, etc.) is placed in a high-speed air stream, it will come to equilibrium at a temperature somewhere between

Table 2.2A

QUEEN AIR SPECIFICATIONS

Engine Power:	380 bhp (2,834 kW)
Wingspan:	50 feet (15 m)
Length:	35 feet 6 inches (10.8 m)
Cabin Floor Area:	65.7 feet ² (6.13 m ²)
Empty Weight:	6,100 lb (2,770 kg)
Maximum Gross Weight:	8,500 lb (3,850 kg)
Maximum Payload Weight Limit:	2,400 lb (1,090 kg)
Maximum Landing Weight:	8,500 lb (3,850 kg)
Electrical Power:	
Primary:	28 V dc 90 A 2,520 W
Secondary:	1 ϕ 60 Hz 115 V ac 1,000 VA
	1 ϕ 400 Hz 115 V ac 750 VA
	3 ϕ 400 HZ 115 V ac 750 VA
Fuel Capacity:	1,564 lb (710 kg)

PERFORMANCE

Maximum Cruising Range:	1,000 n mi (1,800 km)
Service Ceiling:	30,000 feet (9,100 m)
Slow-Flight Speed:	IAS 110 kt (204 km/hr)
Maximum Endurance:	6.5 hr

Table 2.2B Basic Meteorological Instrumentation Aboard the Queen Air

BASIC METEOROLOGICAL INSTRUMENTATION ABOARD THE QUEEN AIRS					
PARAMETER	INSTRUMENT TYPE	MANUFACTURER AND MODEL NO.	RANGE	ACCURACY	RESPONSE*
Stagnation Air Temperature	Platinum Resistance Total Temperature Probe	Rosemount Model 102E2AL	-70 to +30°C	±0.2°C	1 sec
	Platinum Resistance Reverse-Flow Total Temperature Probe	NCAR	-60 to +40°C	±0.5°C	8 to 10 sec
Moisture Content	Thermoelectric Dew-Point Hygrometer	EG&G 137-C3-S3	-50 to +50°C	±0.5°C above 0°C† ±1.0°C below 0°C	3°C/sec‡
Pressure Altitude	Variable Capacitance Pressure Transducer	Rosemount Model 1301-A	300 to 1,035 mb	±1 mb†	0.025 sec†
Airspeed	Variable Capacitance Pressure Transducer	Rosemount Model 1301-B	0 to 140 m/sec	±0.14 m/sect	0.025 sect
Magnetic Heading	Flux-Gate Gyro Compass	Sperry Model N-1 (N304D)	0 to 360°	±1.0°	Undetermined
		Bendix C-11 (N306D)		±0.5°	Undetermined
Drift Angle and Ground Speed	Doppler Navigator	Singer-GPL Model APN-153V	0 to 500 m/sec -40 to +40°	Undetermined	Undetermined
Cloud Liquid Water	Hot-Wire Flowmeter	Johnson-Williams Model LWH	0 to 6 g/m³	Undetermined	1.5 sec
Hydrometeor Liquid Water Content	Optical Flowmeter	NCAR	0.2 to 4.5 g/m³	±10%	0.02 sec
Precipitation Particle Sampler	Lead Foil Impactor	NCAR	150 μm to 1 mm		
Radiometric Surface Temperature	Bolometric Radiometer (8- to 14-μm band)	Barnes Model PRT-5	-50 to +50°C	±0.5°C†	0.5 sect
Visible Radiation	Spectral Pyranometer (280- to 2,800-μm band)	Eppley Model 2	0 to 2.5 ly/min	Unavailable	1 sect
Thermal Mapping (N304D)	Infrared Line Scanner‡	Texas Instruments Model RS-310	See article, "Airborne Infrared Imaging System"		
Weather Radar	X-Band Search Radar	RCA Model AVQ-55	0 to 45 n mi		
Photography	16-mm Time-Lapse Camera and Intervalometer	Giannini Model III-B	0 to 16 frames/sec		

* A standard 63.2% time constant is implied unless otherwise specified.

† Manufacturer's specifications. These values may vary considerably depending on aircraft installation configuration and flight envelope.

‡ This instrument is available to qualified users upon request through the National Hail Research Experiment (NHRE) at NCAR.

the ambient, T_{amb} , or static temperature, T_s , and the so called total temperature, T_t , (the total temperature is the temperature which would be achieved if the airstream were isentropically decelerated to zero velocity). This equilibrium temperature is known as the recovery temperature, T_{rec} . The ratio of the difference between the recovery and ambient temperature to the difference between the total and ambient temperature is the recovery factor, rf. The total temperature is a function of both the ambient temperature and the true air speed, TAS. Thus, the determination of ambient temperature from the probe sensor temperature requires the true air speed (which in turn depends upon the air temperature) and the probe recovery factor (which must be empirically determined).

Mathematically, we may derive an expression for T_{amb} such as described above as follows.

Static or ambient temperature (T_{amb}) is computed by use of the relation

$$T_{amb} = T_t \left(\underbrace{\frac{P}{P + \Delta P}}_{<1} \right)^{R/Cp} \quad 2.1$$

where P = static pressure

ΔP = Dynamic - minus - static pressure.

The above two parameters are obtained from a pitot on the aircraft nose or wing. From 2.1, $T_t > T_{amb}$, thus $T_{amb} < T_{rec} < T_t$

The recovery factor is defined by:

$$rf = \frac{T_{rec} - T_{amb}}{T_t - T_{amb}} \quad 2.2$$

The TAS is related with the T_t by the following formula:

$$TAS = \left\{ 2 C_p T_t \left[1 - \left(\frac{P}{P + \Delta P} \right)^{R/Cp} \right] \right\}^{1/2} \quad 2.3$$

Eqs. 2.1 and 2.3 are derivable from the assumptions of conservation of energy and entropy.

From 2.3,

$$T_t = \frac{TAS^2}{2 C_p \left[1 - \left(\frac{P}{P + \Delta P} \right)^{R/C_p} \right]} \quad 2.4$$

Substitution of 2.4 into 2.2 yields

$$rf = \frac{T_{rec} - T_{amb}}{\left\{ \frac{TAS^2}{2 C_p \left[1 - \left(\frac{P}{P + \Delta P} \right)^{R/C_p} \right]} \right\} - T_{amb}} \quad 2.5$$

Equation 2.5 after rearrangements yields to the final expression of:

$$T_{amb} = \frac{2 C_p T_{rec} \left[1 - \left(\frac{P}{P + \Delta P} \right)^{R/C_p} \right] - rf TAS^2}{2 C_p (1 - rf) \left[1 - \left(\frac{P}{P + \Delta P} \right)^{R/C_p} \right]} \quad 2.6$$

Two types of temperature probes are found on the Queen Air: the Rosemount total temperature and the reverse flow temperature.

The principle behind the total temperature probe is to eliminate recovery factor uncertainty by isentropically decelerating the flow before passing it over the transducer (a platinum resistance wire). This is accomplished by means of a design in which the aerodynamic boundary layer which builds up on the probe housing surface, is continually removed. It is this boundary layer which is the source of non-isentropic effects. Due to its presence on all research aircraft as well as its inherent accuracy, the total temperature probe should be considered the primary instrument for measuring ambient temperature.

The reverse flow temperature probe is different. Here the intention was not so much to strive for high accuracy in clear air but to design an instrument which was capable of making reliable temperature measurements in clouds and rain. The technique used is to turn the air through 180° before passing it over the sensor. It is hoped that droplet inertia will serve to separate the liquid water from the air stream and thus eliminate "wet bulb" effects.

The primary limitation on the accuracy of the reverse flow probe in clear air is the uncertainty in the value of the recovery factor, which may vary with the angle of attack of the probe as well as with air speed.

This difference between the Rosemount temperature and reverse flow temperature is discussed in detail in section 2.4.

The amount of moisture in the air was measured by two sensors, a frost point hygrometer and a wet bulb. Because the wet bulb sensor has a large time constant, the frost point hygrometer observations were used. Results of spectral analysis of the derived dew point data have suggested a response time greater than two seconds but less than ten (Seguin, 1972).

The static pressure measurements, which indicated the flight altitude, were made with a pitot-static probe mounted on a nose boom of the aircraft aligned with the fuselage center line. The principle problem in static pressure measurement is that the aircraft modifies the pressure field not only near the wing and fuselage surfaces but also for a considerable distance ahead of the aircraft. Thus, no matter where static pressure is measured, this modification effect (known as the static pressure defect) must be determined, for example, by means of tower fly-bys. Since VIMHEX II, NCAR has parameterized this error which amounts to 1 to 2 m s^{-1} at Queen Air speed, which agrees with the error found in this study in the true air speed after using graphical and analytical methods such as explained in section 2.4.

The response times and accuracy of the Doppler Navigation System and the derived wind speeds were unknown as is indicated in Table 2b. Because wind speed was determined from the true air speed and ground velocity, special attention was directed to this problem which is discussed in section 2.4. The 16 mm time lapse movies taken by the aircraft were used on a number of flights to indicate the general conditions through which the aircraft was flying.

2.4 Aircraft Data Reduction and Corrections

2.4.1 On the Difference Between the Rosemount Temperature and Reverse Flow Temperature

To obtain a temperature analysis into which both the radiosonde and aircraft values could be integrated, the aircraft temperatures (Rosemount and reverse flow temperatures) were used to compute values of potential and equivalent potential temperature. Therefore, two values of each parameter could be calculated.

It was mentioned earlier that the aircraft temperatures, reverse and Rosemount give a better measurement depending on the weather conditions found during the flight. The former is thought to give a better measurement through clouds and rainy areas while the latter is better in clear areas. In order to investigate the above difference, a procedure explained below was used.

i) Two continuous legs, in the northeast-southwest and southwest-northeast directions with Carrizal rawinsonding site located within them, were chosen. These two legs were flown from 15.11 to 15.30 LST and from 15.31 to 15.49 LST, covering a horizontal extension on the ground of about 90 km and 85.5 km, respectively. They correspond to the flight mission 17 carried out on August 21.

ii) During the flight along the above legs, values of the reverse flow potential temperature (θ_{Rf}) were subtracted from values of the Rosemount potential temperature (θ_R). These calculations were made each minute and after that a mean difference of 1.7°K was found. The constancy of this value showed clearly that no differences between the two temperatures could be established when the aircraft was flying either in a cloud-rainy area or in a clear area. (See Fig. 2.8A), at least using one minute averages.

Figure 2.8a Comparison between reverse flow potential temperature (θ_{RF}) and the Rosemount potential temperature (θ_R).

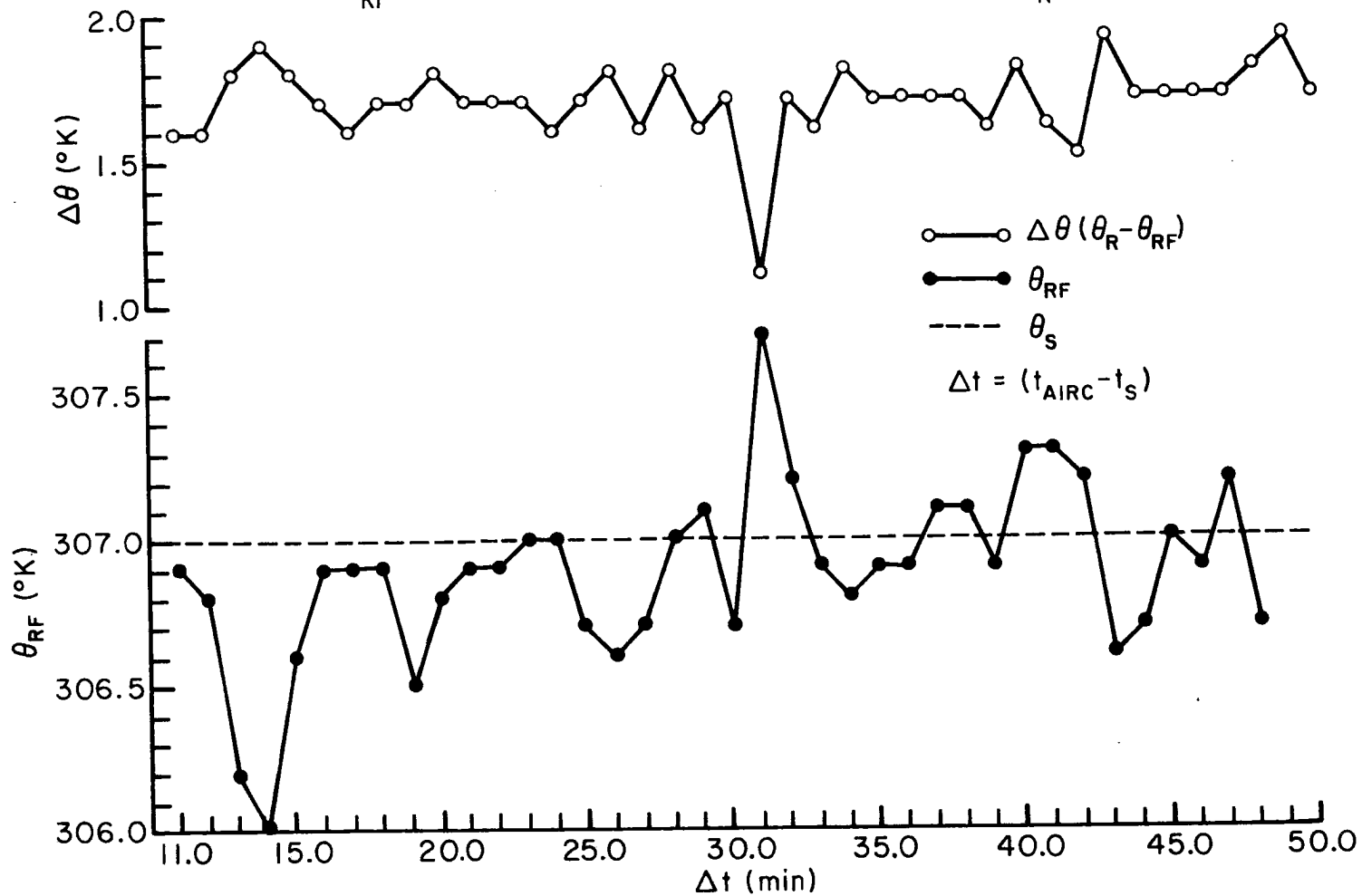


Figure 2.8b Comparison between reverse flow potential temperature (θ_{RF}) and the potential temperature (θ_S) of the sounding.

Next, another point, related to what aircraft temperature to use in this study was considered. Measurements of θ_{Rf} were compared with θ given by the sounding launched at Carrizal at the aircraft level (850 mb) when the flight path was located close to Carrizal.

By using the same procedure described in i, measurements of θ_R and θ_{Rf} were subtracted from the value of θ given by the Carrizal sounding launched at 15.00 LST, as well as the difference in time between measurements taken. After that, it was found that the difference between θ_R and θ of the sounding may be accounted by a systematic factor of $-1.6^\circ\text{K} \pm 0.3$ while the difference between θ_{Rf} and θ of the sounding were within $\pm 0.3^\circ\text{K}$ (see Fig. 2.8b).

This kind of comparison was extended to all of the flight missions used in this study. After that, it was found that the reverse flow temperature was most of the time closer to the radiosonde measurement than the Rosemount temperature, thus, the former was used in this study. $\theta_R - \theta_{Rf}$ was systematically $+ 1.7^\circ\text{K}$.

2.4.2 Corrections of Specific Humidity, Equivalent Potential Temperature and Potential Temperature to 850 mb Level.

In order to obtain a source of comparison with the radiosonde data at one unique level and to eliminate variations in aircraft altitude (flight level pressures varied from 825 to 875 mb), derived aircraft measurements of equivalent potential temperature, potential temperature and specific humidity were corrected to 850 mb. The correction was carried out by using high resolution radiosonde data at each 10 mb in the low levels. Values of the above parameters were taken from 900 to 810 mb on twenty

soundings launched from 1437 LST to 1600 LST, with cloud base between 790-830 mb.

The differences from the mean value at 850 mb of each parameter, were then plotted against pressure. Figure 2.9 shows these curves which were used to correct the aircraft data to 850 mb. It is seen that the corrections are small for flight level pressures between 825 and 875 mb.

2.4.3 Horizontal Wind Measurements

The actual determination of the horizontal wind vector requires measurement of the following quantities:

- i) True air speed. This quantity depends upon pressure (both static and dynamic) and total temperature.
- ii) Angle of side slip and, to a lesser extent, angle of attack.
- iii) Ground speed.
- iv) Drift angle.
- v) True heading.

The accuracy to which the horizontal wind vector can be determined is a function of the accuracy of the five quantities listed above. Uncertainty in the true airspeed measurement and drift angle are usually the limiting factor on the accuracy of the horizontal wind. These were estimated by using graphical and analytical methods which are explained next.

2.4.4 True Airspeed and Drift Angle Correction

A change in aircraft heading produces an apparent change in the wind vector. This inconsistency is the result of systematic errors in true air speed and drift angle from which the wind is computed.

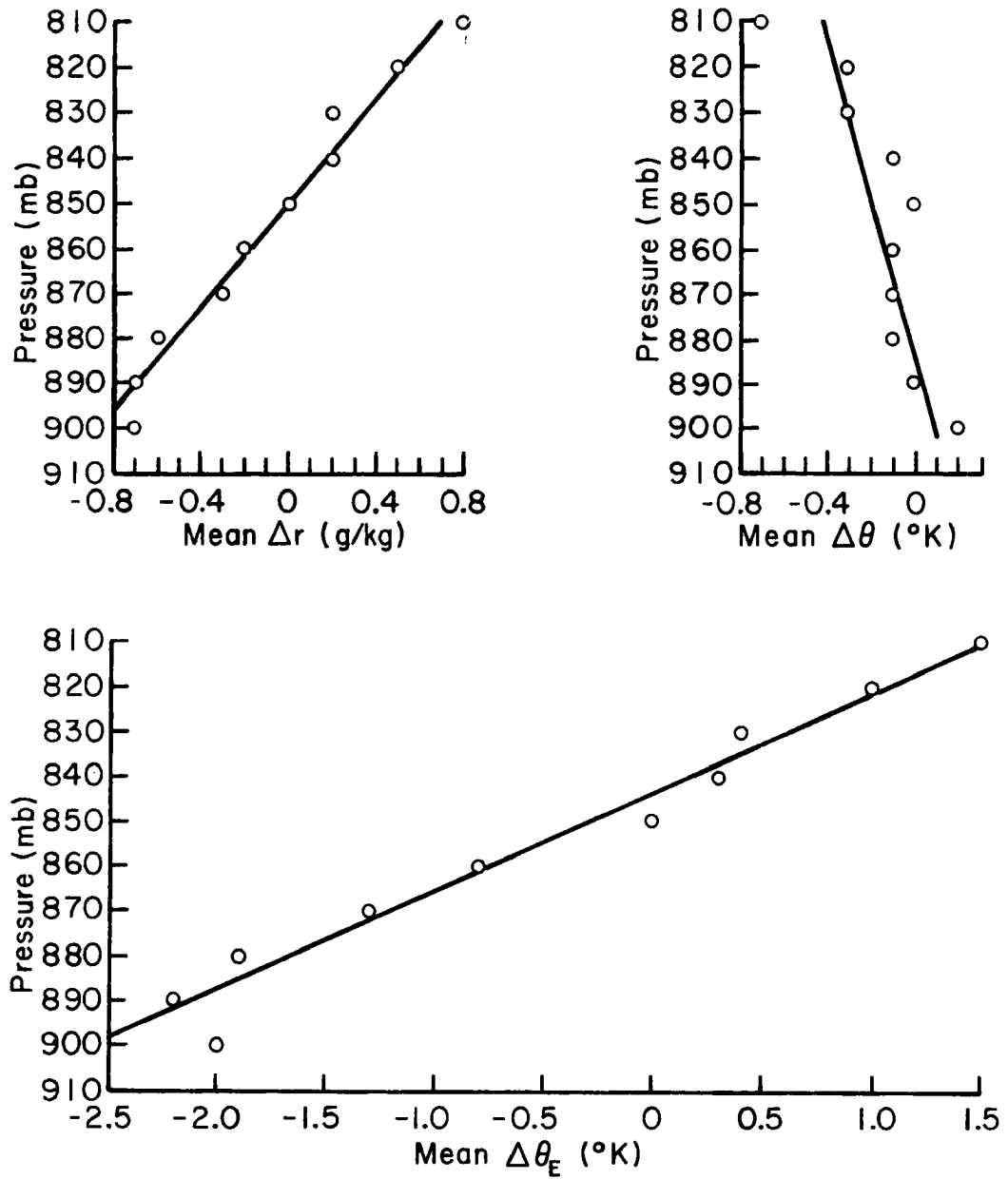


Figure 2.9 Correction curves used to correct the aircraft data to 850 mb.

Consider the following figure:

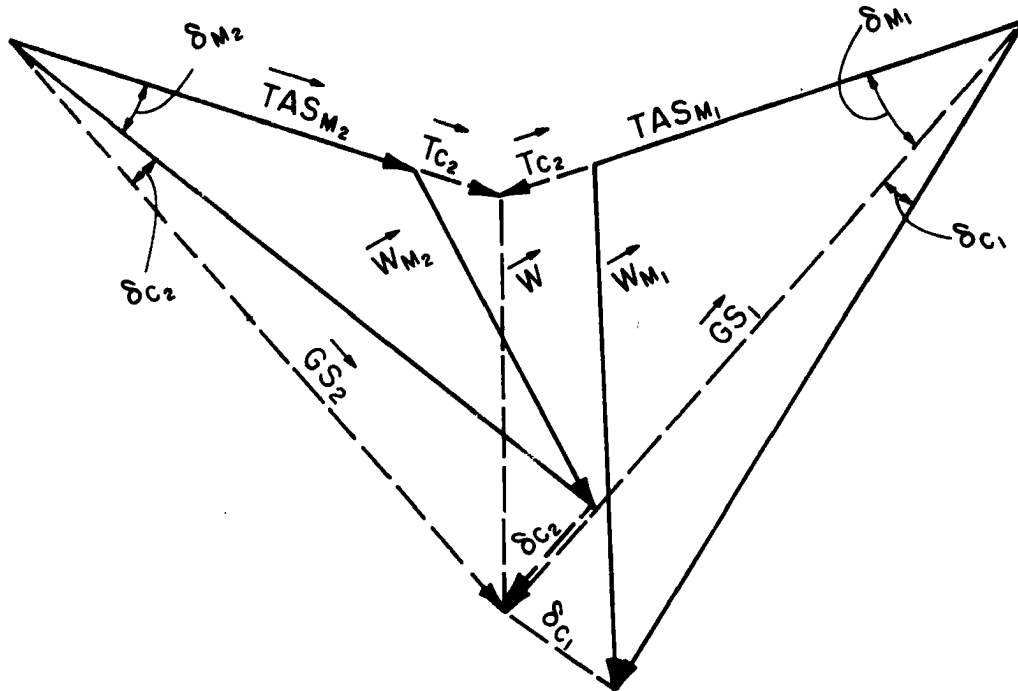


Figure 2.10 Wind velocity triangles for before and after a sharp change in aircraft heading, showing how instrumentation errors affect their geometry. The measured wind velocities, W_{m1} and W_{m2} , are found to differ following a sharp turn, but the actual wind, W , remains the same (for legend of symbols, see List of Symbols).

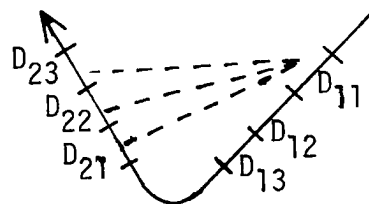
Here the vectors TAS_m represent the aircraft's measured movement with respect to the air, the vectors GS_m represent the measured movement with respect to the ground, and δ_m the measured drift angles. Thus, the vector W_m is a measured wind vector obtained by vector subtraction of TAS_m from GS_m .

$$\vec{W} = \vec{GS} - \vec{TAS} \quad 2.7$$

Figure 2.10 illustrates how an error in either drift angle or true air speed produces a spurious change in the measured wind when the plane changes its heading. The effect is more noticeable when the winds are light and tend to concentrate a fictitious amount of divergence and vorticity near the turns.

The usual procedure to refine the wind measurement is to assume errors in both the measured drift angle and the measured true air speed, indicated in the above figure by T_c and δc . As used here, T_c and δc are corrections applied to the measured quantities to compute the wind, W . This method is used by NCAR, RFF (Research Flight Facility) and the National Hurricane Research Laboratory (see Friedman, et al, 1969). These corrections are then derived from the apparent wind change when the aircraft reverses heading or makes a turn, assuming that the true wind is constant in space and time.

During VIMHEX II, the magnitude of the true air speed (T_c) and drift angle (δc) corrections were computed (see Appendix 1) from the pattern corners by assuming the true wind remained constant. Three minutes of data were considered on either side of a corner, and T_c and δc were calculated from the independent pairs of data, one minute before the turn and one after (Fig. 2.10). Denoting the data for a minute D_{ij} , corrections could be found by comparing D_{11} with D_{21} , D_{22} , D_{23} , etc. The only assumption is that the true wind is the same for all D_{ij} .



The average corrections were:

	<u>Mean</u>	<u>Standard Deviation</u>
T_c	$= 1.3 \text{ m s}^{-1}$	0.4
δc	$= - .73 \text{ degrees}$	0.3

These values correspond to the total average of 29 corners for the above four missions. Combined, the two corrections remove from the measured wind about 2 m/s of error. The calibrated accuracy of the system for measuring winds on the Queen Air aircraft, from NCAR, is considered to be about $\pm 1-2$ m/sec. A residual error of approximately $\pm 1 \text{ m s}^{-1}$ is probably still present after correction.

3. ANALYSIS AND RESULTS OF DATA COLLECTED AT MESOSCALE

3.1 Introduction

Essential to the understanding of how convective systems respond to and conversely, modify their environment, is the adequate description of atmospheric variables at an appropriate scale.

In discussing the value of weather radar in meteorological research, Lidga (1951) recognized a scale too gross to be observed, yet too small to appear even on a sectional synoptic chart. He stated that "phenomena of this size might well be designated as mesometeorological". Regarding the expanded scope of mesometeorological research integrating radar and special network data, Tepper (1959) has emphasized the importance of research dealing in detail with the mesoscale. A surface microstudy of squall line thunderstorm by Williams (1948), a meso-analytical study of the thunderstorm-nose by Fujita (1950), and that of a cold front by Fujita (1951) are investigations of mesometeorological phenomena. All of these early studies as well as incorporation of satellite data for use of study of mesoscale nephsystem, made it evident that actually it is possible to obtain enough data in various forms to undertake a broad research on mesoscale disturbances.

Betts (1974) in his study of the scientific basis and objectives of the U.S. Convection Subprogram for the GATE, has dealt among other topics, with the concept of scale for tropical disturbances. This study has defined four scales: wave scale, cloud cluster scale, mesoscale and cumulus scales for GATE. Their magnitudes have been adopted in this study, mainly the mesoscale (10 to 10^2 km) and the cumulus scale (1 to 10 km).

Although, VIMHEX II did not operate a meso-network of rawinsondes, the use of different sources of data (synoptic, pibal balloon, radar echo, soundings, rainfall and aircraft data) allowed the investigation of mesoscale disturbances present during part of the experimental time period.

It is the purpose of this chapter to study the mesoscale structure of the subcloud layer by using the above combination of data.

Section 3.2 deals with data collected at a single station following the scheme below.

Subsection 3.2.1. Categorization of convection based on daily rainfall index, and the thermodynamic structure of the sub-cloud layer based on soundings launched in the experimental area, for the days chosen.

Subsection 3.2.2. Radar data and precipitation systems occurring for the above period.

Section 3.3 deals with the aircraft data in the following manner:

Subsection 3.3.1. Description of the missions studied.

Subsection 3.3.2. Calculations of divergences and vorticity at the flight level (850 mb).

Subsection 3.3.3. Analysis of the horizontal wind, specific humidity and temperature for the same height and time as above. This subsection will also include a study of the variability of several parameters (wind, temperature and mixing ratio) at the flight level.

Subsection 3.3.4. Comparison of the derived aircraft analysis with the 850 mb chart and pilot balloon analysis.

Subsection 3.3.5. Comments on the dynamic and thermodynamic features at cumulus scale.

3.2 Single Station Analysis for the Days Chosen.

3.2.1 Categorization of Convection and Thermodynamic Structure for the Above Days

Following the criteria already discussed in subsection 2.2.4, the days chosen in this study are classified in the next table.

Convective Regime	Rainfall Index (mm)	Day	Number of Soundings	Recorded Rainfall (mm)
II Diurnal Convection	0.1 - 1.0	Aug. 21	5	1.0
		Aug. 22	4	0.2
		Aug. 30	4	0.7
III Enhanced Convection	1.0 - 5.0	Aug. 29	6	2.0
IV Disturbed	> 5.0	Sept. 1	6	69.6
		Sept. 2	6	19.9

The stratification of the atmosphere from surface to 800 mb, during the above missions was studied by the vertical and the time variation of the potential temperature (θ), equivalent potential temperature (θ_e) and mixing ratio (r) as measured by the radiosondes at Carrizal. Figures 3.1 to 3.3 a&b show these profiles as well as the cloud bases for the different soundings. The height of cloud bases were determined using high resolution radiosonde data. They were estimated from the lifting condensation level (LCL) of air just above the superadiabatic level (Betts, et al, 1974).

Because the days of "diurnal convection" do not show significant differences with respect to the days of "enhanced convection", they were considered as a single group with the following thermodynamic characteristics.

Thermal Structure The atmosphere at 1000 LST is seen to be unstable from surface up to 970 mb. After 1000 LST, the increase in potential temperature increases the instability of the lowest layer, and during the

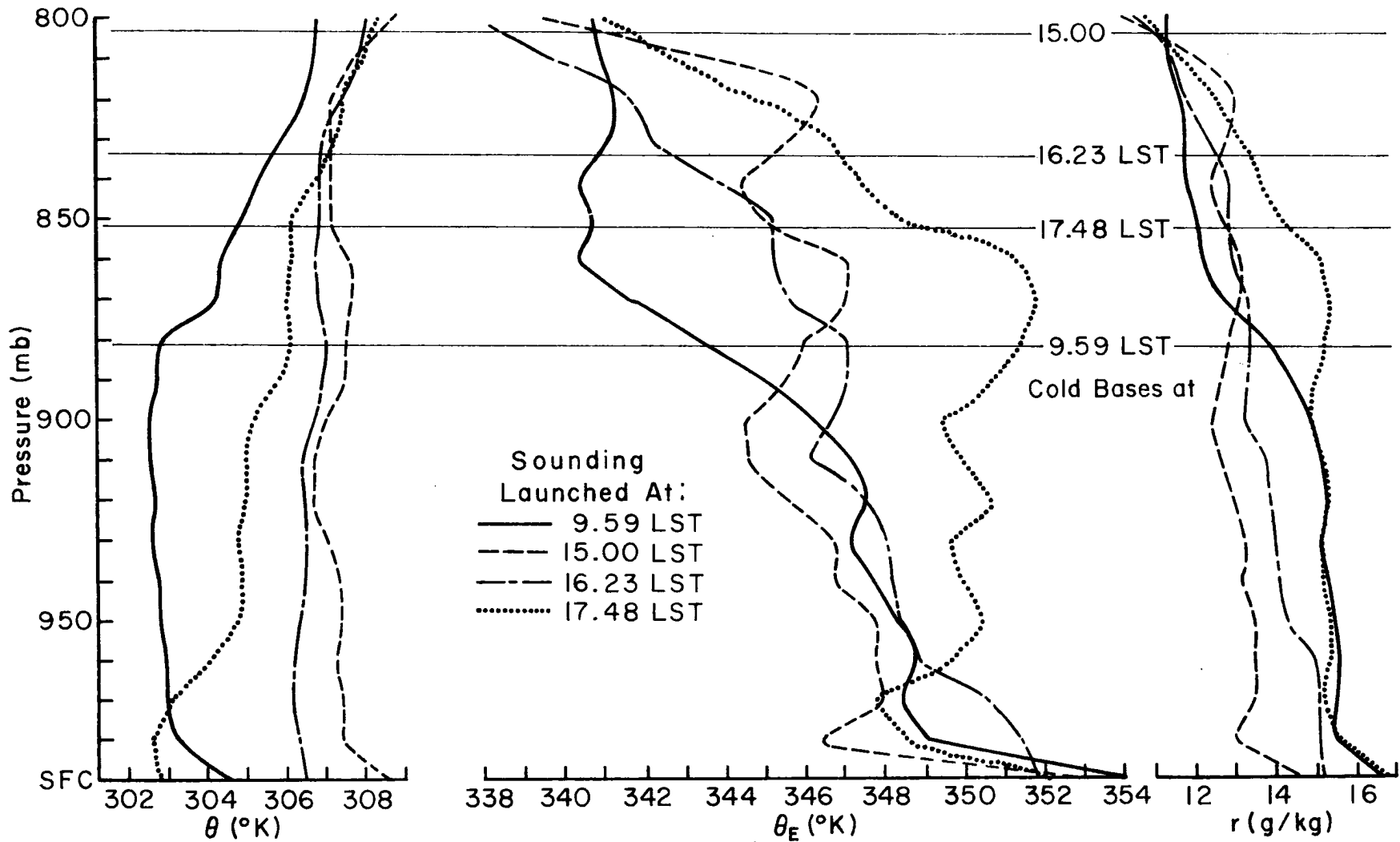


Figure 3.1 Vertical and time variation of the potential temperature (θ), equivalent potential temperature (θ_e), mixing ratio (r), and cloud base for August 21.

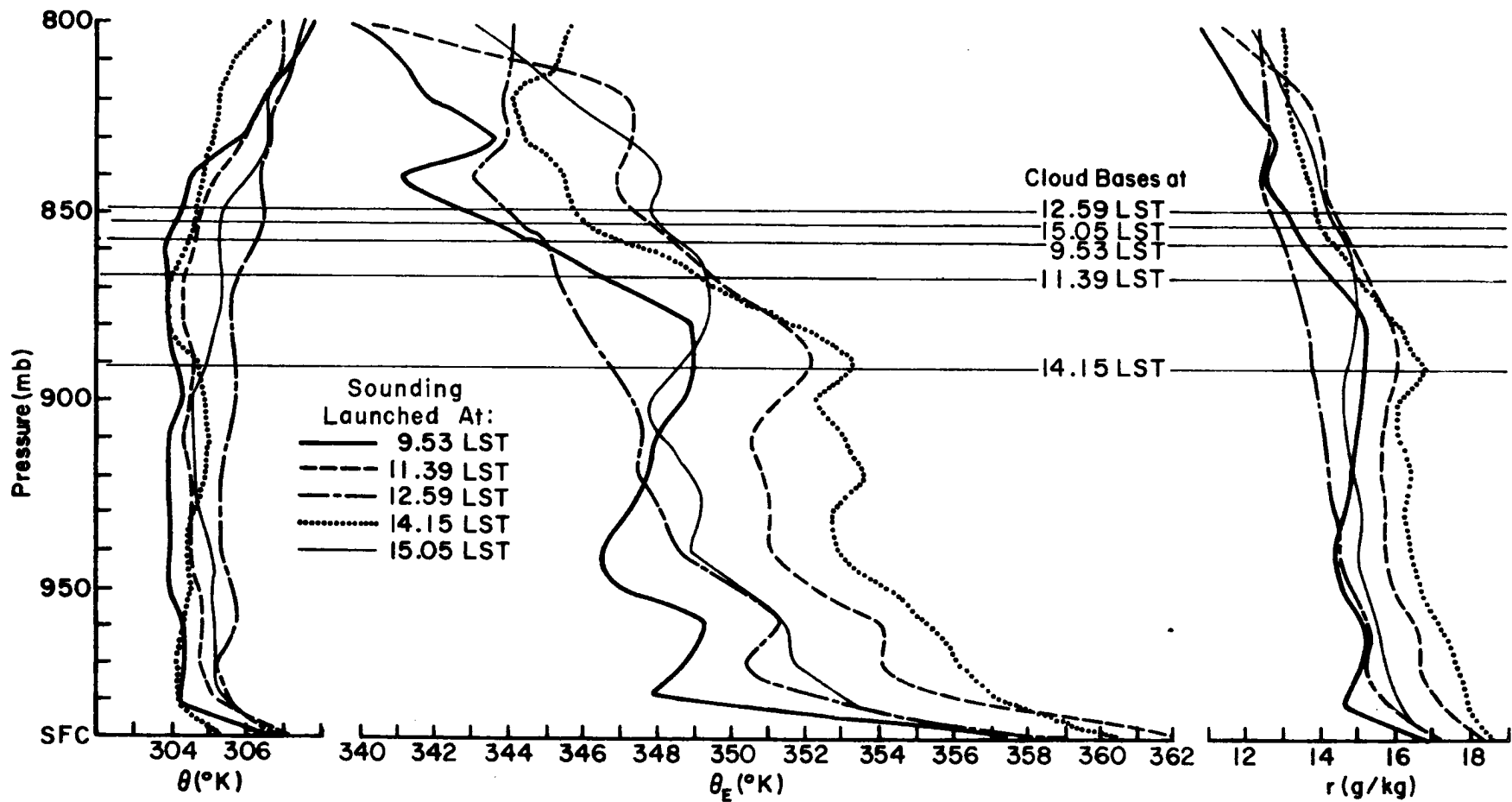


Figure 3.2 Vertical and time variation of the potential temperature (θ), equivalent potential temperature (θ_e), mixing ratio (r), and cloud base for August 29.

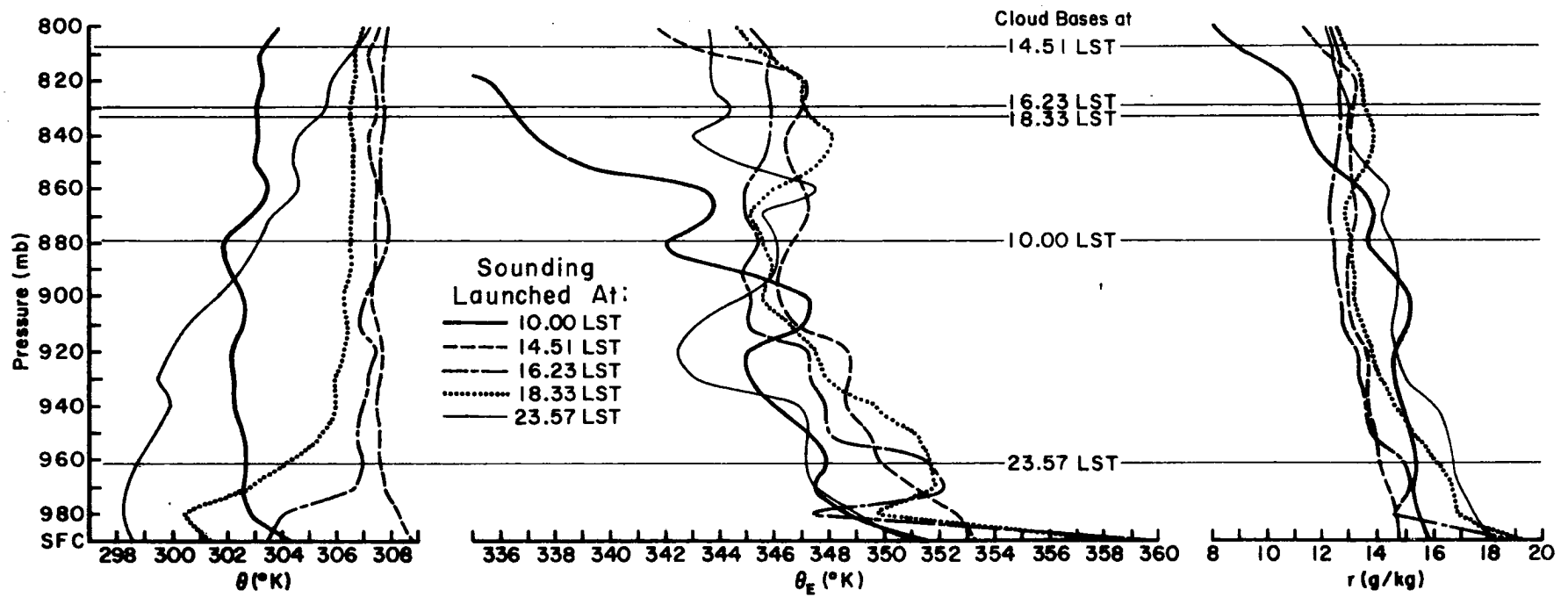


Figure 3.3a Vertical and time variation of the potential temperature (θ), equivalent potential temperature (θ_e), mixing ratio (r), and cloud base for September 1.

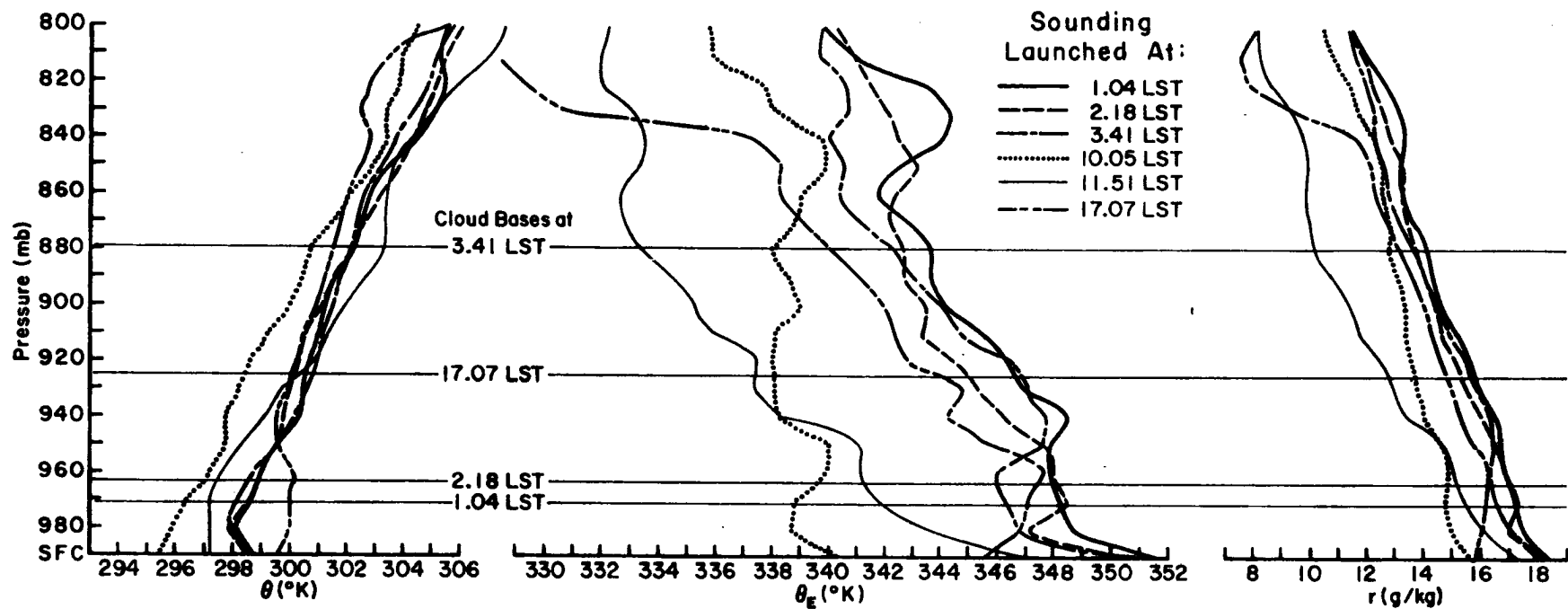


Figure 3.3b Vertical and time variation of the potential temperature (θ), equivalent potential temperature (θ_e), mixing ratio (r), and cloud base for September 2.

late afternoon the decrease in potential temperature near the surface increases the stability of the lowest layers. From 970 mb up to the LCL's of each sounding, a well mixed layer is observed.

Moisture Structure Moisture decreased rather uniformly from 1000 LST to late afternoon between surface and the LCL's for each sounding. Above, an increase in the moisture is observed, especially pronounced on August 21 by 1748 LST.

θ_e Structure A decrease in the equivalent potential temperature is observed between surface and 970 mb from 1000 LST to late afternoon indicating the existence of potential instability. For the same time period and above 970 mb up to 800 mb, the mean θ_e value of the layer increases throughout most of the period during which convection is taking place. This is possibly due to the increasing precipitation observed during these days, and also probably related to the change in instability observed in the potential temperature and moisture.

On disturbed days, the situation was quite different as is explained below.

Thermal Structure From September 1 to September 2 there is a definite cooling below 800 mb. This cooling near the surface reflects the evaporation of precipitation falling through the sub-cloud layer as well as the convectively induced downdrafts of cooler air.

Moisture Structure The layer between the surface and about 960 mb has increased its moisture content. The moisture increase in the layer just above the surface is due, in large part, to the re-evaporation of precipitation from the surface (see the sounding at 1451 LST on September 1 and the sounding at 1151 LST on September 2). From 960 mb to 800 mb there is a significant drying during this period.

θ_e Structure From September 1 to September 2 there is an increasing trend in θ_e with increasing precipitation at high levels, but a marked fall of θ_e at low levels.

These two days are treated in detail separately in Chapter 4 in which a study of the meso-synoptic structure of September 1-2 disturbance is made.

The remark about the conditions already discussed is that the soundings represent conditions essentially at one specific time. However, during the morning and early afternoon, as surface heating increases, the air temperature rises; typically, it is found that at every level up to some maximum the potential temperature itself increases with time but the gradient stays sensibly constant. The level near cloud-base at which there is an abrupt increase in potential temperature gradient rises progressively. Provided that there is adequate moisture in the air and surface heating proceeds long enough, a cloud ultimately forms, and commonly at a level slightly above the abrupt increase in potential temperature gradient. A typical sequence of events is seen in Figs. 3.1 to 3.3 a & b.

3.2.2 Radar and Precipitation Systems

Good radar coverage and a mesoscale raingauge network permitted areal resolution of precipitation systems. This information is used here in order to study several storms present before, during and after aircraft missions.

The PPI data were prepared for analysis by constructing 15-minute and one hour echo charts on transparencies to determine the motion and intensification of echoes.

Composite echo charts were then constructed for each hour, for the days chosen at the aircraft mission periods.

The daily station rainfall for the project raingauges are given by Betts and Stevens (1974). The values given are the daily rainfall, in mm, for the 24-hour period beginning at 0800 hours for the days of August. For September 1, the average is for the period from 0800 September 1 to 1200 September 2. For September 2, the average is for the period from 1200 September 2 to 1200 September 3. In order to estimate the daily rainfall over the study region, two precipitation indices were computed daily from the raingauge data collected each morning (Fig. 2.2). Recording raingauges records were used in this study in order to construct hourly average isohyct charts for the aircraft mission periods while recording and nonrecording raingauges in and adjacent to the study area were used to construct daily average isohyct charts. Also used in combination with the above charts were half hourly average of wind (speed and direction), pressure, relative humidity and temperature at surface for the same time period.

Table 3.1 shows the values of the line and area precipitation indices as well as the echo life cycle data observed during the aircraft mission periods while Figs. 3.4 to 3.7 show hourly averages and daily echo-rainfall composite charts for the above period.

August 22 and 30 are not included because there was no radar coverage during these days (almost dry days). Storms 108 and 109 observed on September 1 and 2 respectively, were the longest observed during the summer. Because of that, they are presented in the daily echo-rainfall composite charts at their peak times. Storm 108 at its peak (2215) had

Table 3.1 Echo and precipitation data during the aircraft mission periods. (Definitions see 2.2.3A)

DATE	LINE PRECIP. INDEX (%)		AREA PRECIP. INDEX (%)		ECHO LIFE CYCLE DATA							
	Average Precip. (mm)	N° Stations With Rain	Average Precip. (mm)	N° Stations With Rain	Storm No.	LOCAL TIME OF ECHO			Max. Area (sq km)	Max. Height (km)	Echo Lifetime (min)	Echo Track Dir.(deg)/Speed(ms ⁻¹)
Aug. 21	1.0	8	1.9	18	86	1550	1745	1930	368	15.5	220	93/12.9
Aug. 22	0.2	2	0.7	8								
Aug. 29	2.0	14	1.8	24	97	1200	1215	1345	161		105	94/11.1
					98	1215	1300	1345	329	14.1	90	83/7.8
					99	1215	1400	1500	271	15.8	165	75/10.5
					100	1230	1345	1415	187	9.9	105	85/11.2
					101	1315	1330	1545	542	12.2	150	50/7.8
					102	1400	1430	1615	394	9.0	135	50/7.8
					103	1515	1600	1645	110	9.9	90	72/10.1
Aug. 30	0.7	8	0.4	8								
Sept. 1	69.6	23	66.5	40	104	1615	1830	2000	503	16.4	225	120/8.6
					104	1615	1830	2000	503	16.4	225	180/11.6
					104	1615	1830	2000	503	16.4	225	94/15.3
					105	1800	1845	2130	258	10.6	210	119/7.0
					105	1800	1845	2130	258	10.6	210	98/10.1
Sept. 2	16.9	23	18.0	40	108	2115	2215	0300	4767	16.2	345	95/5.2
					109	0345	0645	1200	11481	14.1	495	87/3.1
					109	1215	1300	1415	2309	7.0	120	93/3.4

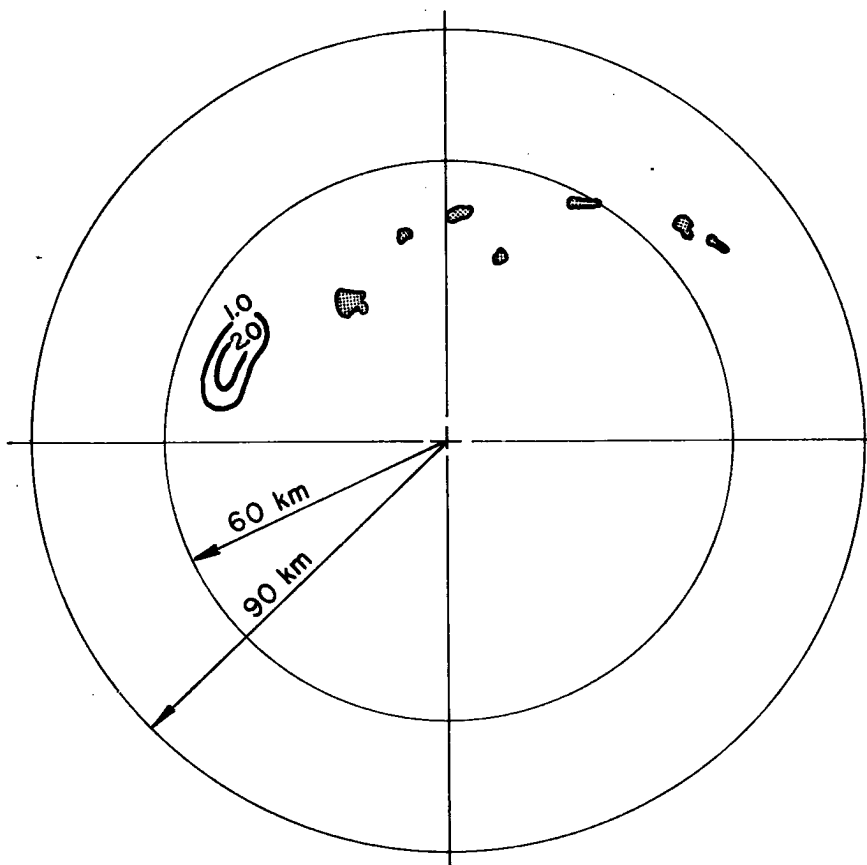


Figure 3.4a 1400-1500 hourly echo and average rainfall composite chart for August 21.

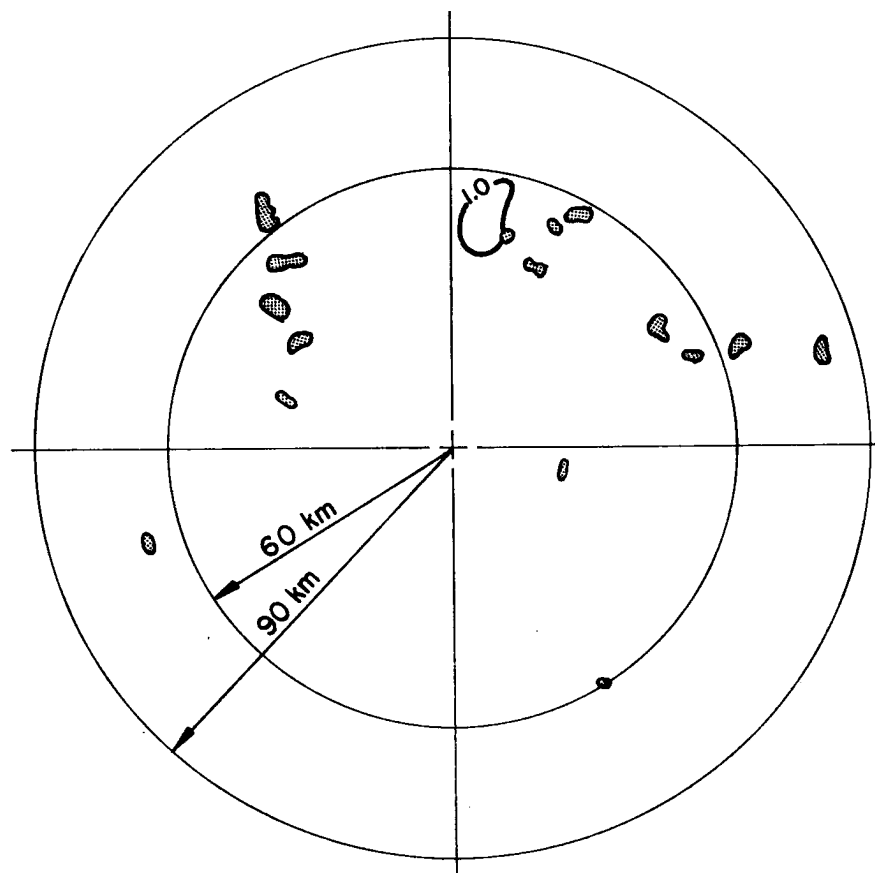


Figure 3.4b 1500-1600 hourly echo and average rainfall composite chart for August 21.

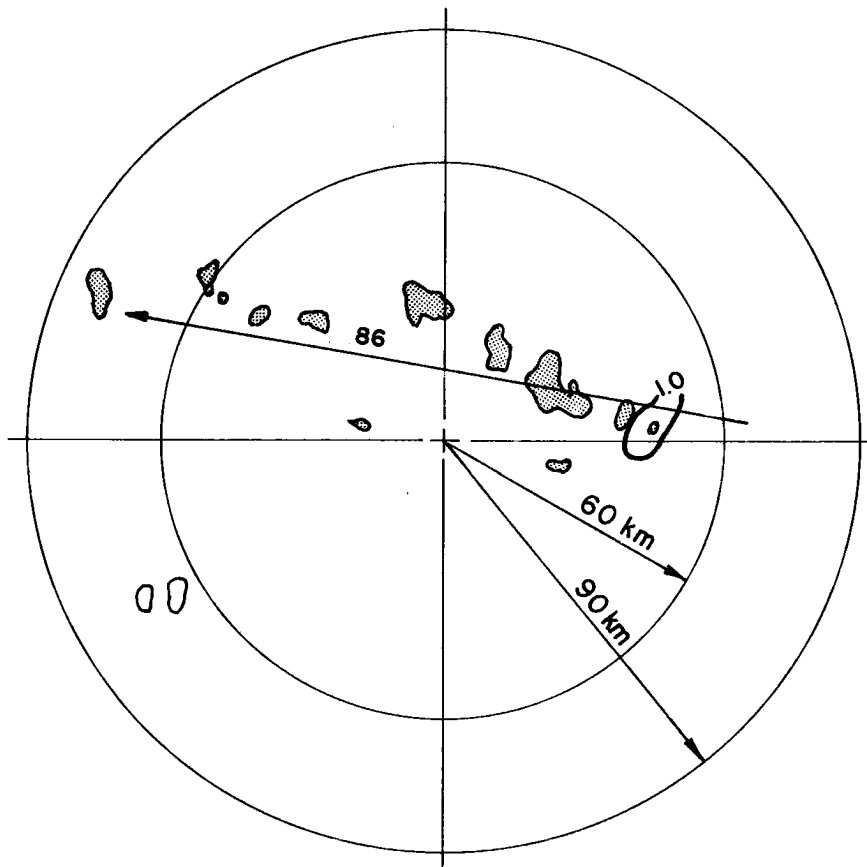


Figure 3.4c 1600-1700 hourly echo and average rainfall composite chart for August 21.

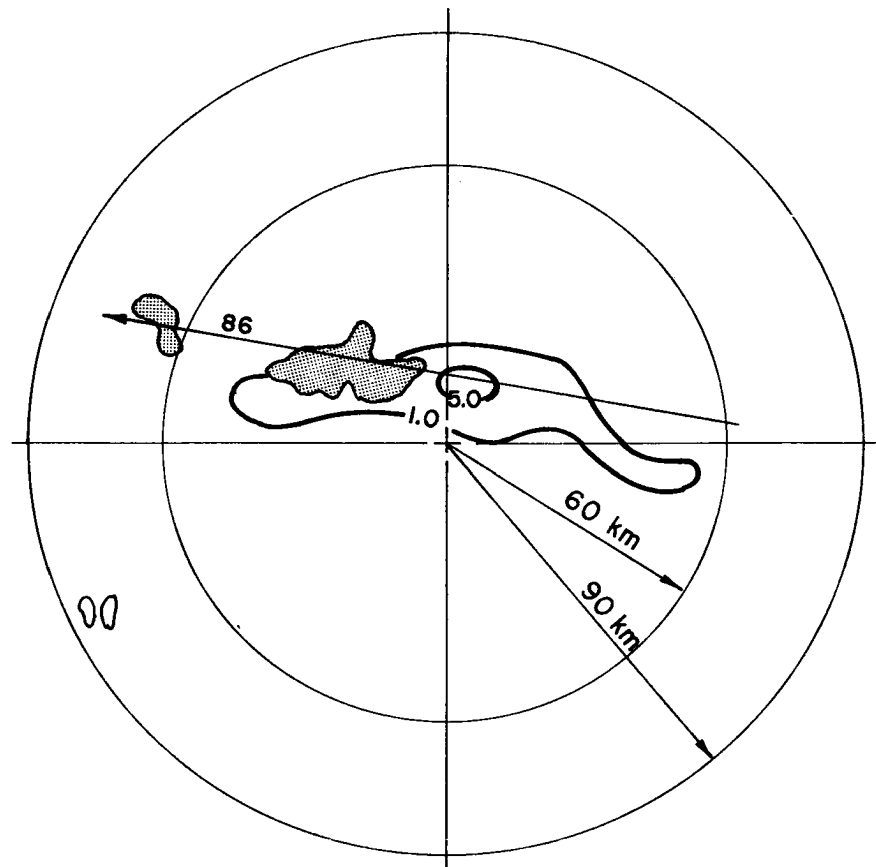


Figure 3.4d 1700-1800 hourly echo and average rainfall composite chart for August 21.

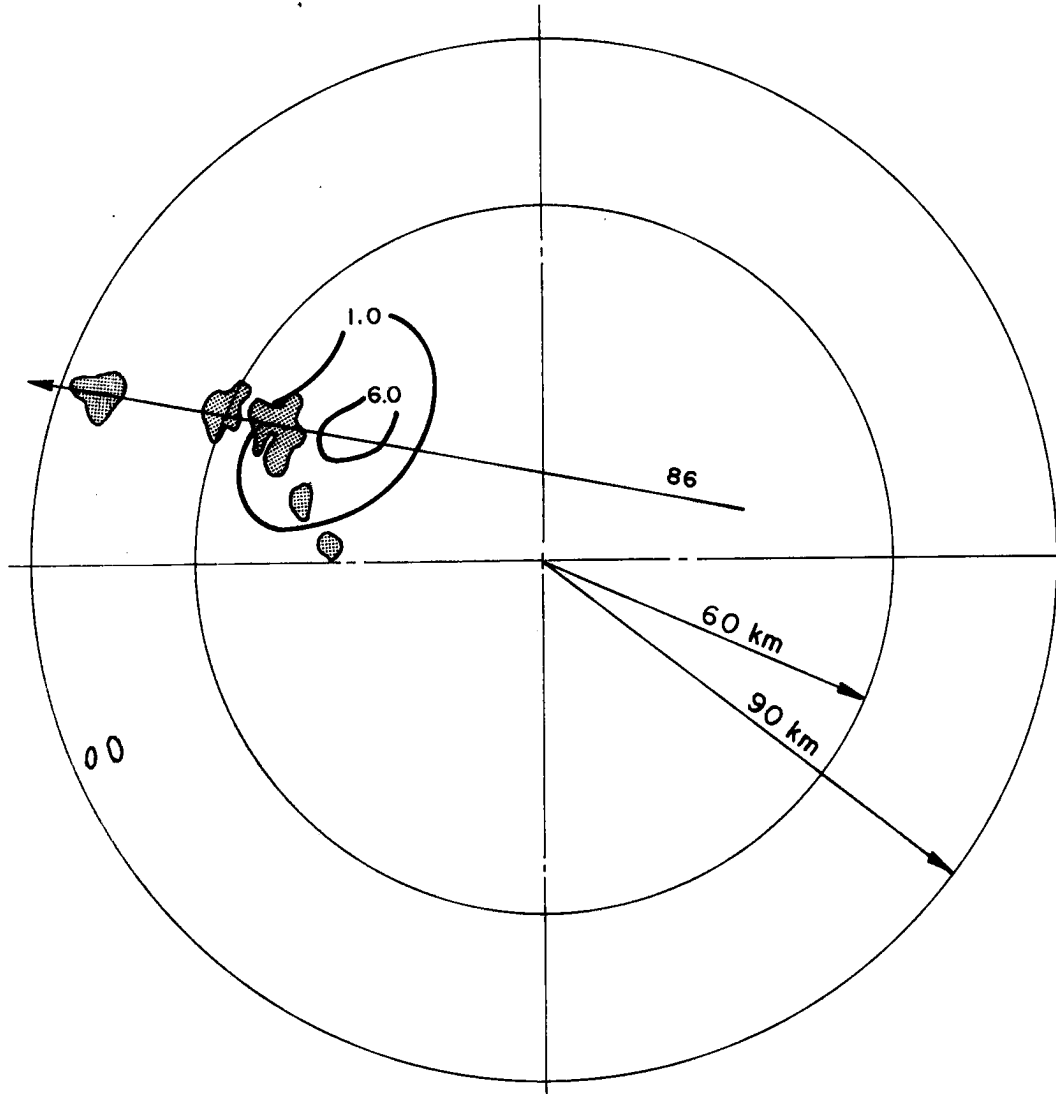


Figure 3.4e 1800-1900 hourly echo and average rainfall composite chart for August 21.

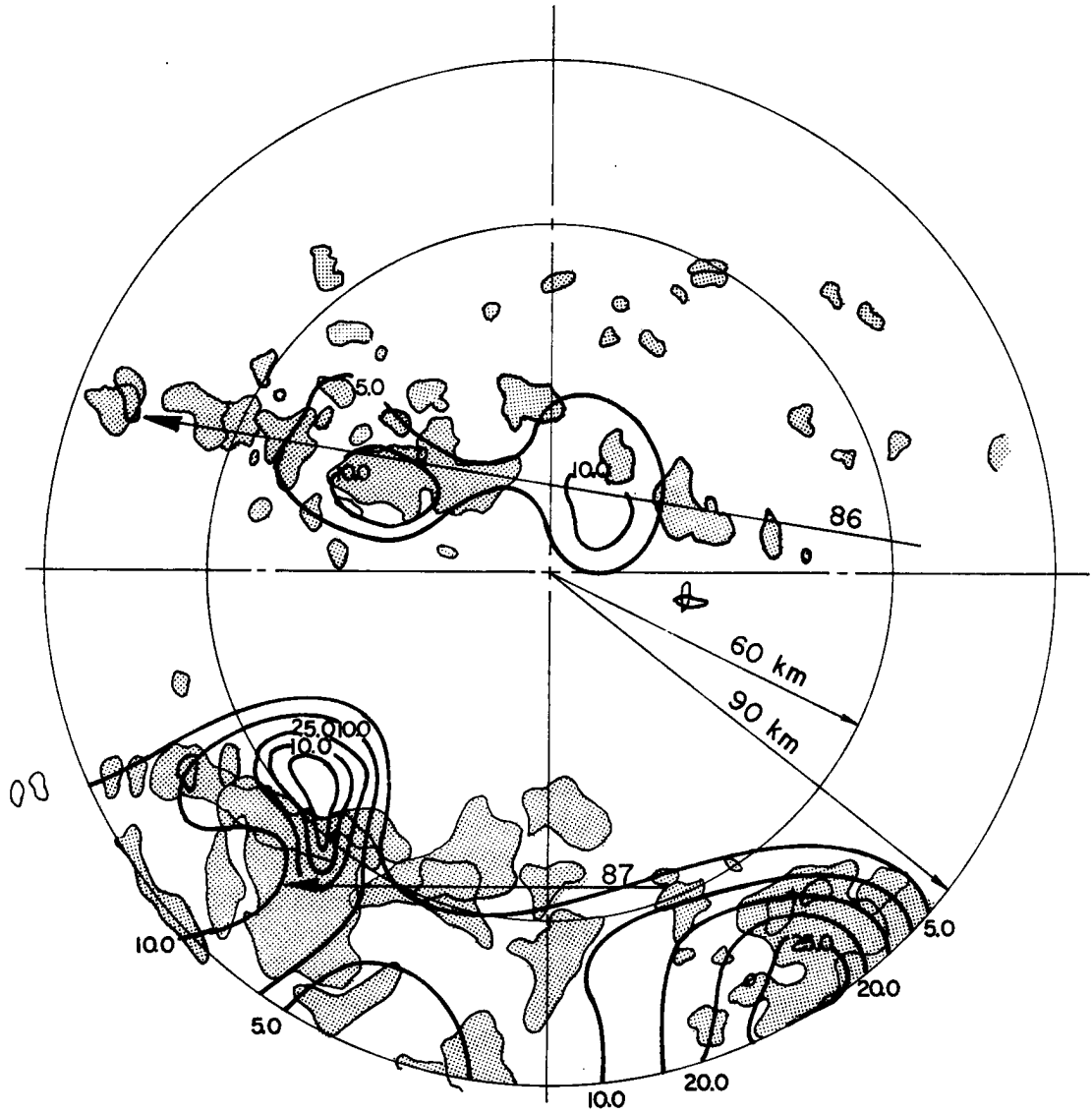


Figure 3.4f Daily echo and average rainfall composite chart for August 21.

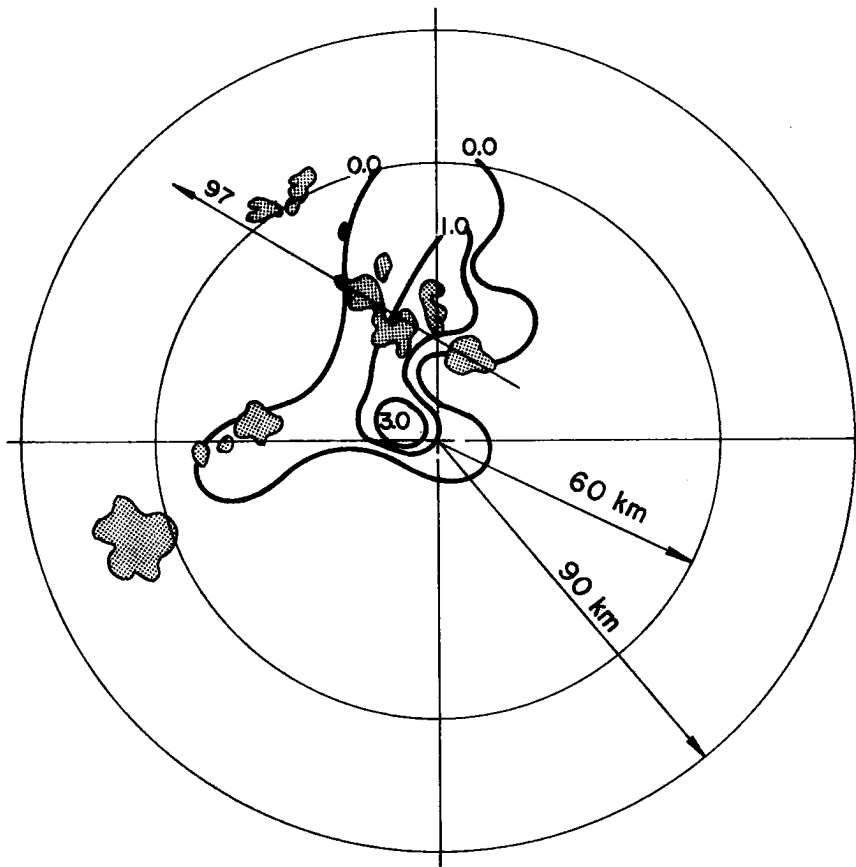


Figure 3.5a 1200-1300 hourly echo and average rainfall composite chart for August 29.

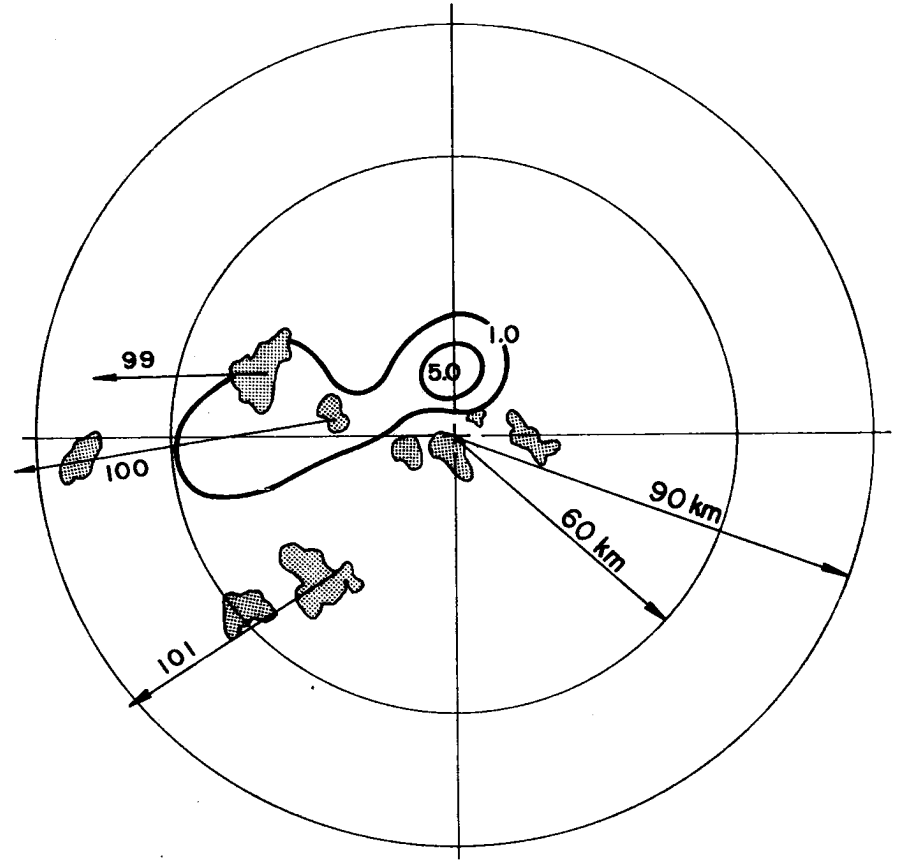


Figure 3.5b 1300-1400 hourly echo and average rainfall composite chart for August 29.

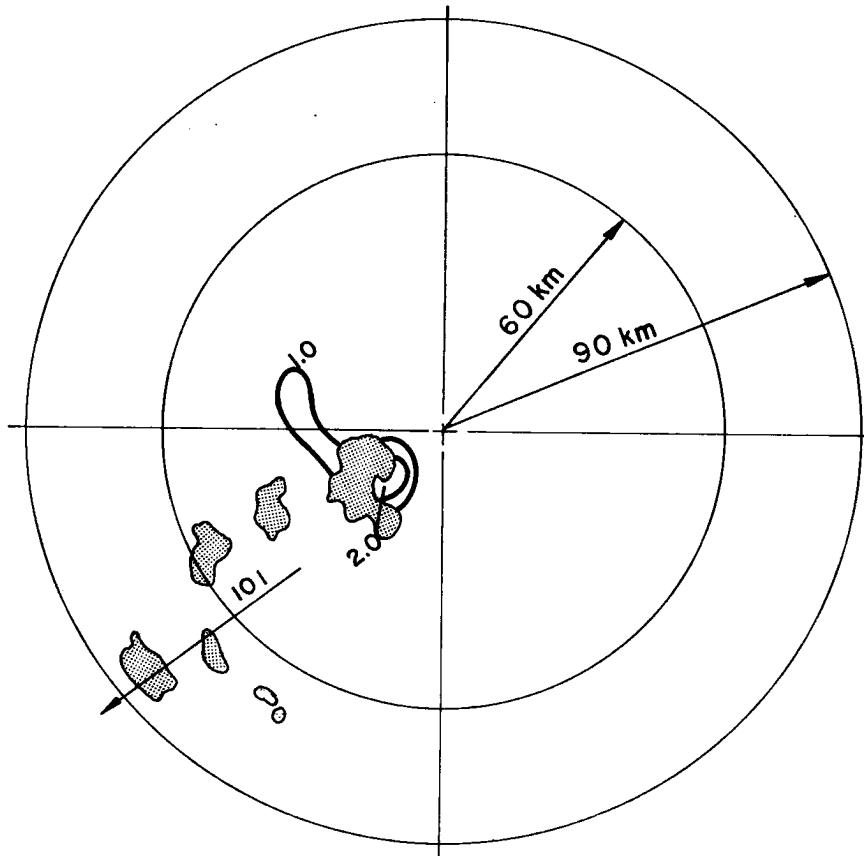


Figure 3.5c 1400-1500 hourly echo and average rainfall composite chart for August 29.

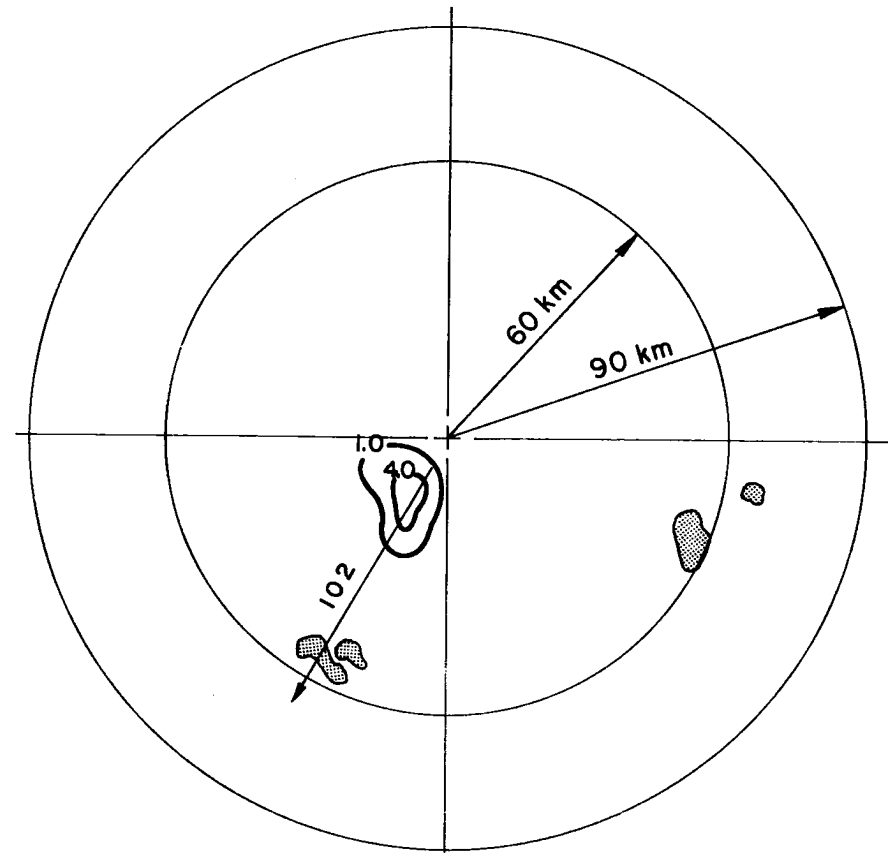


Figure 3.5d 1500-1600 hourly echo and average rainfall composite chart for August 29.

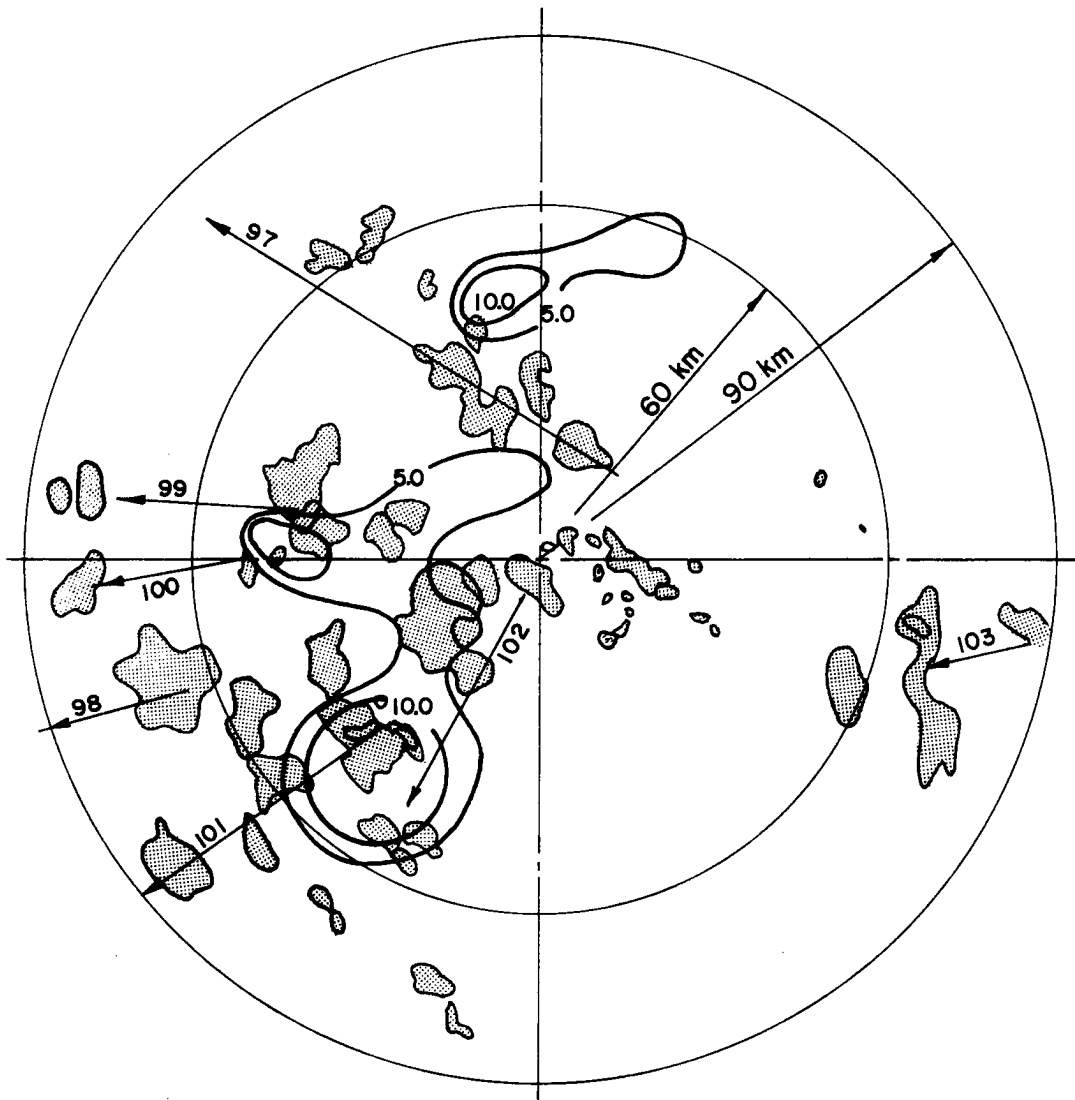


Figure 3.5e Daily echo and average rainfall composite chart for August 29.

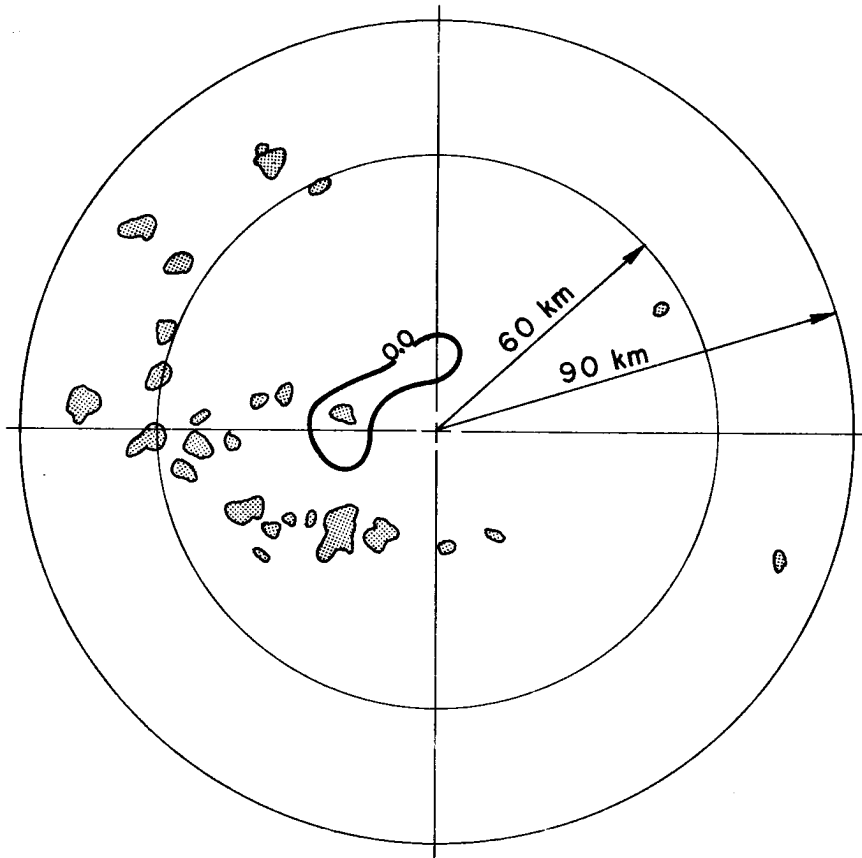


Figure 3.6a 1400-1500 hourly echo and average rainfall composite chart for September 1.

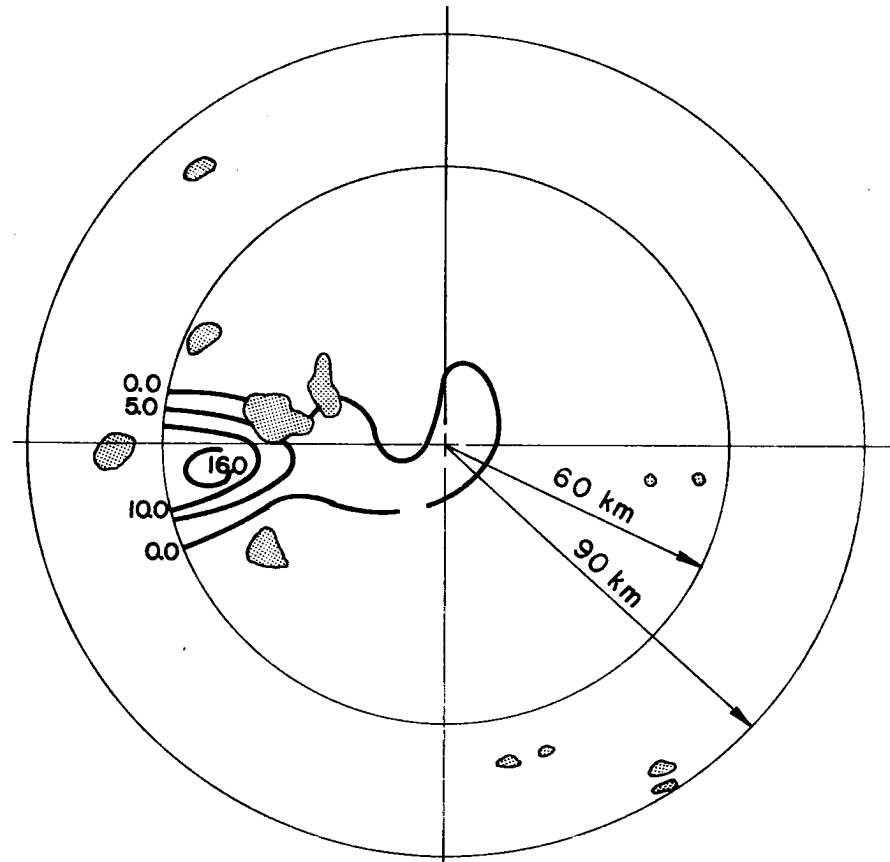


Figure 3.6b 1500-1600 hourly echo and average rainfall composite chart for September 1.

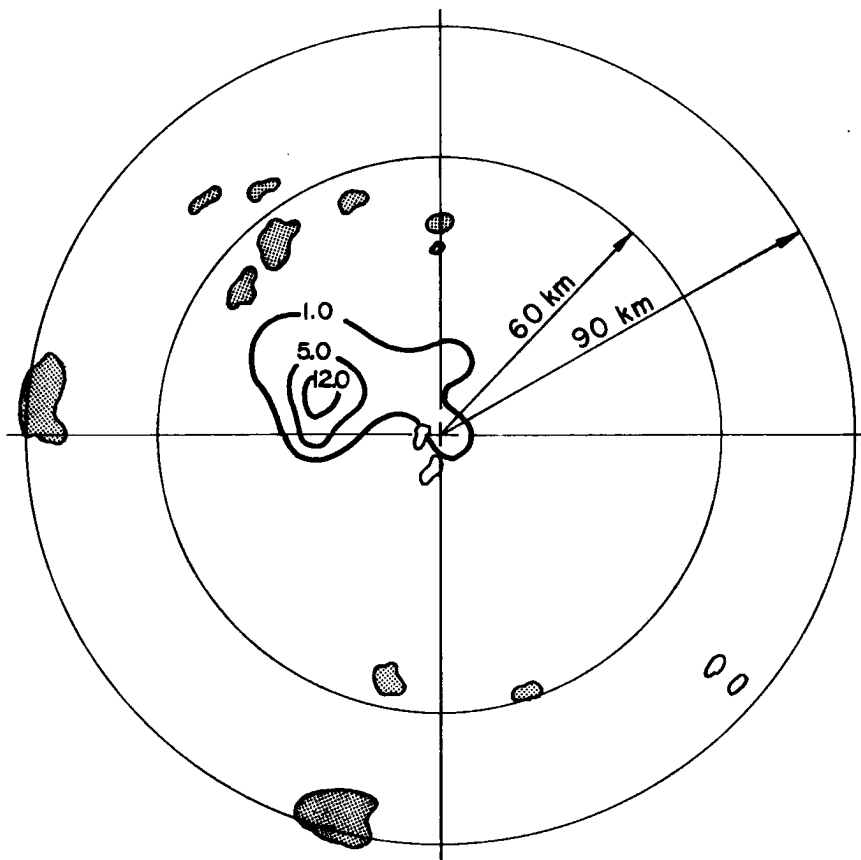


Figure 3.6c 1600-1700 hourly echo and average rainfall composite chart for September 1.

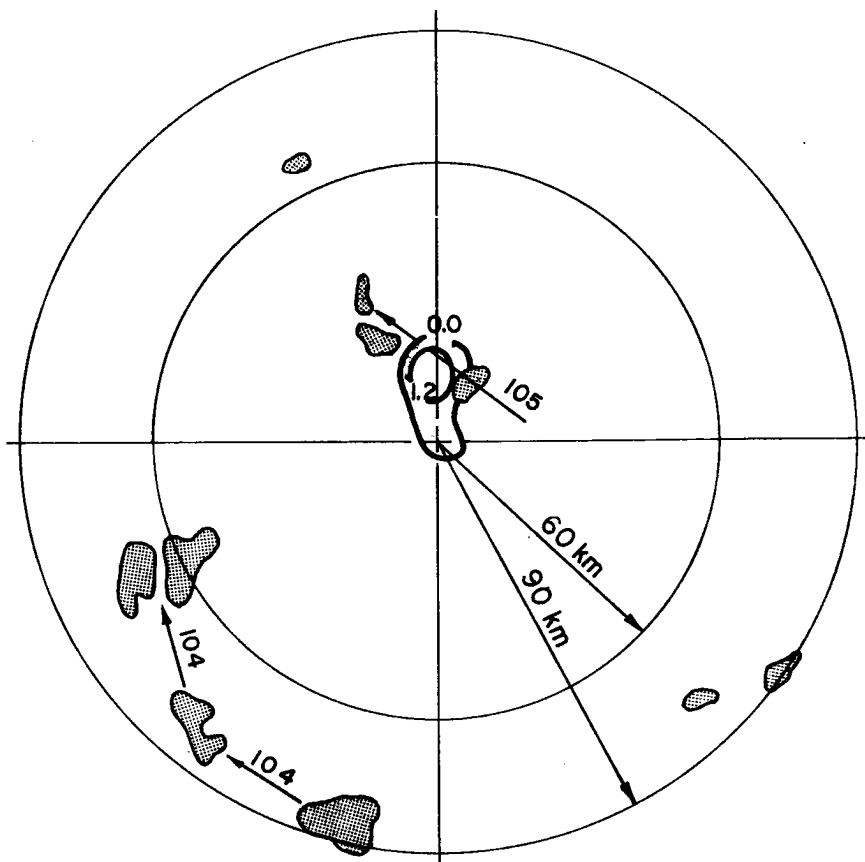


Figure 3.6d 1700-1800 hourly echo and average rainfall composite chart for September 1.

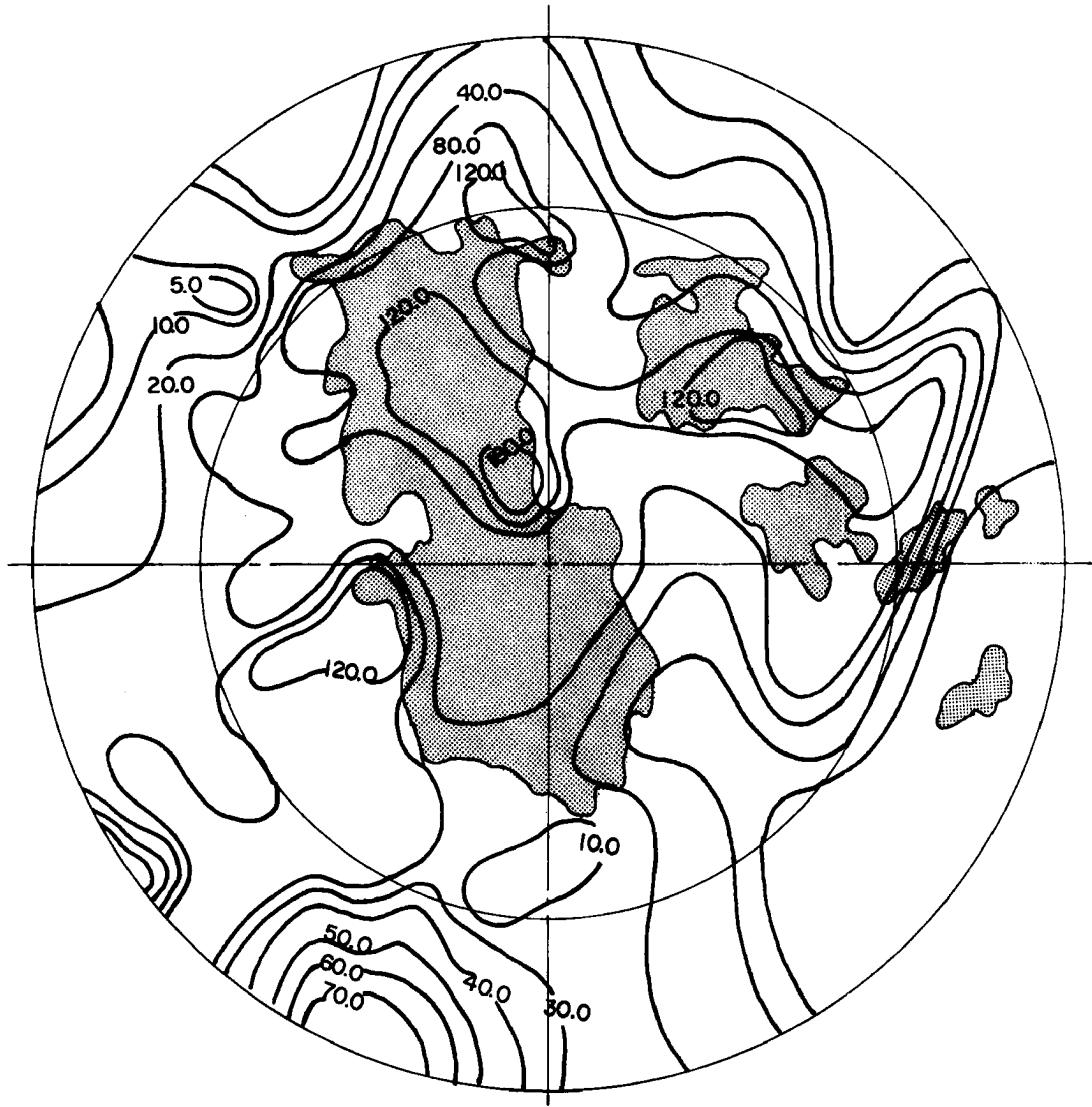


Figure 3.6e Average daily isohyct chart and maximum area of the radar echo for September 1.

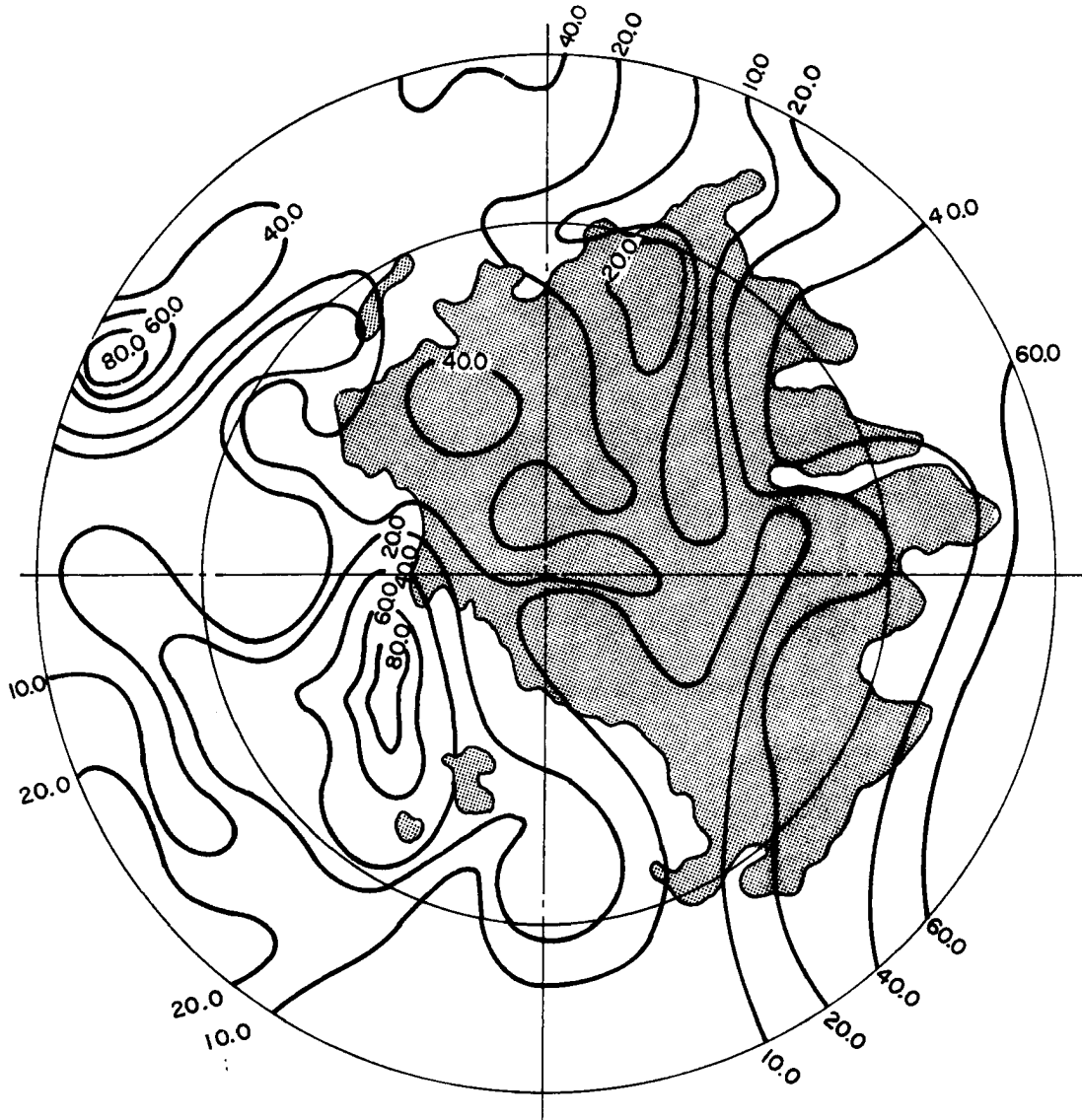


Figure 3.7 Average daily isohyct chart and maximum area of the radar echo for September 2.

an area of about 4767 km² at its peak (0730 LST) while storm 109 had an area of at least 11,655 km², with additional area beyond radar range.

The more significant features resulting after analysis of the mentioned charts for the days chosen can be summarized as follows.

i) The direction of the storms was, in general, from east to west except August 29, when storms 102 and 103 moved from northeast to southwest, and September 1 and 2 when storms 108 and 109 moved very slowly.

ii) Most of the storms show an organized pattern during late afternoon.

iii) In general, individual rainstorms reached maximum intensity an hour or two after formation, then gradually weakened except September 1 and 2.

iv) August 21 and 22 registered their maximum rainfall in an area out of the experimental raingauge network (see daily chart, Fig. 3.5a,b,c, or d). Thus, the continued increase in length of the different storms was due to successive formation of new rainstorm further to the east.

3.3 The Aircraft Data

Aircraft measurements are useful for the study of atmospheric motions and conditions of scales much smaller than can possibly be detected through the standard synoptic upper-air network. Moreover, aircraft data are vastly more valuable if combined with other data forms, particularly in an environment where time series from fixed stations are generated, especially from frequent soundings. In this study, the above conditions were met such that the data derived could be used in order to study some kinematic and thermodynamic features at the top of the sub-cloud layer.

Description of the different aircraft missions chosen in this study are presented next (see section 3.3.1).

Subsection 3.3.2 deals with the divergence and vorticity computation from aircraft data. Subsection 3.3.3 deals with analysis of the horizontal wind, mixing ratio, and temperature as measured by the aircraft. A study about the mesoscale variability of the above parameters at the flight level is also included. Subsection 3.3.4 relates the above analysis with conventional data (synoptic charts and pilot balloon data). Subsection 3.3.5 makes some comments about thermodynamics and dynamic features at cumulus scale.

3.3.1 Description of the Aircraft Missions

The Queen Air aircraft from NCAR carried out twenty-eight missions during VIMHEX II. The missions were decided on daily at meetings arranged at Maracay. Because of the variability of the meteorological phenomena being investigated, the flight plans giving specific tracks to be followed were decided a few hours before the missions were carried out.

The aircraft missions may be classified as convection, radiation or synoptic missions. Each mission consisted of transit from Venezuelan Air

Force "El Libertador" to the chosen experimental area. During the transit flights, special observations were made. The flight track used depended partly on the distribution of cloud to be investigated and partly on the kind of information to be obtained. Three aircraft patterns were essentially used.

- a. North-south pattern
- b. Circle pattern
- c. Cloverleaf pattern.

Figure 3.9 shows the scale and geographical situation of the above patterns.

Pattern a. was basically used to measure state parameters and horizontal winds on an extended north-south profile. The extension covered in most of this pattern was from $10^{\circ}15'N$ $-67^{\circ}39'W$ to $1^{\circ}55'N$ $-67^{\circ}04'W$ at variable heights.

Pattern b. was used to measure state parameters and horizontal winds around the "Central Venezuela Circle" in order to compare with pilot balloon winds. The radial extension covered with its center at Carrizal was about 170 kms flown at 3000 feet.

Pattern c. (the one used in this study) was aimed to measure state parameters and horizontal winds below cloud base by flying a cloverleaf pattern centered $9^{\circ}00'N$ and $67^{\circ}00'W$ with 50 nm sectors. The altitudes during this pattern varied to best conform with the varying cloud bases. The location of the check points during the pattern can be seen in Fig. 3.8.

The nature of the cloverleaf pattern was such that it permitted the measurement of different parameters along and across the main wind (easterly wind). All legs took from twenty to twenty-three minutes flown at 148 knots indicated air speed. The data used are one minute averages so they are representative of a horizontal distance on the ground of 4.6 km.

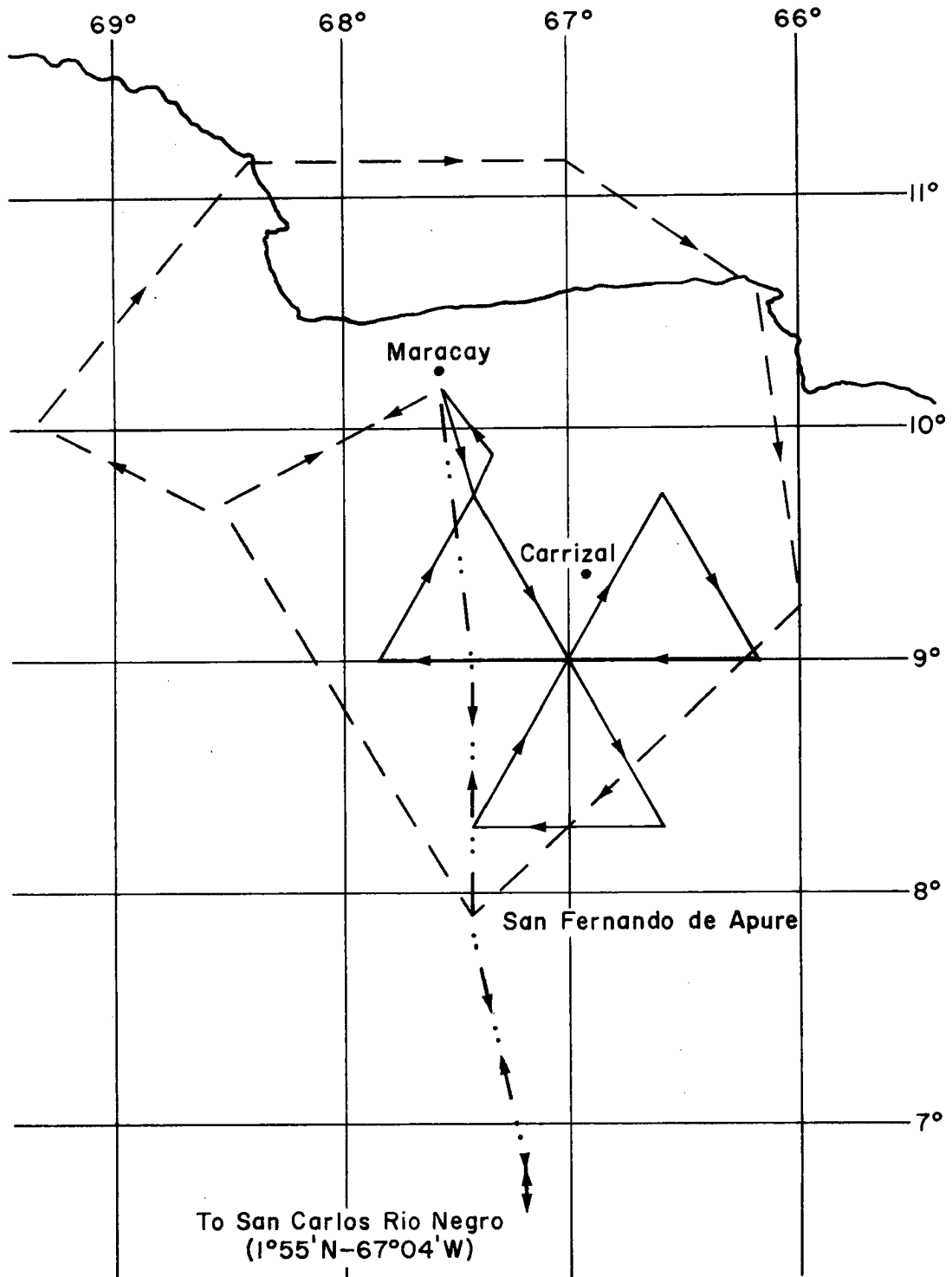


Figure 3.8 Scales and geographical situation fo the north-south (· · —), circle (— —) and cloverleaf (—) aircraft patterns.

There were twelve missions with pattern a., three missions with pattern b., and five missions with pattern c. Of the rest of the missions, eight were dedicated to photo and radiation missions. These did not have specific patterns.

This study made extensive use of the five cloverleaf pattern missions. Only one north-south pattern mission was used. The level, just below cloud bases, used on the former, was chosen in order to keep track of cloud base, and the horizontal variation near the top of the sub-cloud layer. It was also hoped to calculate horizontal divergence at this level (850 mb) (see 3.3.1), but this was not found to be measurable by the Queen Air aircraft in suppressed conditions.

Table 3.2 shows the dates, times, and prevailing conditions during the six flights used and also the soundings launched shortly before, during and after the above missions. Each day has been classified according to the convective regime and rainfall index such as explained in section 3.2.1.

3.3.2 Divergence and Vorticity Computations Based on Aircraft Winds

The horizontal divergence and relative vorticity formulae used in this study were evaluated from the horizontal wind.

By the divergence theorem:

$$\overline{\nabla_h \cdot V} = \frac{1}{A} \oint V_n d\epsilon \quad 3.1$$

and

$$\overline{\nabla_h \times V} = \frac{1}{A} \oint V_t d\epsilon \quad 3.2$$

where A is the area of each triangle described by the Queen Air aircraft, ϵ is the perimeter, V_n is the component of the horizontal wind normal to the perimeter directed outward and V_t is the component of the horizontal wind tangent to the perimeter. The bar over the horizontal divergence and vorticity terms indicates an average over the area A. The line integral is around ϵ at 850 mb.

Table 3.2 Date, time, prevailing conditions and soundings launched during the aircraft mission periods.

DATE (1972)	TIME LST	PLACE	SOUNDINGS		CLOUD		SURFACE WIND DIRECTION (deg)/ SPEED (ms ⁻¹)	WEATHER REPORTED at 850 mb	SYNOPTIC SITUATION At 850 mb (1200 Z)
			N°	TIME	AMOUNT AND TYPE	BASE (mb)			
21 Aug.	1450-1827	Carrizal	274	1500	3/10 CU	803	136/4.5	Rain	A passage of a trough over central part of South America followed by a ridge from the Atlantic.
			275	1623	2/10 CU, CI	833	170/3.5	No Rain	
			276	1748	3/10 AS	852	107/3.5	Rain Shaft	
			277	1905	9/10 CG	879	114/3.0	Light Rain	
22 Aug.	1500-1800	Carrizal	279	1357	3/10 CU, CI	819	90/2.7	Light Rain	
			280	1553	4/10 CU	806	119/4.5	No Rain	
			281	1902	4/10 CU	848	114/3.0	Heavy Rain Shaft	
29 Aug.	1250-1617	Carrizal	296	1259	4/10 CU, CI	849	45/2.5	Rain Shafts	A trough associated with a low pressure at east of Venezuela approach to Carrizal area.
			297	1415	4/10 CU	891	42/5.0	Rain Shafts	
			298	1505	4/10 CU, CI	853	30/4.0	Rain Shafts	
			299	1619	3/10 CU, CI	872	23/3.0	Rain Shafts	
30 Aug.	1354-1728	Carrizal	303	1555	5/10 CU, CS, CI	803	125/2.5	No Rain	
1 Sept.	1420-1743	Carrizal	310	1451	3/10 CG, CI	807	130/3.5	Shower	A trough is located just over Carrizal, moving to the west.
			311	1623	2/10 CU, CI	829	68/1.0	Shower	
			312	1833	4/10 CU	833	217/1.0	Rain	
2 Sept.	1219-1709	North	318	1151	3/10 CU	963	270/1.0	Light Rain	A trough associated with a low-pressure over the Panama Canal has just passed over Carrizal.
		South	319	1707	2/10 CU, CI	925	280/1.0	No Rain	

The above computations were carried out after correction of the wind measurements as described in section 2.4.

The data consisted of wind observations taken a level below the cloud bases. It was evident that the heights of cloud base were different from one mission to another (825-895 mb); however, the computation of divergence and vorticity can be assumed to be representative of 850 mb.

The triangles described by the cloverleaf pattern have been named, for convenience, as I, II and III as seen in Fig. 3.9. It is also convenient to remind the reader that these "leaf sectors" were oriented almost identically for all five missions, with a northeast, a northwest and a north-south triangular sector of 50 N miles each side on each triangle. The three sectors join at the center which was located at 9° - 00N and 67° - 00W .

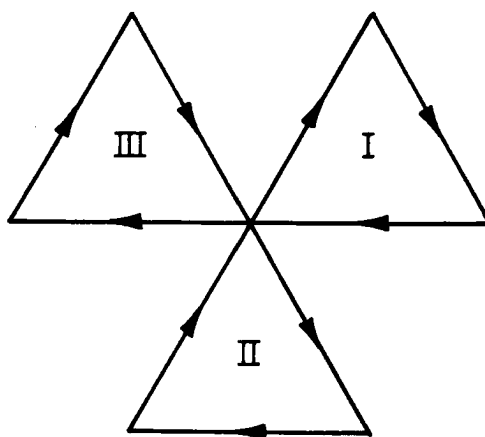


Figure 3.9 Conventional notation for the aircraft cloverleaf pattern used in the horizontal divergence and vorticity calculations.

In order to minimize the error caused by turns of the aircraft at each corner of the cloverleaf pattern, a linear interpolation was carried out close to the corner itself. The procedure is sketched in Fig. 3.10.

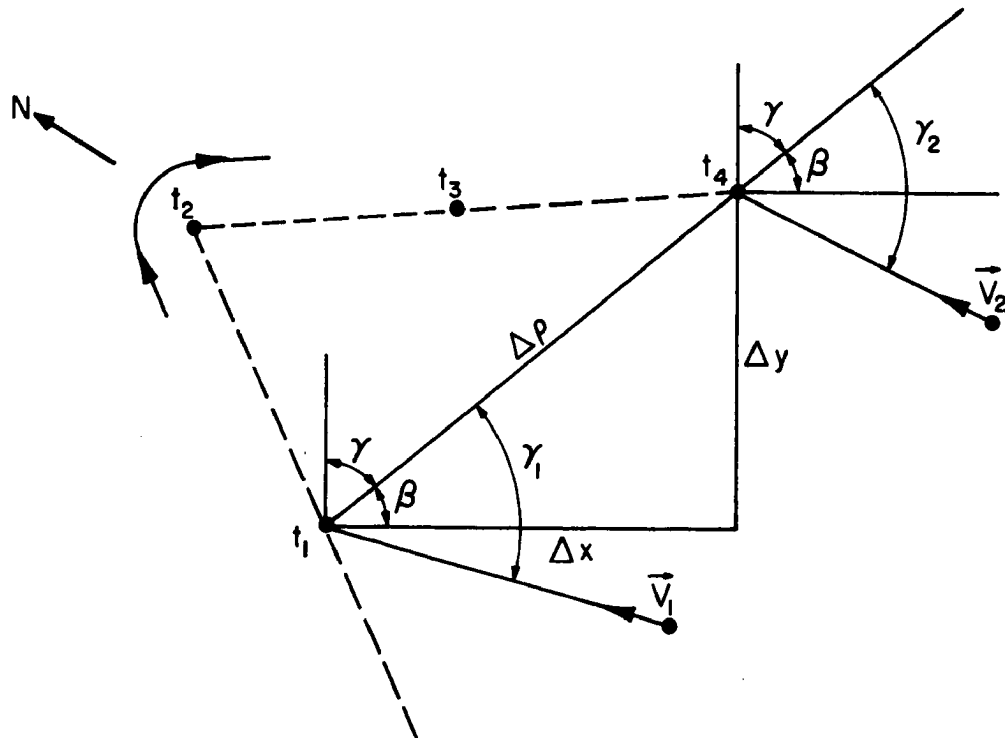


Figure 3.10 Graphical linear interpolation used at each corner of the aircraft cloverleaf pattern in the horizontal divergence and vorticity calculations.

The figure shows the track of the aircraft (dashed line) when it was flying towards the northwest and then turning to an easterly direction. The minute average measurements taken by the aircraft are indicated by $t_1 - t_4$. The purpose of this procedure is to avoid using the winds associated with t_2, t_3 , since these may be influenced by the turn. By taking readings of the aircraft's positions at t_1 and t_4 , Δx and Δy (east and north position) could be determined, and so $\Delta\rho$ and β .

Next, values of the normal and tangent wind components at t_1 and t_4 , were computed from the direction and speed of the wind at t_1 and t_4 (indicated in the above figure by V_1 and V_2). The average of the above components of the winds multiplied by the new $\Delta\rho$ were then used in the computation of the horizontal divergence and vorticity for this corner of each triangle.

A summary of the formulae used following the above procedure appears below.

$$\Delta\rho = \sqrt{\Delta x^2 - \Delta y^2} \quad (3.3)$$

$$\sin \beta = \frac{\Delta y}{\Delta x} \quad \therefore \beta = \sin^{-1} \beta \quad (3.4)$$

$$\text{at } t_1, V_{n1} = |V_1| \times \sin \gamma_1 \quad (3.5a); \quad V_{t1} = |V_1| \times \cos \gamma_1 \quad (3.5b)$$

$$\text{at } t_4, V_{n2} = |V_2| \times \sin \gamma_2 \quad (3.6a); \quad V_{t2} = |V_2| \times \cos \gamma_2 \quad (3.6b)$$

$$\bar{V}_n = \frac{V_{n1} + V_{n2}}{2} \quad (3.7a); \quad \bar{V}_t = \frac{V_{t1} + V_{t2}}{2} \quad (3.7b)$$

This method introduced a small error because it reduced the computation area, but on the other hand, a better accuracy in the normal and tangent components of the wind at the corners was achieved. Moreover, the area reduction was negligible compared with the total area of each triangle.

The computed divergences and vorticities at 850 mb for the five missions are given in Table 3.3.

TABLE 3.3 Values of Horizontal Divergence and Vorticity Determined from Aircraft Measurements on the Days of August.

DATE	TRIANGLE	TIME (LST)	DIVERGENCE	MEAN VALUE	VORTICITY	MEAN VALUE
Month - Day		From - To	Unit: $10^{-6}s^{-1}$	Unit: $10^{-6}s^{-1}$	Unit: $10^{-6}s^{-1}$	Unit: $10^{-6}s^{-1}$
August 21	I	15.32-16.31	1.8		7.9	
	II	16.33-17.36	4.4	-1.3	-0.9	3.5
	[III]	17.38-18.14 [plus] 15.12-15.29	[9.3]	[2.2]	[36.9]	[14.6]
August 22	I	15.32-16.29	4.6		3.3	
	II	16.31-17.25	-5.1	-0.25	1.8	2.5
	[III]	17.27-18.13 [plus] 15.13-15.30	[25.1]	[8.2]	[-37.7]	[-1.1]
August 29	I	13.34-14.30	5.4		-5.7	
	II	14.32-15.25	-3.5	0.95	-2.6	4.2
	[III]	15.27-16.06 [plus] 13.14-13.32	[-4.5]	[-2.6]	[30.7]	[7.7]
August 30	I	14.39-15.33	-2.1		3.6	
	II	15.35-16.33	-5.8	4.0	5.0	4.3
	[III]	16.35-17.12 [plus] 14.19-14.37	[11.2]	[1.1]	[-11.1]	[-0.8]

Because of the big difference in time of the wind measurements on triangle III for each mission, big values of divergence and vorticity obtained were considered meaningless. They are included in the Table 3.3 in brackets in order to show the effect of a greater time difference on the above calculations compared with triangles I and II. Mean values in brackets also correspond to mean values of the horizontal divergence and vorticity after values on triangle III were included.

In general, the four days in which divergence and vorticity computations were computed, were characterized by easterly flow and by a small vertical wind shear at low and middle tropospheric levels over Carrizal. According to the convective regime, and rainfall index range, Aug. 21, Aug. 22 and Aug. 30 were classified as diurnal convection days and Aug. 29 as an enhanced convection day.

After examining hourly and daily echo-rainfall composite charts (see section 3.2.2) for these days and comparing them with the divergence values obtained, it is evident that no relation is found. The maximum value of convergence is found on Aug. 30 in which 0.7 mm of rain were registered in the late afternoon. It is also doubtful if the vorticity estimates are significant. However, the results of this study are significant in two ways.

First, they provide observational support to correction of the wind explained in section 2.4, clearly, small values of divergence on the order of 10^{-6} sec^{-1} reflect the high accuracy of the corrected winds ($\sim 1 \text{ ms}^{-1}$).

Second, although the measured divergence values of 10^{-6} s^{-1} are not significant considering the residual errors in the winds; clearly during undisturbed periods, the low level divergence on this scale is small. (The residual winds errors would probably give errors in the divergence for a triangle of order 10^{-5} s^{-1} .)

3.3.3 Analysis of the Horizontal Wind (Speed and Direction), Mixing Ratio, and Temperature from Aircraft Data.

It was mentioned earlier that all aircraft missions used in this study were carried out just below cloud base. Thus, the information derived from those flights should be representative of conditions at the top of the sub-cloud layer.

3.3.3A Horizontal Wind Analysis

Using corrected winds derived from the aircraft data (850 mb), the basic field was analyzed in the conventional manner (streamlines and isotach analysis) on the days chosen except for September 2 due to the nature of the pattern followed on this day. The area of analysis was approximately equal to that shown in Fig. 3.8. A complete set of the analyses for August 21, 22, 29, 30 and September 1 is presented in Figs. 3.11 to 3.15.

The remarks from this analysis are:

i) The wind direction on Aug. 21, 22, 29 and 30 was mainly from east-northeast while on September 1 it was from south-southeast. The first four days did not show the large variability which was seen on September 1.

ii) The wind speed varied between 5 m s^{-1} and 9 m s^{-1} on the days in August while on September 1 it was less than 5 m/s. The variability was smaller on the days in August than those on September 1.

According to i), the August days may be categorized as a steady regime and September 1, as an unsteady regime. This difference is consistent with the convection categorization earlier described (section 3.2). From ii), it is seen that the August days show a greater wind speed than September 1. Thus, again a consistency is found in the sense that undisturbed days (high speeds) are related to high constancy of the wind while disturbed days (low speeds) are related to low constancy.

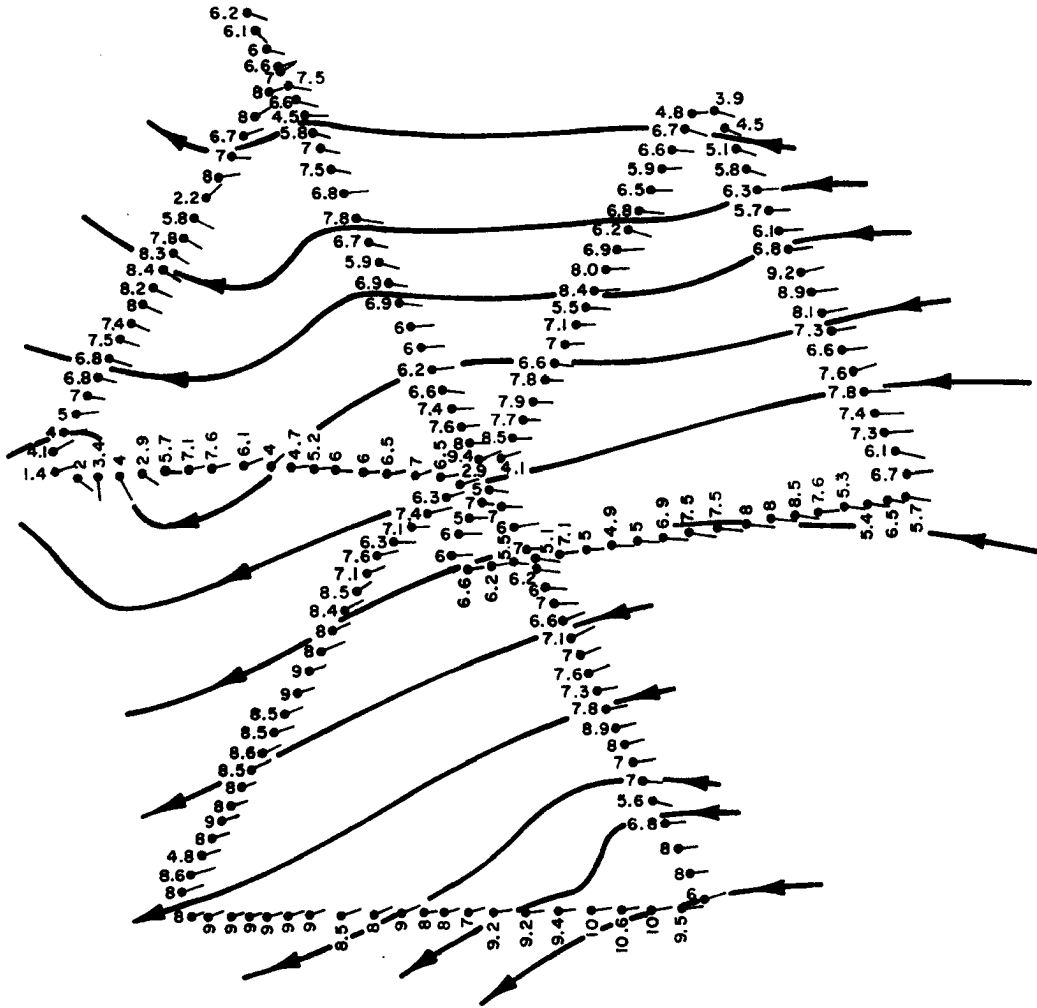


Figure 3.11a Streamlines analysis for August 21.

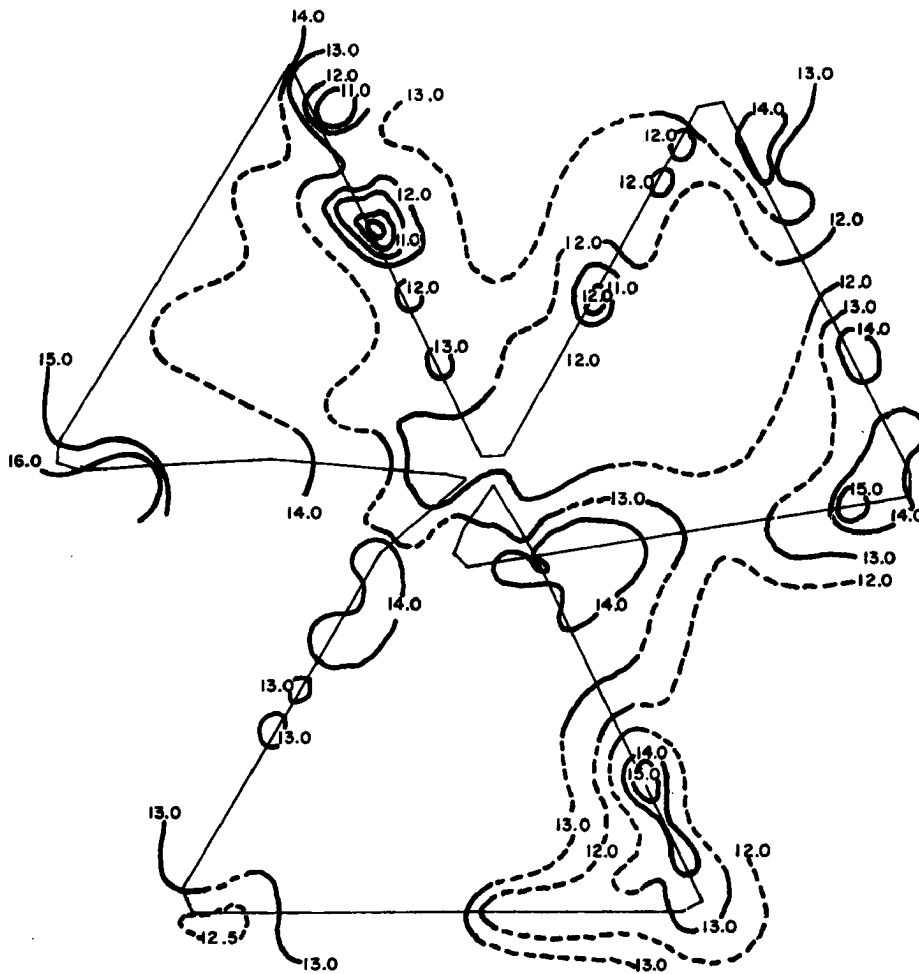


Figure 3.11b Mixing ratio analysis for August 21.

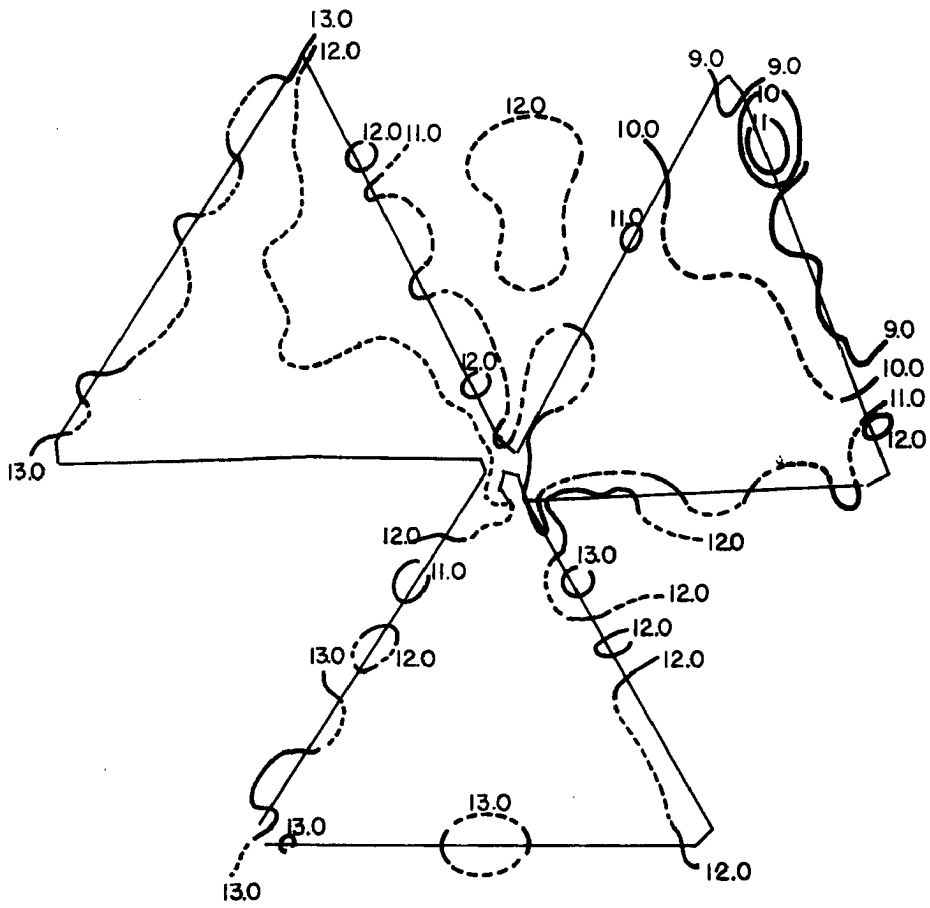


Figure 3.12b Mixing ratio analysis for August 22.

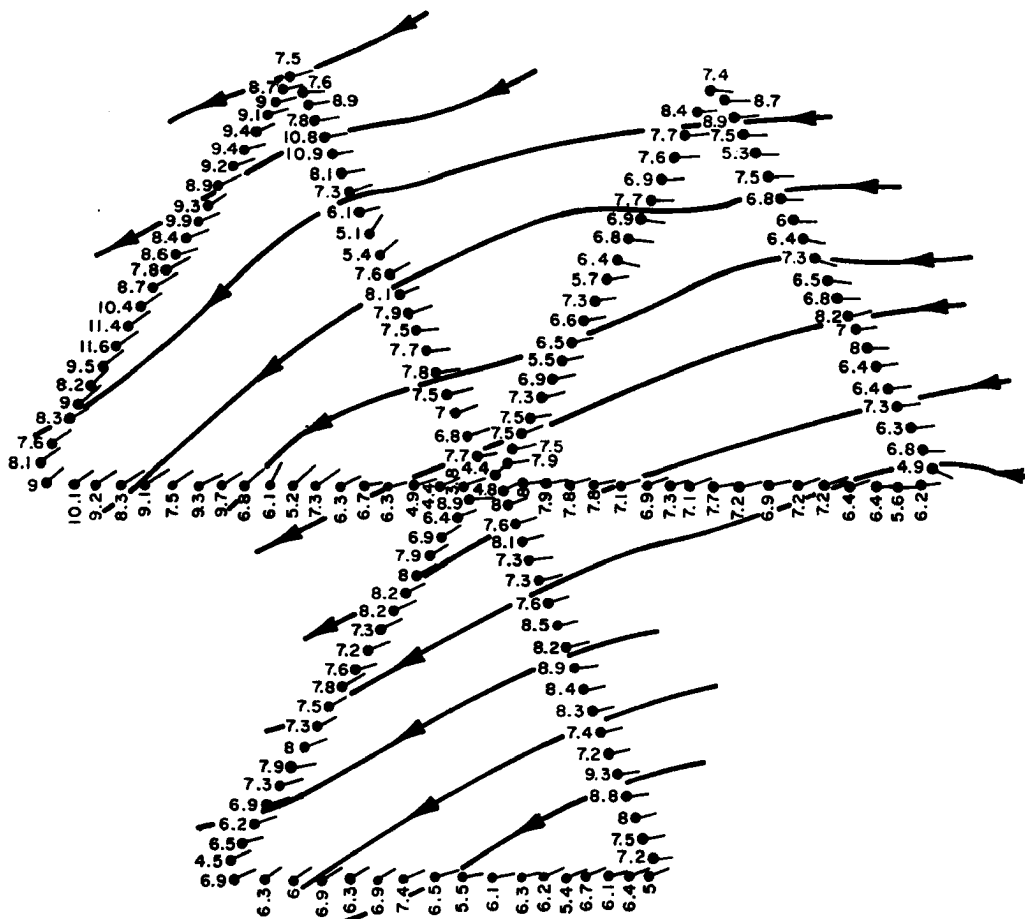


Figure 3.13a Streamlines analysis for August 29.

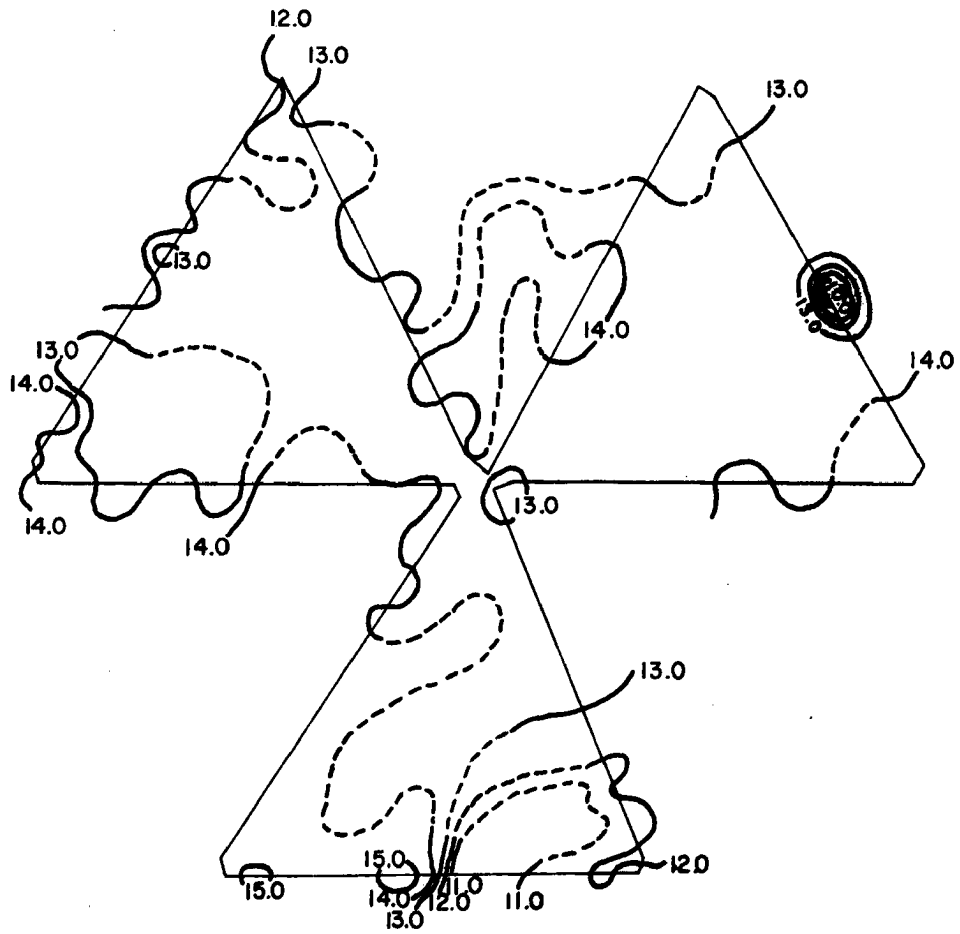


Figure 3.13b Mixing ratio analysis for August 29.

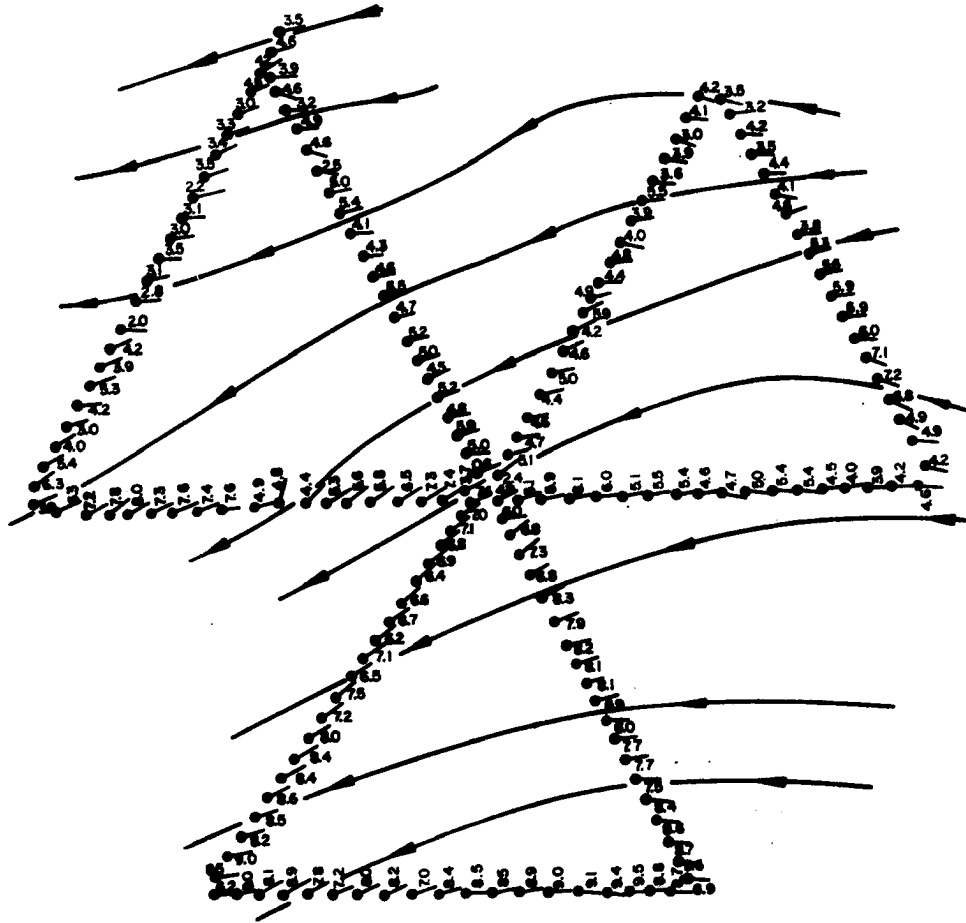


Figure 3.14a Streamlines analysis for August 30.

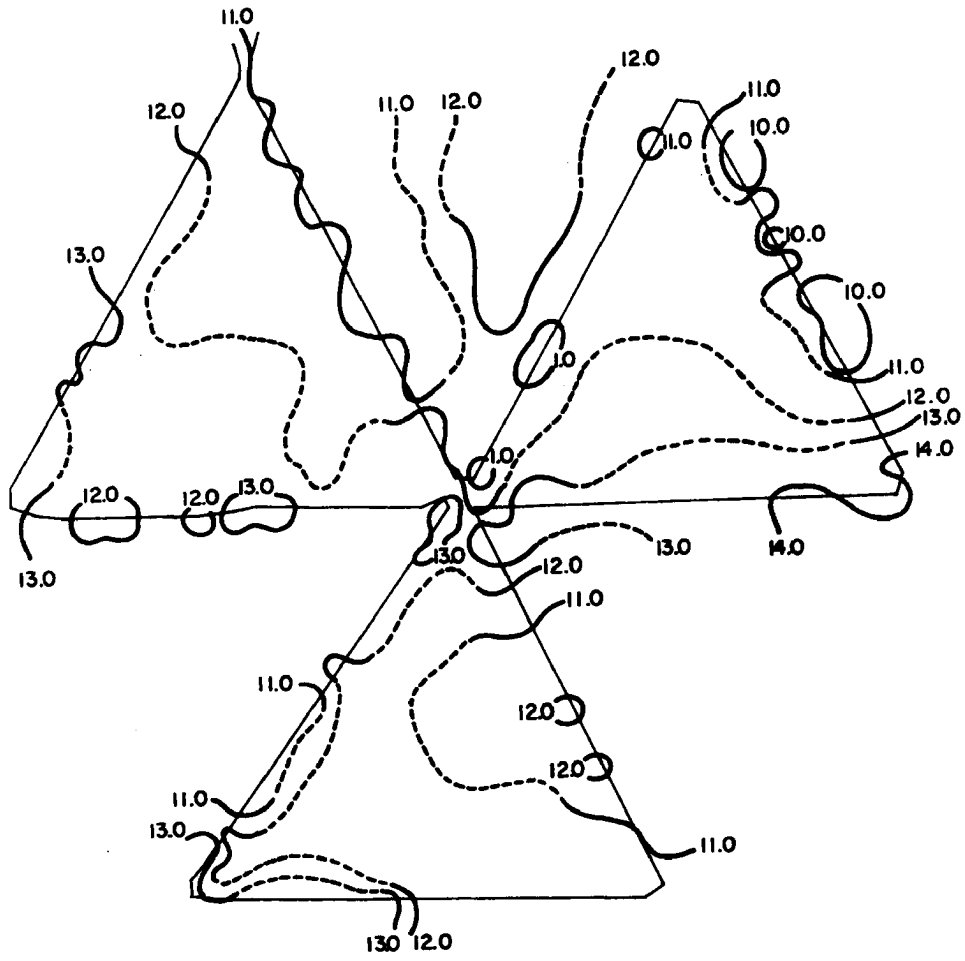


Figure 3.14b Mixing ratio analysis for August 30.

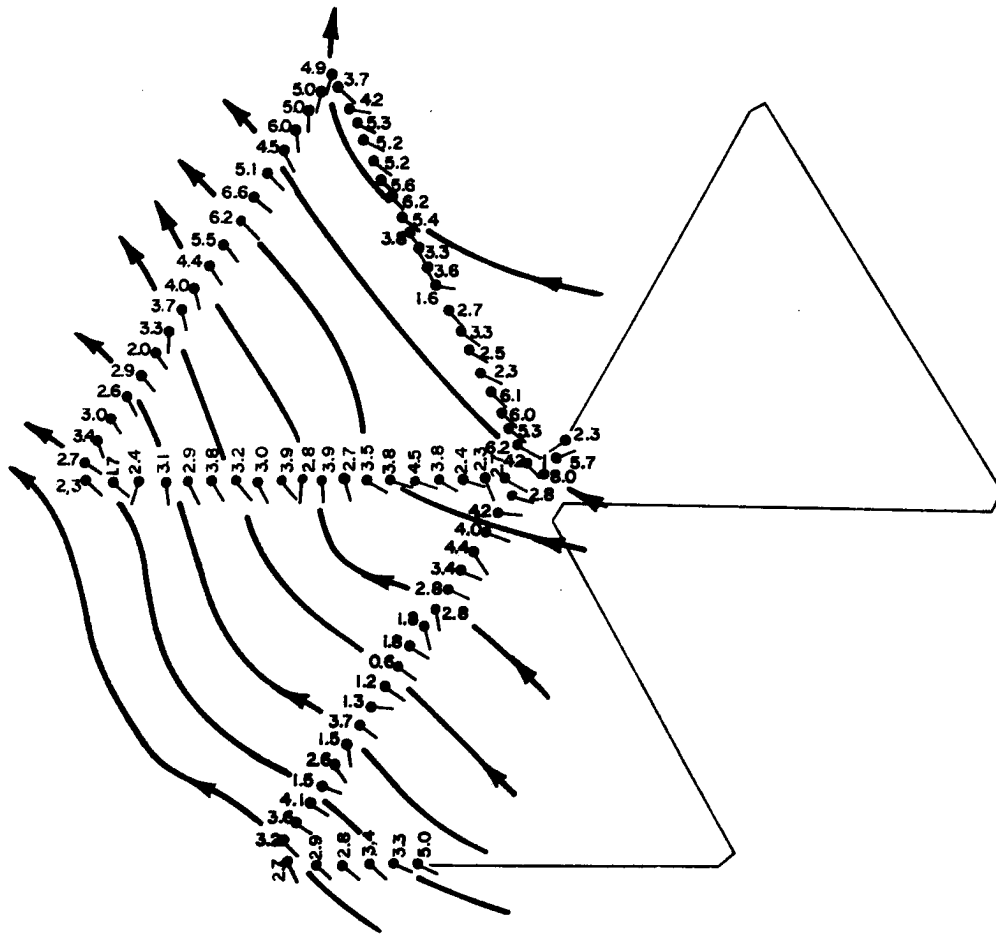


Figure 3.15a Streamlines analysis for September 1.

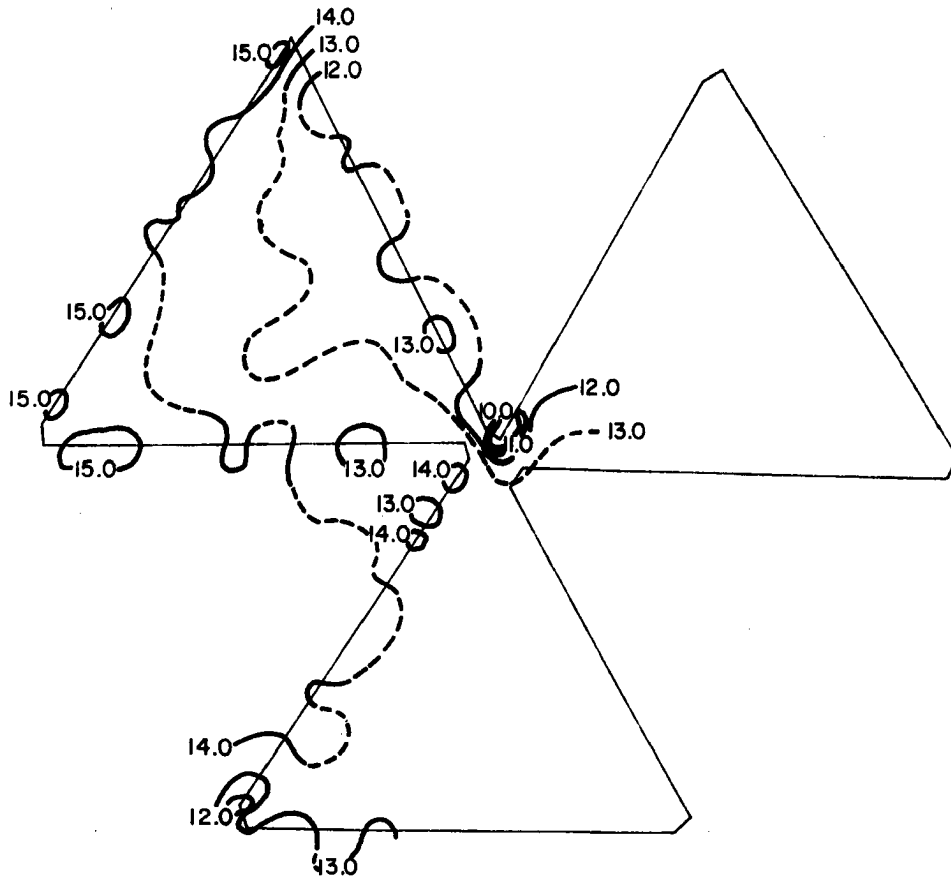


Figure 3.15b Mixing ratio analysis for September 1.

An interesting feature observed from the streamline and isotach analysis on August 21, was the cyclonic curvature associated to low velocities on the northwest triangle. During this time the airplane flew through clouds and rain. This weather condition was reported by the aircraft crew, and also confirmed by the time lapse movie and by the radar. The clouds reported were part of an organized system, specifically storm 86. (See Table 3.1.)

3.3.3B Mixing Ratio (r) and Temperature Analysis (θ , θ_e).

In Chapter 2, section 2.4, it was explained in detail how θ and θ_e were obtained from the aircraft measurements, and also the reasons which permitted us to choose the reverse flow temperature values and the derived θ and θ_e . An explanation was also given for the method used to correct the above parameters as well as the mixing ratio to 850 mb level.

This section will make use of those values after they were plotted each minute along the aircraft path for the mission chosen.

Two kinds of analysis were performed with the mixing ratio, θ and θ_e .

- a. Isopleth Analysis
- b. Statistical Analysis

Only the isopleths of mixing ratio (r) is presented in this study. Because of the small horizontal gradient shown by θ , the corresponding isopleth analysis was difficult to perform.

Statistical analysis consisted primarily of the determination of the means and standard deviations for each leg, for each parameter and for all five flights.

Similarly, the basic field was analyzed in the conventional manner (isopleth analysis) for all days except September 2 for the reasons already mentioned above. The area of analysis was also the same as before. A

complete set of analyses for August 21, 22, 29, 30 and September 1 is presented in Figs. 3.11 to 3.15.

The most striking features found from these analyses are:

Mixing Ratio (r)

i) Throughout all aircraft missions it is seen that there are significant horizontal variations in the moisture field in the order of 1 to 2 g/Kg. The reason for this variation is not well known at the present time. Some are associated with clouds (see 3.3.5) but some may not be. In fact, this sort of variation is difficult to observe by using radiosonde. Although there have been extensive and numerous studies made from aircraft missions in the past, the attention has been concentrated on the vertical variation of the parameters used.

Warner and Telford (1967), in a smaller scale study of convection below cloud bases from aircraft measurements, have shown similar variability; although, their results are related to the fluctuation of the θ in the sub-cloud layer.

ii) The mixing ratio variations are such that they described "wet" and "dry" regions. The time interval between them varies from 5 to 7 minutes (20 to 30 Kms).

iii) After overlapping the streamline analysis over the isopleth of the mixing ratio, it was found that the wet regions appear to correspond to apparent horizontal convergence in the wind.

iv) From mean and standard deviation values computed from each leg, a good correlation is found between large values (wet regions) of the mixing ratio and low cloud bases, as seen by the aircraft crew.

Potential Temperature (θ) and Equivalent Potential Temperature (θ_e)

After comparison of values of r with respect to θ and θ_e for each leg, the following relation is found. Wet regions are related to maximum values of θ_e and to minimum values of θ . Conversely, dry regions are related to minimum values of θ_e and to maximum values of θ . This relation is discussed in more detail in the section of cloud scale study: 3.3.5.

3.3.3C Variability of the Potential Temperature, Equivalent Potential Temperature, Mixing Ratio and Wind (Direction and Speed) Near the Top of the Sub-Cloud Layer.

In order to study the above variability, simple statistical analyses were performed during the five cloverleaf pattern missions. These analyses consisted primarily of computations of mean and standard deviation for each of the above mentioned parameters. All parameters, except the wind, were corrected to 850 mb before being used in the calculations (see section 2.4). The mean and standard deviation for each leg were determined from the cloverleaf pattern. A conventional notation described in Fig. 3.16 was adopted for each leg.

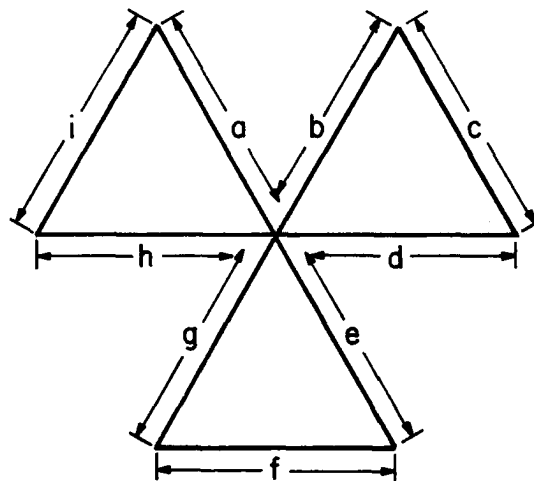


Figure 3.16 Conventional notation for the aircraft cloverleaf pattern used in the study of the variability of θ , θ_e , r and wind (direction and speed) at ~ 850 mb.

Tables 3.4A to 3.4D show a summary for the five days (August 21, 22, 29, 30 and September 1) of the mean and standard deviation for each leg and parameters (θ , θ_e , r and wind direction and speed). The values in the table are probably representative of the mesoscale patterns in the tropics, and are consistent with the earlier mentioned results (see 3.3.2A and 3.3.2B). This variability on the mesoscale indicates that caution is needed in interpreting a single rawinsonde sounding as representative of a large area.

Table 3.4A Mean and standard deviation of r , θ , θ_e , and wind (direction and speed) at 850 mb from the aircraft mission on August 21.

FLIGHT MISSION: August 21, 1972; 17

	LEG	a	b	c	d	e	f	g	h	i
Time	From	1511	1531	1550	1609	1632	1654	1714	1737	1755
	To	1530	1549	1608	1627	1653	1713	1736	1754	1815
r (g/Kg)	Mean	12.0	12.1	13.3	14.0	13.4	13.0	13.2	14.0	14.2
	S.D	1.0	1.0	1.0	1.0	1.0	0.4	1.0	1.5	0.4
θ ($^{\circ}$ K)	Mean	308.4	308.6	307.6	307.3	307.4	307.3	307.5	307.5	307.1
	S.D	0.2	0.3	0.6	0.2	0.4	0.3	0.3	0.8	0.4
θ_e ($^{\circ}$ K)	Mean	344.3	345.1	347.5	348.4	347.5	345.5	347.0	349.5	350.0
	S.D	3.0	2.5	2.0	2.0	2.0	1.0	2.0	4.0	1.1
Wind Dir. (deg)	Mean	95.0	91.0	92.0	93.1	83.0	75.1	69.5	92.5	92.0
	S.D	9.3	7.4	12.0	6.0	11.0	5.3	7.5	32.0	23.5
Wind Speed (ms^{-1})	Mean	7.0	7.0	7.0	6.4	7.0	9.0	8.1	5.0	7.0
	S.D	1.1	1.2	1.4	1.2	1.0	0.8	0.8	1.8	1.7

Table 3.4B Mean and standard deviation of r , θ , θ_e , and wind (direction and speed) at 850 mb from the aircraft mission on August 22.

FLIGHT MISSION: August 22, 1972; 18

LEG	a	b	c	d	e	f	g	h	i	
Time	From	1512	1533	1552	1612	1631	1650	1708	1727	1745
	To	1532	1551	1611	1628	1649	1707	1726	1744	1805
r (g/Kg)	Mean	12.0	11.1	10.3	11.4	12.0	12.5	12.2	12.5	13.1
	S.D	0.4	0.4	1.1	0.6	1.0	0.5	1.0	0.2	0.5
θ ($^{\circ}$ K)	Mean	308.4	308.0	308.0	307.0	307.0	307.0	307.1	307.3	307.3
	S.D	0.4	0.3	0.7	0.2	0.3	0.2	0.4	0.2	0.3
θ_e ($^{\circ}$ K)	Mean	344.0	341.2	339.0	341.1	342.0	344.1	343.0	345.0	347.0
	S.D	1.2	2.5	3.0	2.0	2.0	1.3	3.2	0.6	1.2
Wind Dir. (deg)	Mean	87.0	87.2	92.0	80.3	92.0	91.0	80.0	81.0	101.4
	S.D	17.0	9.1	10.4	5.0	9.0	7.0	7.0	7.0	17.5
Wind Speed (ms^{-1})	Mean	5.0	5.2	6.2	5.4	6.0	5.5	6.0	6.5	5.1
	S.D.	1.0	1.0	1.1	0.5	0.5	1.1	1.0	1.0	1.0

Table 3.4C Mean and standard deviation of r , θ , θ_e , and wind (direction and speed) at 850 mb from the aircraft mission on August 29.

FLIGHT MISSION: August 29, 1972; 23

LEG	a	b	c	d	e	f	g	h	i	
Time	From	1313	1333	1354	1314	1431	1450	1507	1527	1545
	To	1332	1353	1413	1430	1449	1506	1526	1544	1607
r (g/Kg)	Mean	13.2	13.4	13.0	13.5	13.0	12.5	14.0	13.3	12.2
	S.D	1.0	1.0	1.3	0.5	1.0	2.0	0.3	7.4	1.0
θ ($^{\circ}$ K)	Mean	307.4	307.2	307.0	307.1	307.3	307.0	307.4	307.3	307.5
	S.D	0.4	0.4	0.3	0.4	0.3	0.1	0.3	0.4	0.4
θ_e ($^{\circ}$ K)	Mean	347.0	347.3	345.1	349.4	347.1	346.5	351.4	349.2	346.1
	S.D	2.6	2.2	4.0	1.1	2.0	5.5	0.7	2.1	2.4
Wind Dir. (deg)	Mean	75.4	81.5	91.0	77.3	77.0	70.4	66.1	61.0	61.0
	S.D	13.1	11.2	9.0	7.0	4.4	7.5	9.0	14.0	9.0
Wind Speed (ms^{-1})	Mean	8.0	7.0	7.0	7.1	8.0	6.3	7.4	7.2	9.0
	S.D	1.4	0.1	1.0	0.7	1.0	0.6	1.0	2.0	1.1

Table 3.4D Mean and standard deviation of r , θ , θ_e , and wind (direction and speed) at 850 mb from the aircraft mission on August 30, 1972.

FLIGHT MISSION: August 30, 1972; 24

LEG		a	b	c	d	e	f	g	h	i
Time	From	1417	1438	1458	1517	1535	1554	1613	1634	1653
	To	1437	1457	1516	1534	1553	1612	1633	1652	1713
r (g/Kg)	Mean	11.5	12.0	11.2	13.5	12.0	12.3	12.0	12.4	12.5
	S.D	0.7	0.5	1.2	0.6	0.7	1.0	1.1	0.5	1.0
θ ($^{\circ}$ K)	Mean	308.0	308.0	308.0	307.0	307.1	307.0	307.6	308.0	308.3
	S.D	0.2	0.2	0.6	0.6	0.2	0.2	0.4	0.2	0.6
θ_e ($^{\circ}$ K)	Mean	343.0	343.0	341.4	347.0	342.0	344.0	344.0	345.2	346.0
	S.D	2.4	1.4	3.0	1.1	2.2	3.0	3.1	1.3	2.0
Wind Dir. (deg)	Mean	88.0	85.0	95.1	86.0	82.0	82.6	62.0	63.0	75.0
	S.D	11.4	15.0	12.5	8.4	14.0	1.0	10.0	13.3	11.2
Wind Speed (ms^{-1})	Mean	5.0	4.3	5.0	5.1	8.0	8.4	7.5	6.3	4.0
	S.D	1.0	1.0	1.2	1.0	1.0	1.0	1.0	1.4	1.1

Table 3.4E Mean and standard deviation of r , θ , θ_e , and wind (direction and speed) at 850 mb from the aircraft mission on September 1, 1972.

FLIGHT MISSION: September 1, 1972; 26

LEG	a	b	c	d	e	f	g	h	i
Time	From	1441					1635	1655	1714
	To	1501					1654	1713	1732
r (g/Kg)	Mean	13.0					13.5	14.0	14.1
	S.D	0.6					1.0	1.0	0.5
θ ($^{\circ}$ K)	Mean	308.0					306.8	307.0	307.0
	S.D	0.4					0.5	1.0	0.3
θ_e ($^{\circ}$ K)	Mean	346.0					348.4	347.5	348.4
	S.D	2.0					3.1	2.0	1.2
Wind Dir. (deg)	Mean	129.2					124.0	146.0	155.2
	S.D	15.0					21.0	28.3	20.0
Wind Speed (ms^{-1})	Mean	4.4					3.0	3.1	4.3
	S.D	1.4					1.1	1.0	1.4

The results obtained in this section are related to the 850 mb chart and pilot balloon data in subsection 3.3.4 while subsection 3.3.5 deals with some cloud scale features.

3.3.4 Relating Streamline Analysis from Aircraft Wind Measurements to 850 mb Chart and Pilot Balloon Data

A comparison of streamline analysis from aircraft wind measurements with conventional data was carried out in order to see how well these analyses agree. It is evident that some caution had to be taken due to the different scales involved. Each aircraft mission for the days chosen was studied with respect to the 850 mb chart and pilot balloon analysis corresponding to 0800 LST (1200 Z). The two last analyses are not shown in this study due to space limitations. Therefore, only a short comment about the resulting findings is presented. On all days, a general agreement in the direction of the wind was found. Again, the three analyses show that during the days in August (21, 22, 29 and 30) the wind was mainly from the east while on the days in September (1 and 2) the wind was from the south-southwest. That confirmed the discussion in section 3.2 and section 2.2.

Naturally, in order to detect small mesoscale features around the Carrizal area, the streamline analysis from the aircraft wind data clearly showed a better resolution than the other two analyses.

The synoptic situation on September 1 and 2 is discussed with more detail in Chapter 4.

3.3.5 Some Comments About Dynamic and Thermodynamic Features at Cumulus Scale

During the different aircraft missions, there were several occasions in which the aircraft flew through clouds and rain for a relatively short

time (2 to 5 minutes). The aircraft report (including time lapse movie), as well as radar information were used to locate these features exactly. Although it is not the main purpose of this study to deal with the cumulus scale, these provided, as will be seen later, evidence to support the hypothesis that coupling between the cloud layer and the region close to the top of the sub-cloud layer is more common than was previously believed for the undisturbed atmospheric states. Chapter 4 shows definitely that it becomes more intense for disturbed states.

The atmospheric conditions during the aircraft measurements were discussed in section 3.2.1. However, the reader is reminded now that the measurements were performed on days with some developing cumulus clouds. The stratification of the atmosphere in the layer in which the convective motions were observed is characterized by a superadiabatic lapse rate in the layer up to 980 mb from the surface. From 980 mb up to the height of the lower cloud base, an almost adiabatic layer is observed; with increasing height the stability again decreases.

The flight plans were described in section 3.3. In this section, winds relative to clouds were used. The motion of the clouds along the aircraft track were assumed to be the same as the motion of the corresponding radar echoes (or those closest in time and space).

Initial aircraft measurements of the wind field were relative to the earth. To obtain a u and a v component of the wind field relative to the cloud system, the storm system velocity (from the radar) was subtracted from the wind field and the resulting relative u and v components were resolved into direction and speed of the relative wind.

The general procedure was then to combine all of the above features and to study their variation on different legs of flights where cloud and rain were present through the aircraft path.

3.3.5A Individual Cases of Study

During the flight mission carried out on August 21, there were two opportunities in which the aircraft flew through clouds and rain. The relative wind was determined based on storm 86 which was moving from east to west, at 12.9 m s^{-1} . This storm at its peak (1745 LST) had an area of 368 km^2 (see hourly and daily echo-rainfall composite chart, subsection 3.2.2).

The first case of study corresponds to a section flown during 15 minutes when the aircraft was flying in an east-west direction, covering a horizontal extension on ground of about 60 kms (see Fig. 3.17). The plotted wind values are averages for the preceding minute of flight. This flight section was interesting because of the penetration made by the aircraft through an east-west line of small cells during the above time. This line of cells was not part of any organized system. It died shortly after the aircraft penetrated it. According to the aircraft report, the next sequence of weather features was observed before, during and after the penetration. At 1745 LST, a rain shaft was reported directly ahead. At 1749 LST, the aircraft turned to the left to avoid the rainshaft. At 1750 LST, it was flying through light rain, and at 1751 LST entered into a cloud, leaving it one minute later.

Because of the poor visibility observed in the time lapse movie during the last six minutes, it was only possible to detect the position of the clouds and rain area by means of the radar echoes and the aircraft report.

In general, all parameters studied during this flight section show an increase, except θ , which shows a decrease along the section. The relatively small fluctuations in the temperature suggest cold conditions in the cloudy area and warmer conditions in between.

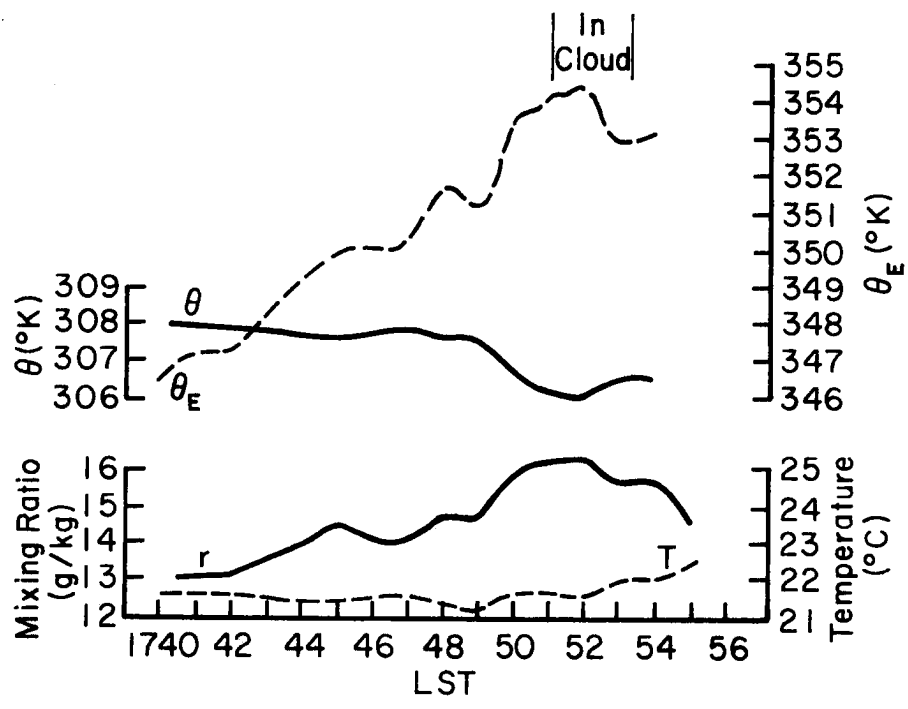
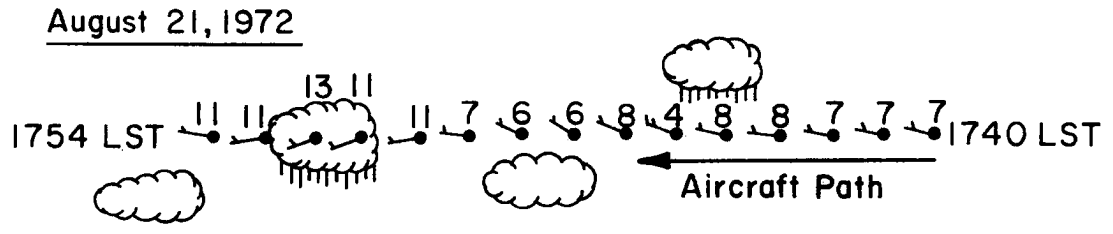


Figure 3.17 Variations of T , θ , θ_e , r and relative wind as measured by the aircraft through clouds and rain at 850 mb on August 21 (1740-1758 LST).

Thus, these warm regions may be interpreted as descending motions, generated by developing clouds. Just under cloud (1751-1752 LST), a high value of θ_e indicates that the air comes from below. The cold and wet conditions are caused by evaporation of rain droplets.

The maximum relative wind (13 m/s) indicates that the increase in the mixing ratio is not only due to the evaporation of rain droplets but to the horizontal convergence of moisture. The outflow of moisture just in cloud (2 g/Kg) may suggest that the cloud had an active region to the right of the aircraft path while it was dying to the left.

The second case of study on the same day corresponded to a section flown for 15 minutes when the aircraft was flying from a southwest to northeast direction, covering a horizontal extension on the ground of about 60 kms (see Fig. 3.18). During this section, the aircraft flew through cloud and rain. This cloudy area was part of the storm 86 shortly after it reached its peak. From 1808 to 1809 LST, the aircraft ran into clouds and rain, while at 1810 LST it was out of the main rainshaft with fair visibility but still with light rain. From the time lapse rate movie, poor visibility was observed from 1805 LST until the end of the flight section.

The high value of θ_e just under cloud may be explained by the ascending air. The wet and cold conditions as seen by the mixing ratio and the potential temperature may also be explained by the evaporation of the droplets of rain.

The maximum wind speed (11.0 m s^{-1}) showed by the relative wind at 1809 LST followed by a minimum (5.0 m s^{-1}) at 1810 LST is suggesting that an active region of the storm is approximately located at the right side of the flight while at the left side the system was dying. Some evidence

August 21, 1972

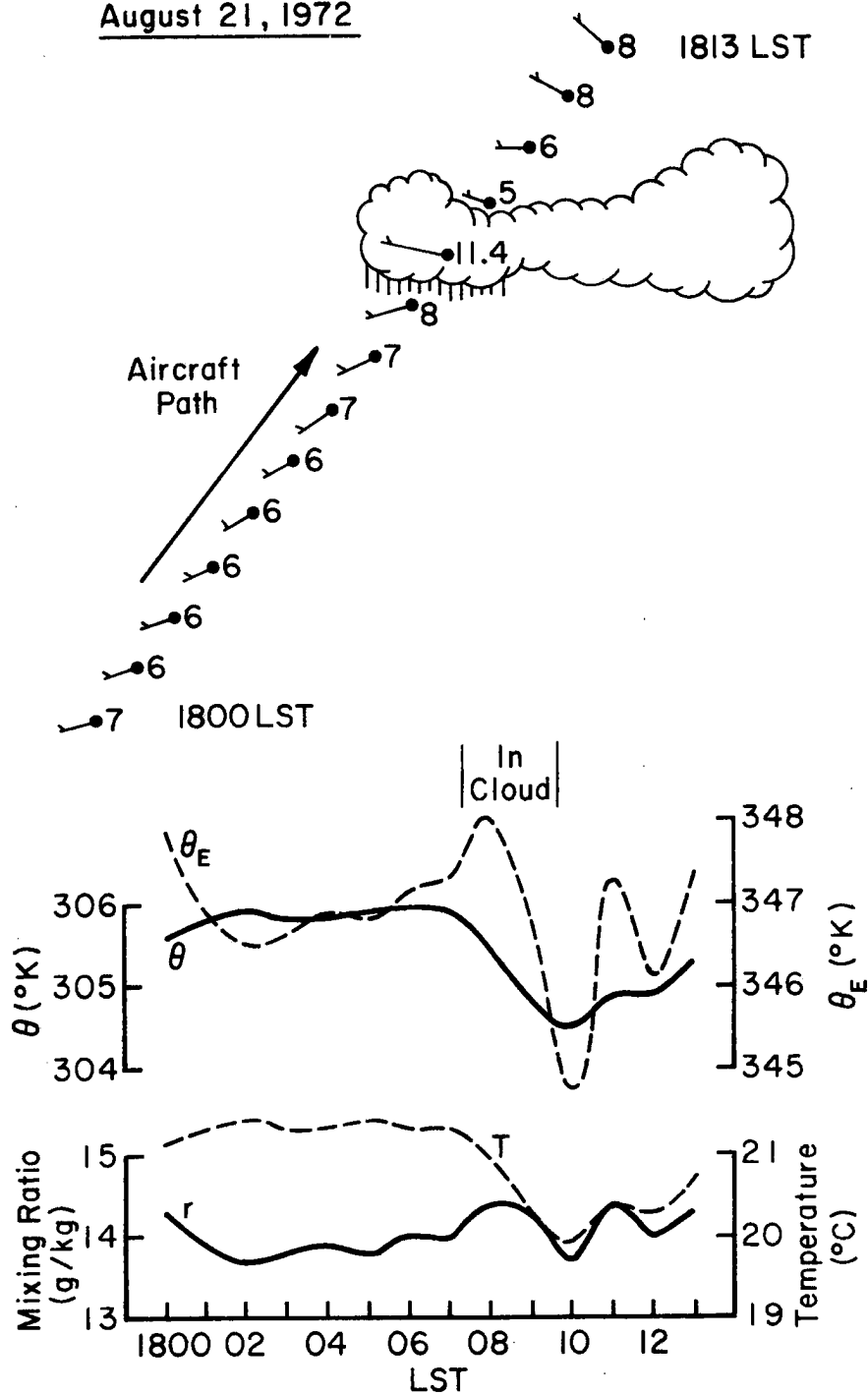


Figure 3.18 Variations of T , θ , θ_e , r and relative wind as measured by the aircraft through clouds and rain at 850 mb on August 21 (1800-1813 LST).

of this mechanism can be seen on the hourly echo-rainfall composite chart which showed a maximum precipitation between 1810 and 1815 LST below the area in study.

An interesting feature observed during this section is the sharp drop in the equivalent potential temperature shortly after the cloud area (1810 LST). This drop in the θ_e can be adduced to a mechanism related to a weaker example of cloud layer-subcloud layer coupling which would hardly be observed at the surface. At 1800 LST, the echo-rainfall composite chart showed an east-west band of rainfall of about 90 km (which included Carrizal and the cloud area reported by the aircraft) along the path of the storm 86. The series of soundings (see section 3.2.1) launched at Carrizal at the above time show a consistent change with the features reported and measurements taken by the aircraft along this section.

During the flight mission carried out on August 29, there were two occasions during which the aircraft flew through clouds and rain. One of these is presented next. The relative wind used was based on the mean storm characteristics (storms 99 and 100, see subsection 3.2.2) which moved from east to west at 10.8 m s^{-1} .

The third case of study corresponded to a chosen section flown from the northeast to southeast, during nine minutes from 1316 to 1324 LST covering a horizontal distance on the ground of about 42 km (see Fig. 3.19).

According to the aircraft report (confirmed by the time lapse movie), shortly before the above section was flown, at 1313 LST, numerous rain shafts were seen in every quadrant as well as heavy cirrus. Visibility was unlimited. At 1317 LST, visibility started to decrease reaching a minimum at 1320 LST. According to the soundings launched at Carrizal, a

August 29, 1972

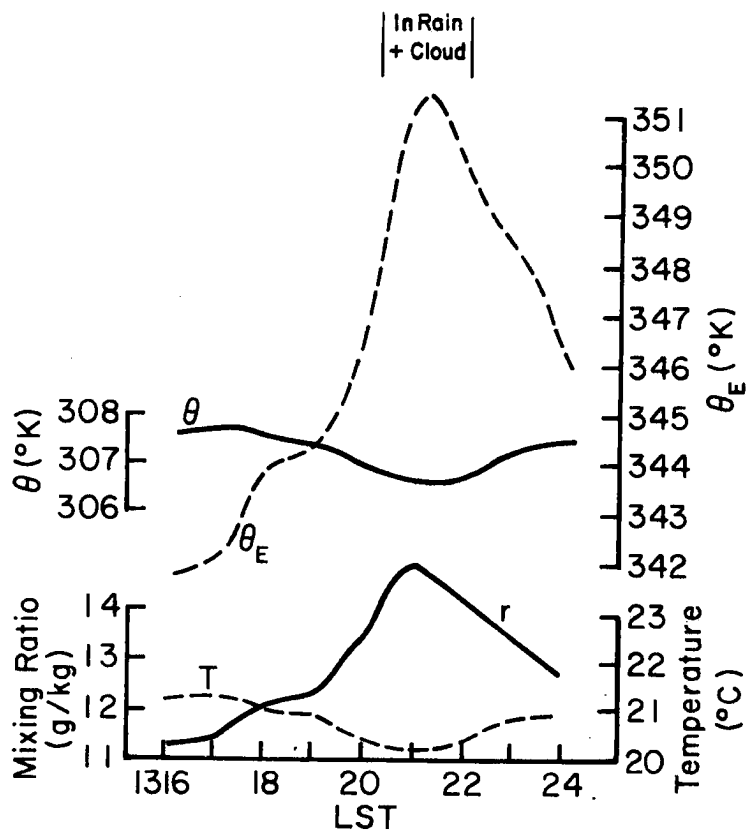
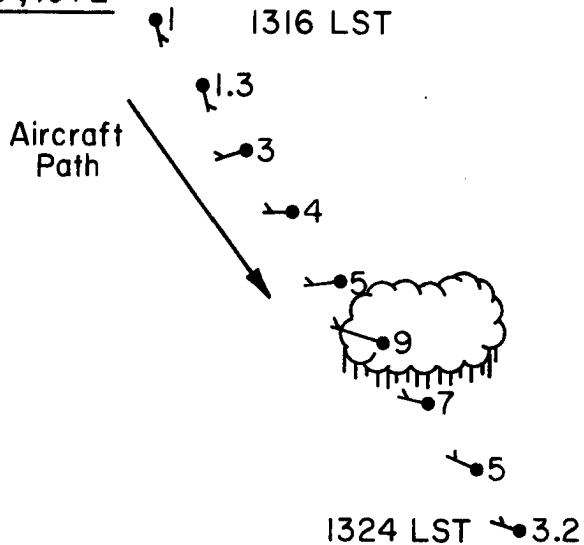


Figure 3.19 Variations of T , θ , θ_e , r and relative wind as measured by the aircraft through clouds and rain at 850 mb on August 29 (1316-1325 LST).

decrease in height of the LCL was observed from 851 mb at 1259 LST to 890 mb at 1415 LST (see Fig. 3.2). This feature explains how the developed clouds observed were warmer than the surrounding air due to condensation at the cloud base, particularly in the period of development of convective motion.

The above feature is confirmed by the increase of θ_e at 1321 LST, just under the cloud studied. A high value of θ_e (351.4°K) indicated that the air comes from below. The wet and cold conditions as seen by r and θ , means evaporation of the droplets of rain. The maximum relative wind (9.0 m s^{-1}) and the moisture outflow might indicate that the cloud was active to the left of the flight path and dying to the right of the flight path. Most of the precipitation caused by this cloud evaporated before it reached the surface as can be seen from the hourly echo-rainfall composite chart.

On September 1, there were again two occasions during which the aircraft flew through clouds. Only one case is presented in this section.

The fourth case of study corresponded to a flight section flown from 1715 LST to 1725 LST; it was flown in a southwest-northeast direction covering a horizontal distance on the ground of about 46 km (see Fig. 3.20). The line of cells penetrated by the aircraft during this sector belonged to the storm 104 which moved from southeast to northwest direction. This storm at its peak (1830 LST) had an area of about 503 km^2 . Because of that, it is believed that the penetration made by the aircraft through the system corresponds to this development stage. The penetration through the line of cells occurred during the last two minutes (1719-1720 LST). Some rain was reported to the west during the penetration time. From

September 1, 1972

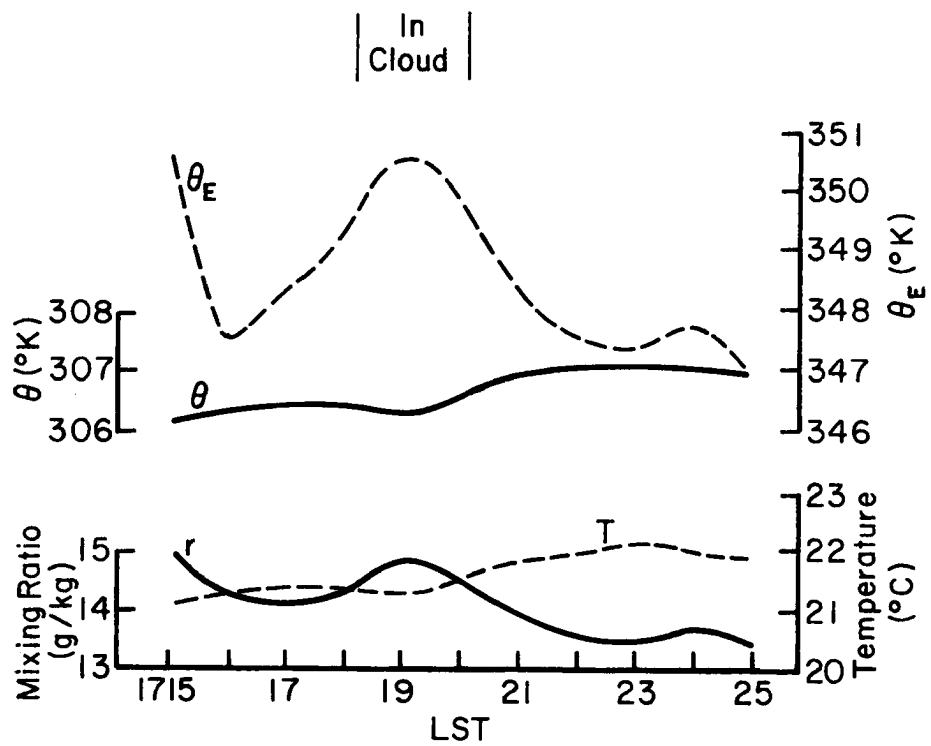
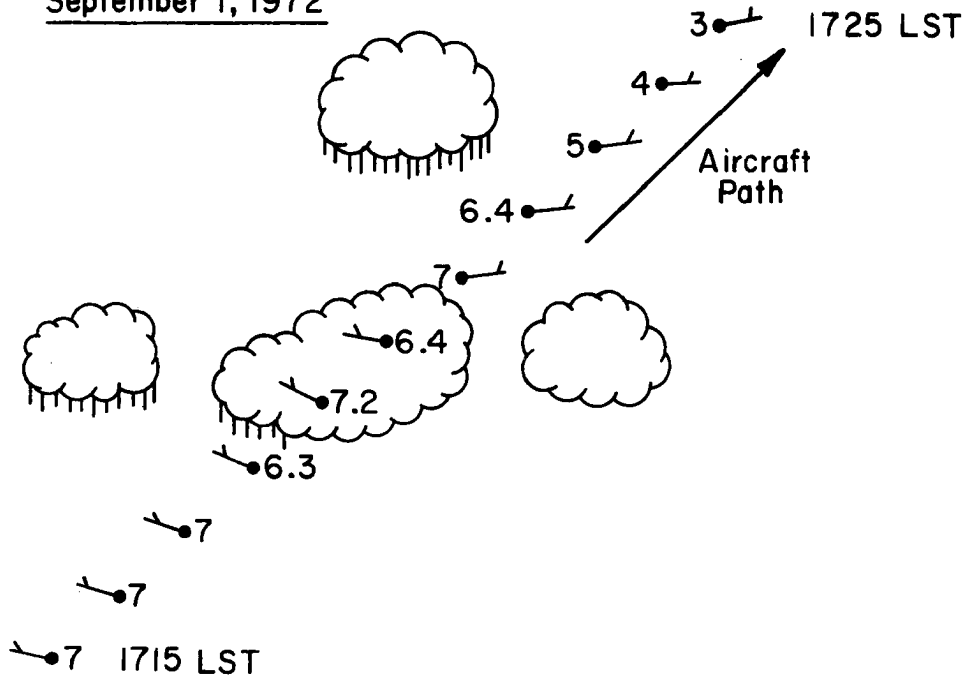


Figure 3.20 Variations of T , θ , θ_e , r and relative wind as measured by the aircraft through clouds and rain at 850 mb on September 1 (1715-1725 LST).

1721 to 1725 LST, a clear area was reported to the right of the aircraft path while rain was reported to the left of the aircraft path.

The observed increase in θ_e and r with a slight decrease in θ just under the cloud are indicative of ascending air currents and the evaporation of the droplets of rain. Increase in θ and decrease in r and θ_e , from 1721 to 1725 LST (clear area) suggest the presence of descending motions. They are possibly caused by developing clouds.

The above variations of θ , r and θ_e from 1721 to 1725 LST, although small, could be interpreted as warm currents derived from descending motions.

Of significance in this flight section is the cyclonic shear observed in the relative wind from the cloudy to cloudless area. Because the wind variations are large, it was concluded that the above variations occur with cloudy areas.

3.3.5B Discussion of Results

The results of the flight level data, although relatively crude, suggest that in cloudy areas, the wind, temperature and mixing ratio are well correlated. This correlation was such that the mixing ratio increased as well as the equivalent potential temperature. A decrease in the potential temperature and a shift and increase in the direction and magnitude of the relative wind were also observed in the above area.

These findings suggest a confirmation of the hypothesis that coupling between the cloud layer and the sub-cloud layer occurred more frequently than was previously believed for the undisturbed atmospheric conditions and that it became more frequent and more intense for disturbed conditions. The mechanism responsible is hard to observe possibly because the subsiding air rarely penetrates the full depth of

the subcloud layer. The main limitation of the present study is due to the one minute average data which was used. Measurements of the different parameters could only be computed from each 4.6 km on the ground. This kind of resolution, of course, is not adequate enough to perform cloud studies accurately.

These results give some indication of the varied and complex processes which occur under and through clouds and rain. They show that the associated variation in temperature, humidity and wind are significant and measureable even in relatively undisturbed conditions. However, it is difficult from a few line cross-sections to build up a complete picture of all the interactions involved.

4. MESO-SYNOPTIC STRUCTURE OF SEPTEMBER 1-2 DISTURBANCE

4.1 Introduction

One of the central problems of tropical meteorology is the interaction between synoptic scale systems and processes on the convective scale. The most significant interactions of this type take place in organized disturbances in which large convective clouds are concentrated. Riehl and Malkus (1958), in their study of the energy budget of the equatorial trough zone, state that the synoptic-scale disturbances account for the bulk of the vertical energy transport, and that the individual cumulonimbus towers themselves can accomplish most of the required transport. They also point out that convective downdrafts are another feature for contributing to the energy transport through deep layers of the atmosphere, and also enhance the energy transfer from sea to atmosphere by bringing cooler and drier air into contact with the sea surface. Zipser (1969) has presented a well-documented example of this energy transport by downdrafts over the Western Pacific.

In order to incorporate the structure and organization of convective clouds, mesosystems or downdrafts in land disturbances, a combination of synoptic, aircraft, rainfall and echo data were used for studies of the meso-synoptic scale interaction. One specific, well documented example of the heaviest precipitation event of the summer of 1972 over Venezuela is presented here.

4.2 The 1-2 September 1972 Disturbance

The first direct indication of this disturbance in the experimental area was the onset of heavy rain showers at Carrizal at 2300 LST of September 1. The showery conditions changed to steady rain for several hours before ending at 1130 LST of September 2 with a total rainfall of

89.5 mm at Carrizal. What made the system interesting was the onset of westerly and southerly winds at low levels at 1833 LST. During the entire summer, westerly winds which persisted for several hours were present only three times at the lowest levels (they occurred on June 19, August 25 and from September 1 to 5). On September 1, the mean half hour surface wind reached 6 m/s from the west at Carrizal and the 2357 LST rawinsonde measured a west wind of 11 m/s at a height of 1540 m, decreasing with height thereafter.

Synoptic data were used to produce a track and life history of this rather strong disturbance. As subsequent documentation suggests, the system underwent intensification and expansion between 1451-2357 LST on September 1. It is probably just past its peak intensity when it reaches Carrizal sometime after 2400 LST on September 1, and dissipates after noon of September 2. The structure of the system through its life cycle will now be examined.

4.3 Synoptic Situation

From examination of the synoptic charts (analyzed by Dr. H. Riehl) for the disturbance period (1-2 September), synoptic conditions could be identified.

Figures 4.1, 4.2, and 4.3 show the isobaric pattern at 1200 Z (0800 LST) on September 1 for 200 mb, 500 mb and 850 mb, respectively. The 200 mb pattern shows a low pressure dominating the Caribbean region while a high pressure region is located over the central and west part of Venezuela. The 500 mb chart shows a trough extending from the Caribbean to the north central part of Venezuela. The 850 mb charts show similar patterns to the 500 mb.

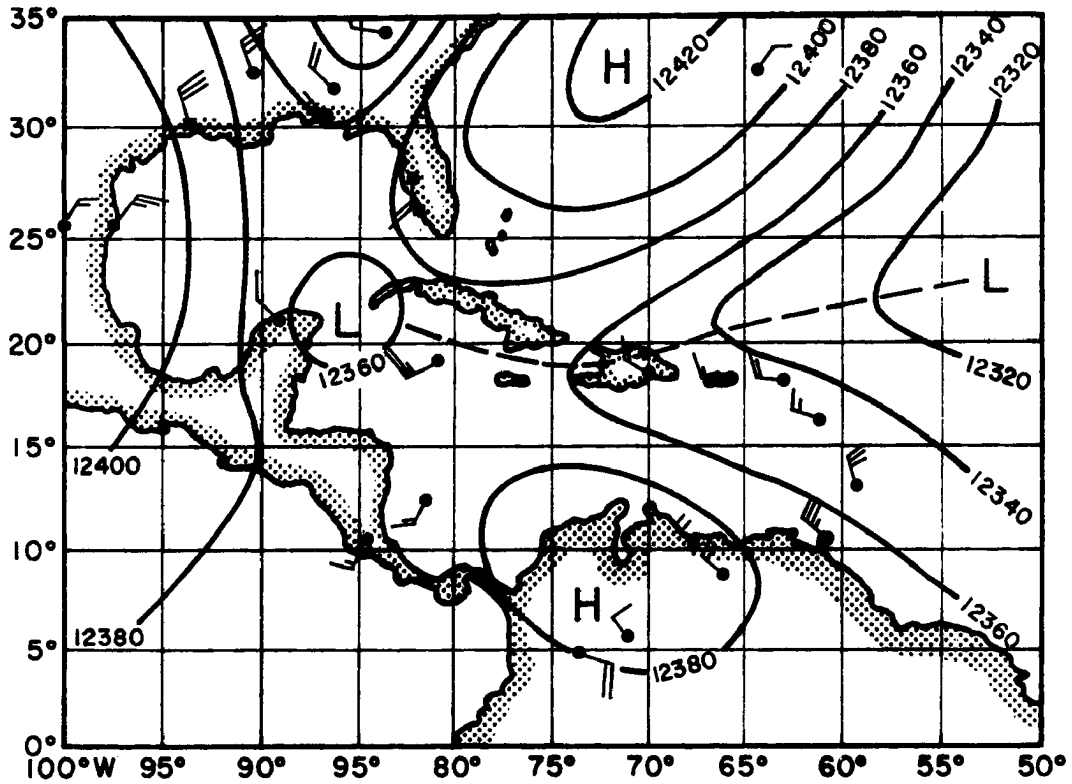


Figure 4.1 Height pattern on 200 mb surface at 1200 Z (0800 LST) September 1, 1972.

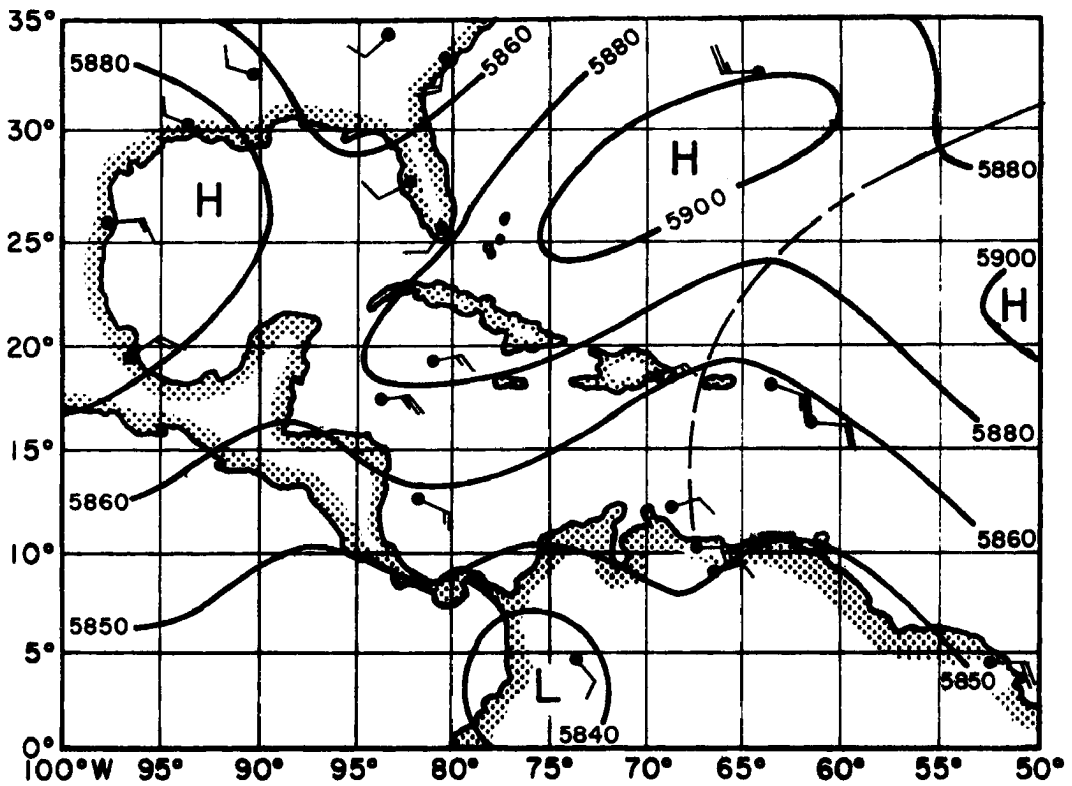


Figure 4.2 Height pattern on 500 mb surface at 1200 Z (0800 LST) September 1, 1972.

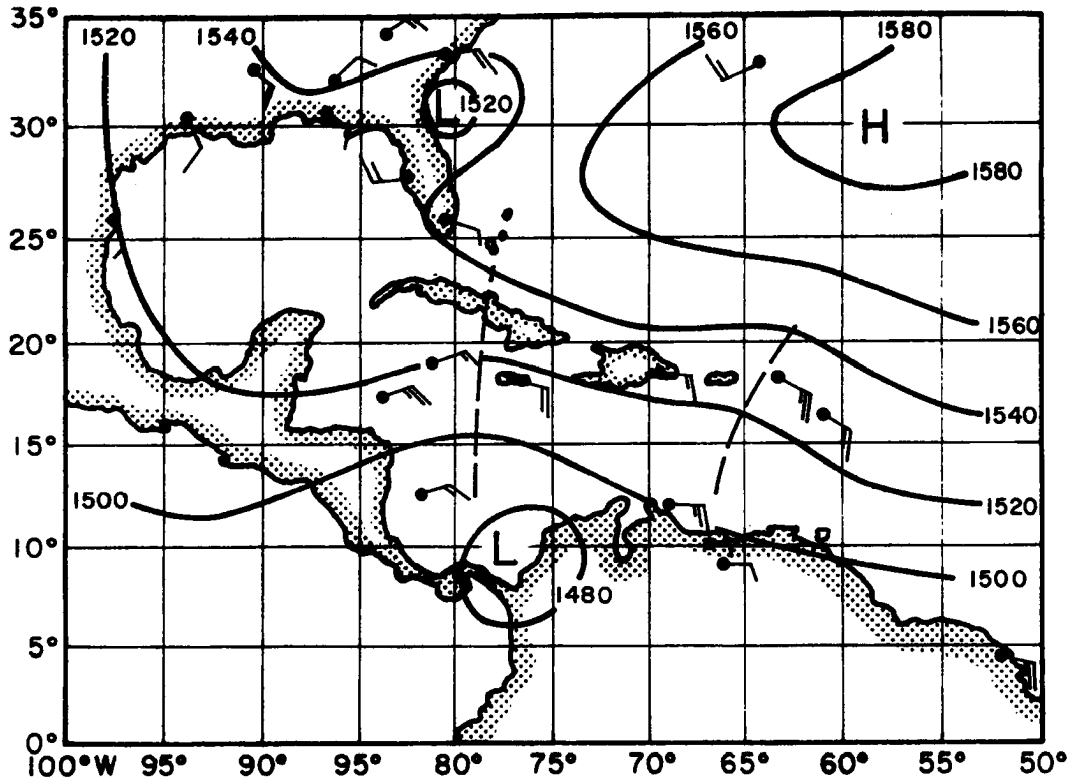


Figure 4.3 Height pattern on 850 mb surface at 1200 Z (0800 LST) September 1, 1972.

Figures 4.4, 4.5 and 4.6 show the isobaric pattern at 0000Z (2000 LST) on September 1 for 200 mb, 500 mb and 850 mb, respectively. At 200 mb, a trough can be seen extending from mid-Atlantic with an intrusion over the northeastern part of South America approaching the eastern part of Venezuela. The 500 mb chart shows a sequence of troughs, a ridge and a trough in the east central and western part of Venezuela, respectively. The synoptic pattern at 850 mb is very similar to 500 mb.

Figures 4.7, 4.8 and 4.9 show the isobaric pattern at 1200 Z (0800 LST) on September 2 for the same levels as above. At 200 mb a trough can be seen extending from the mid-Atlantic to the southwest over Venezuela. The 500 mb chart shows two troughs associated with a low pressure area centered over the radar site. At 850 mb, a trough associated with a low pressure area over the Panama Canal has just passed over the radar site. This low pressure can be seen at 500 mb. The duration, intensity, size and lack of propagation of the storms observed during the disturbed period can be attributed to this "special" synoptic situation.

4.4 Storm Structure

From the echo-rainfall composite charts (see Chapter 3, subsection 3.2.2), two storms were present during 1-2 September. These storms were the largest observed during the summer experimental period. Storm 109 at its peak (0730 LST) had an area of about 11,655 km², with an additional area beyond radar range as can be seen from the daily isoyect map for September 2. Storm 108 began at 2115 LST on September 1 and continued until 0300 LST on the second of September. Forty minutes later, storm 109 began and lasted until 1415 LST the same day.

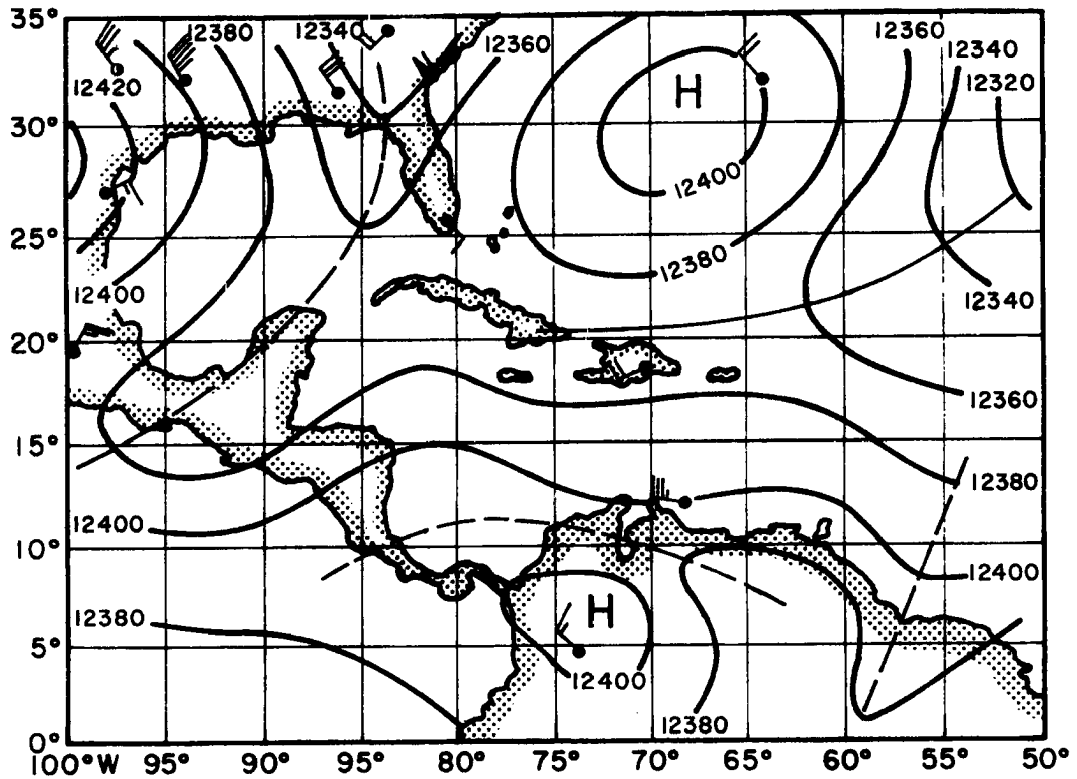


Figure 4.4 Height pattern on 200 mb surface at 0000 Z (2000 LST) September 1, 1972

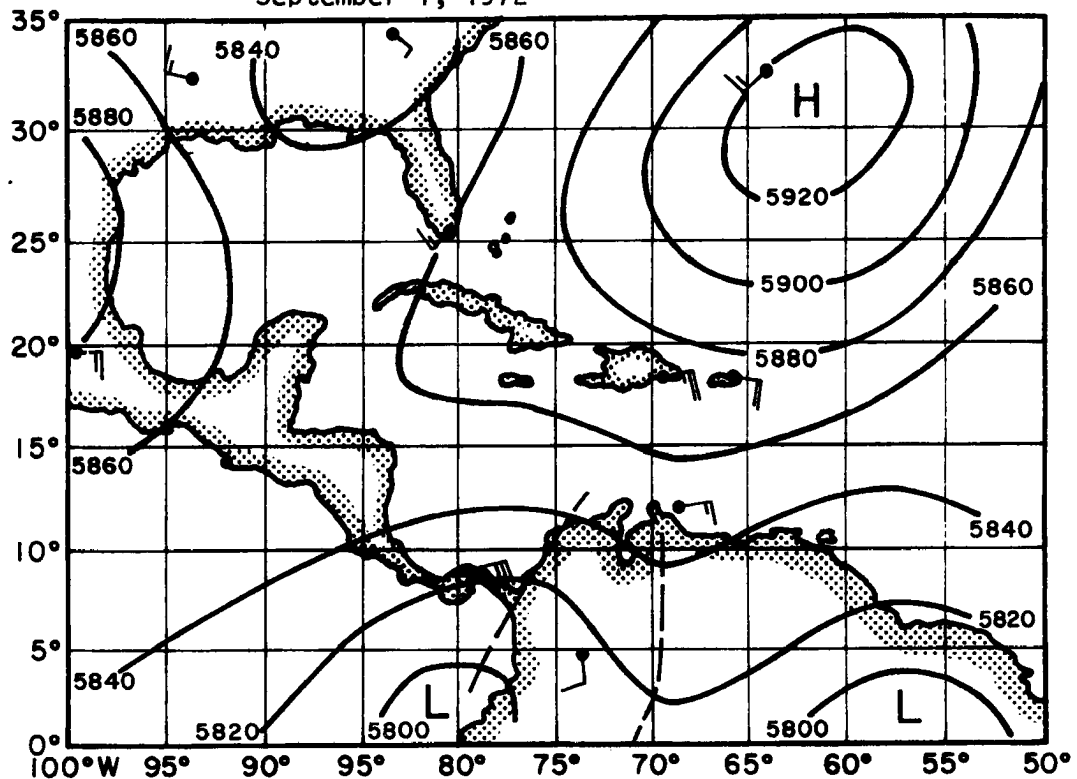


Figure 4.5 Height pattern on 500 mb surface at 0000Z (2000 LST) September 1, 1972.

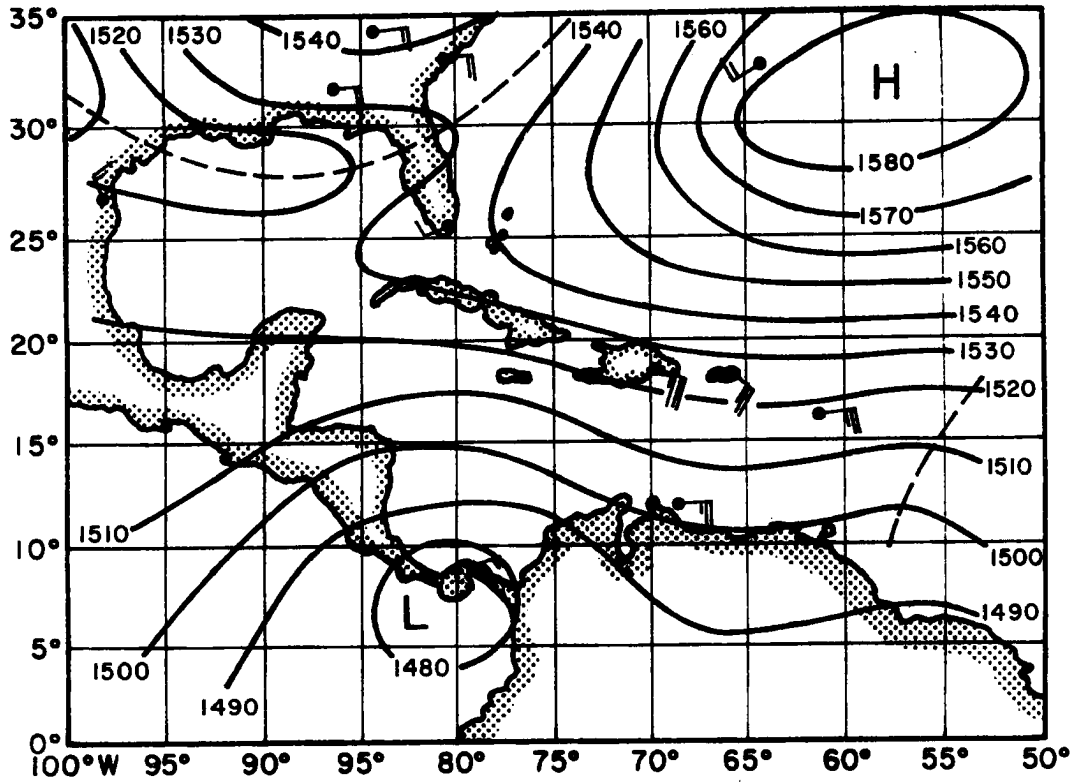


Figure 4.6 Height pattern on 850 mb surface at 0000Z (2000 LST) September 1, 1972.

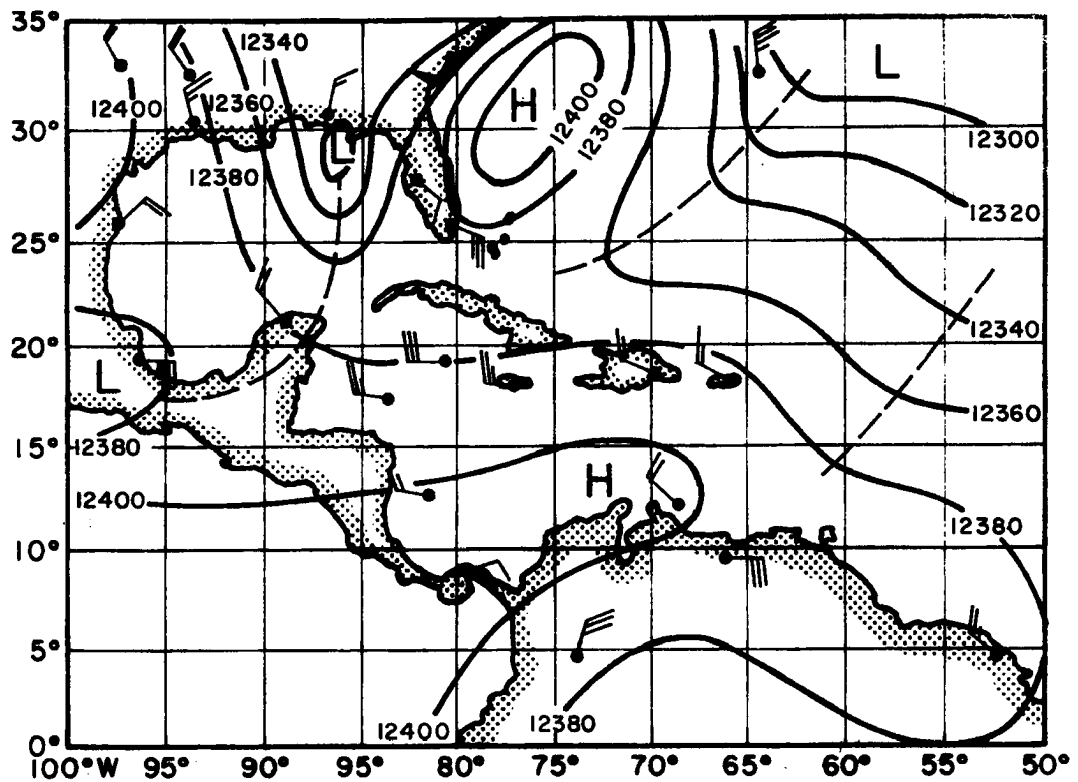


Figure 4.7 Height pattern on 200 mb surface at 1200 Z (0800 LST) September 2, 1972.

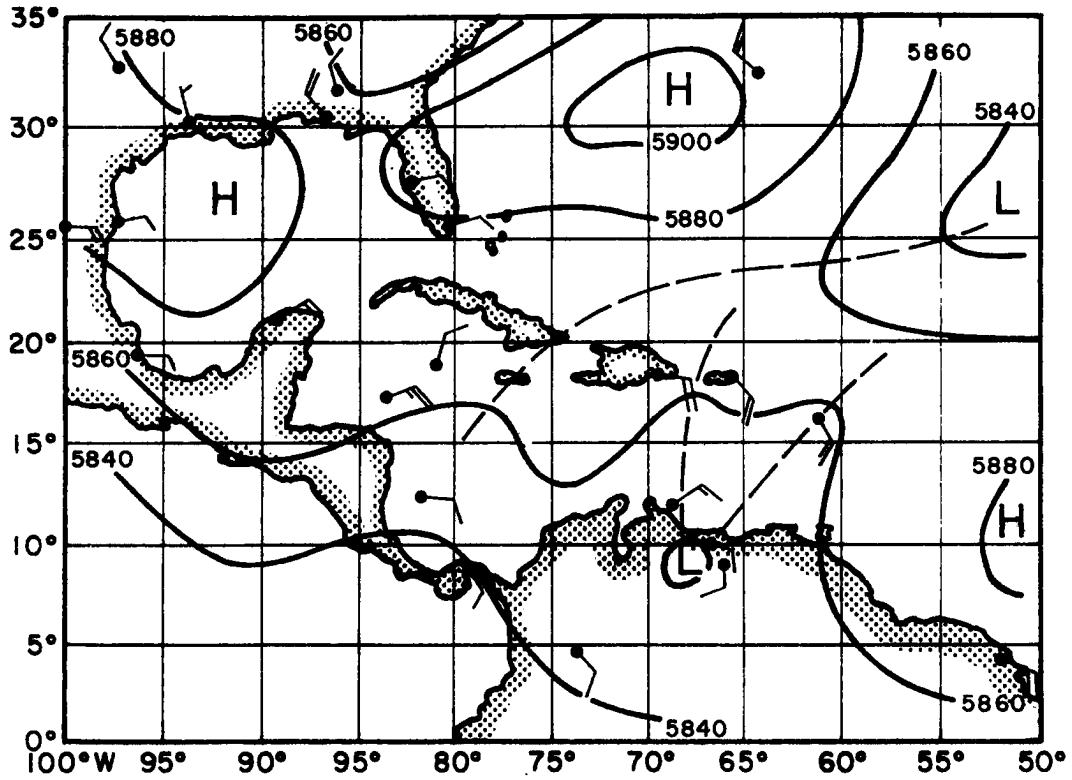


Figure 4.8 Height pattern on 500 mb surface at 1200 Z (0800 LST) September 2, 1972.

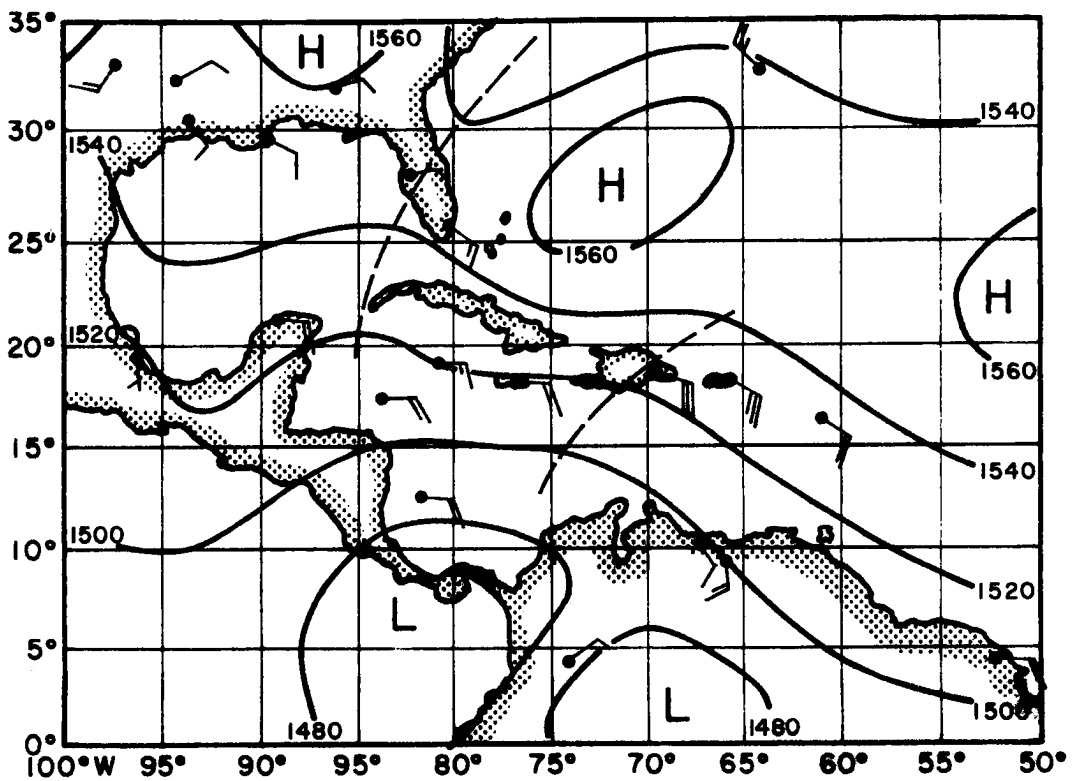


Figure 4.9 Height pattern on 850 mb surface at 1200 Z (0800 LST) September 2, 1972.

4.5 Sub-Cloud and Upper Layer Winds

4.5.1 Sub-Cloud Layer Winds

A sequence of events at the Carrizal station is given in Fig. 4.10a,b & c. Prior to 2100 LST on September 1, or during the rapid intensification of the disturbance, the surface winds at Carrizal have a component from the west. Serial rawinsonde ascents verify that the winds in the lowest 1000 m have this west component, which rapidly changes to the south and disappears with height. The wind shift to the southwest at Carrizal coincides with the time location of the beginning of storm 108. The vertical wind structure at Carrizal is illustrated by Fig.4.11 (time-cross section).

4.5.2 Upper Winds

The low westerly winds disappear at 850 mb, moderate southerly winds occupy the 850-750 mb layer, easterly winds exist at the 750-350 mb. Above 300 mb, the winds are variable but they are mainly out of the northeast.

During their active period the storms 108 and 109 moved westward at 5.2 m/s^{-1} and 3.1 m/s^{-1} respectively, giving a relative wind at low levels into the system from the west.

4.6 Structure of the Rain-Cooled Air

4.6.1 Structure Before Rain Period on September 1

Prior to the major development, a number of mesoscale and smaller cloud systems existed within a zone about 200 km wide extending along a north-south, east-west axis through Carrizal. The active convective clouds reach heights of 16 km with a life time of 2.5 hours. There is a significant change in the large scale thermodynamic structure on September 1 from 1000 to 2357 LST at Carrizal (see Fig.3.3a subsection 3.2.1).

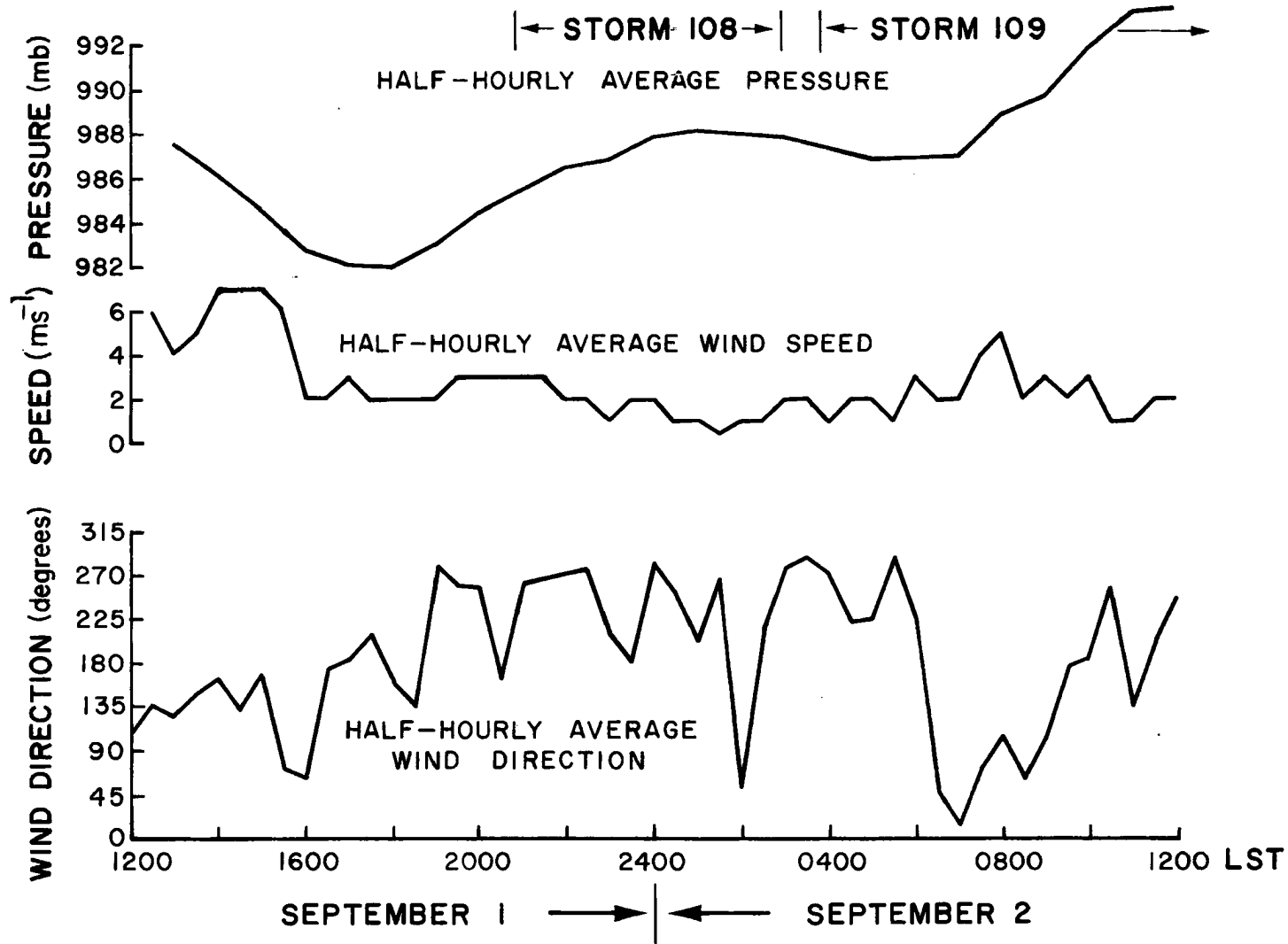


Figure 4.10a Half hourly average values of wind (direction and speed) and pressure at the surface at Carrizal from 1200 LST (September 1) to 1200 LST (September 2).

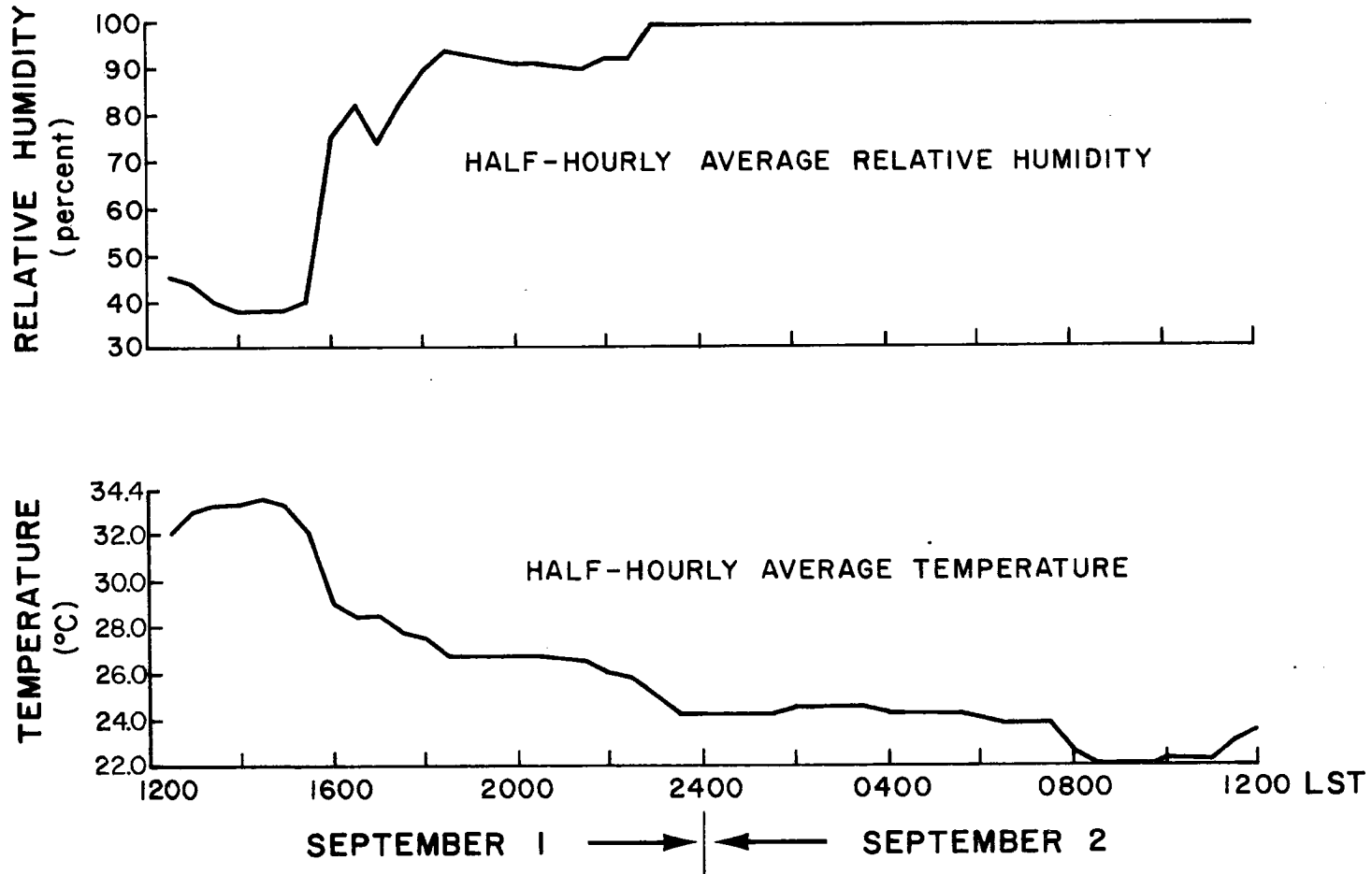


Figure 4.10b Half hourly average values of temperature and relative humidity at the surface at Carrizal from 1200 LST (September 1) to 1200 LST (September 2).

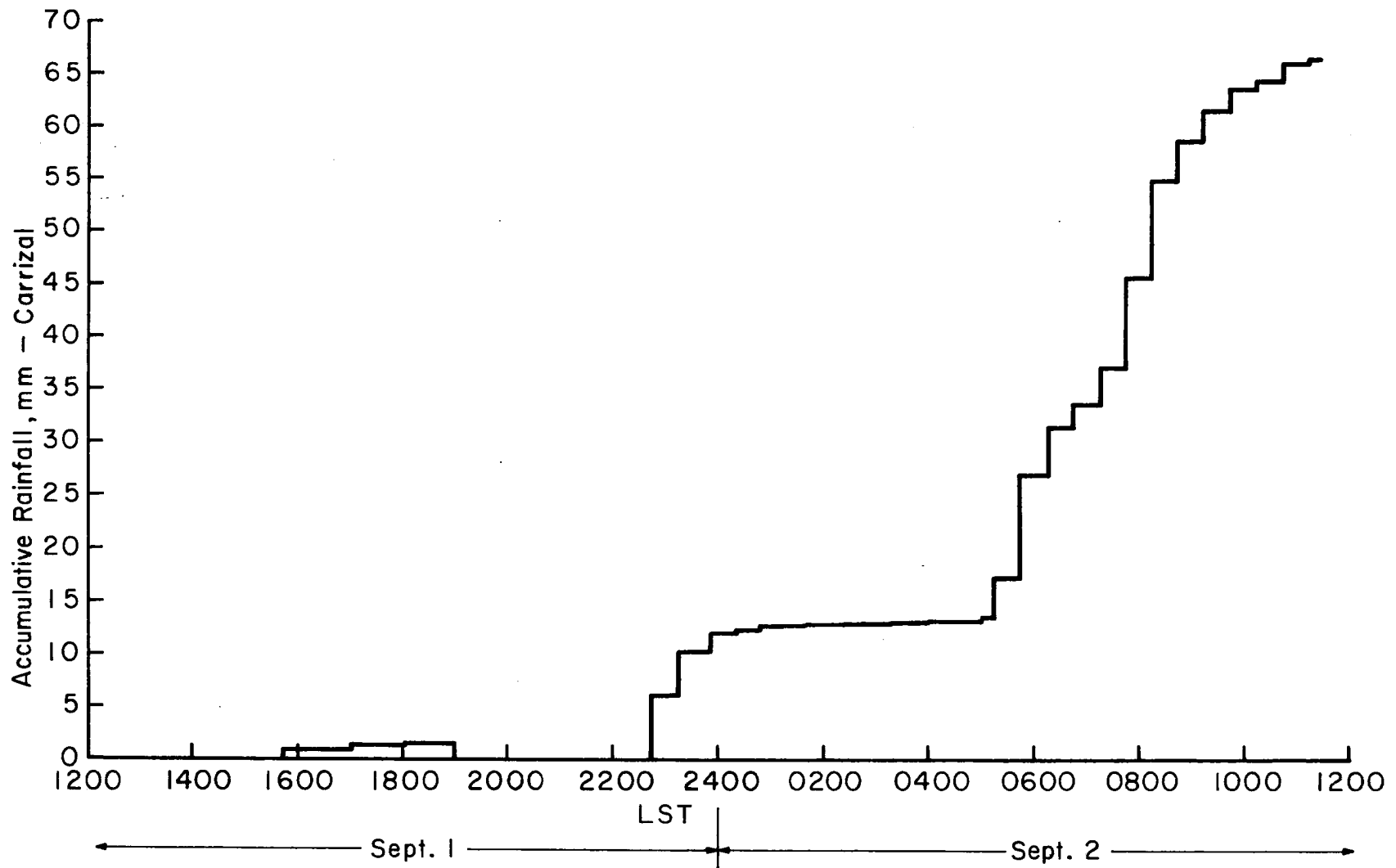


Figure 4.10c Accumulative rainfall at the surface at Carrizal from 1200 LST (Sept. 1) to 1200 LST (Sept. 2).

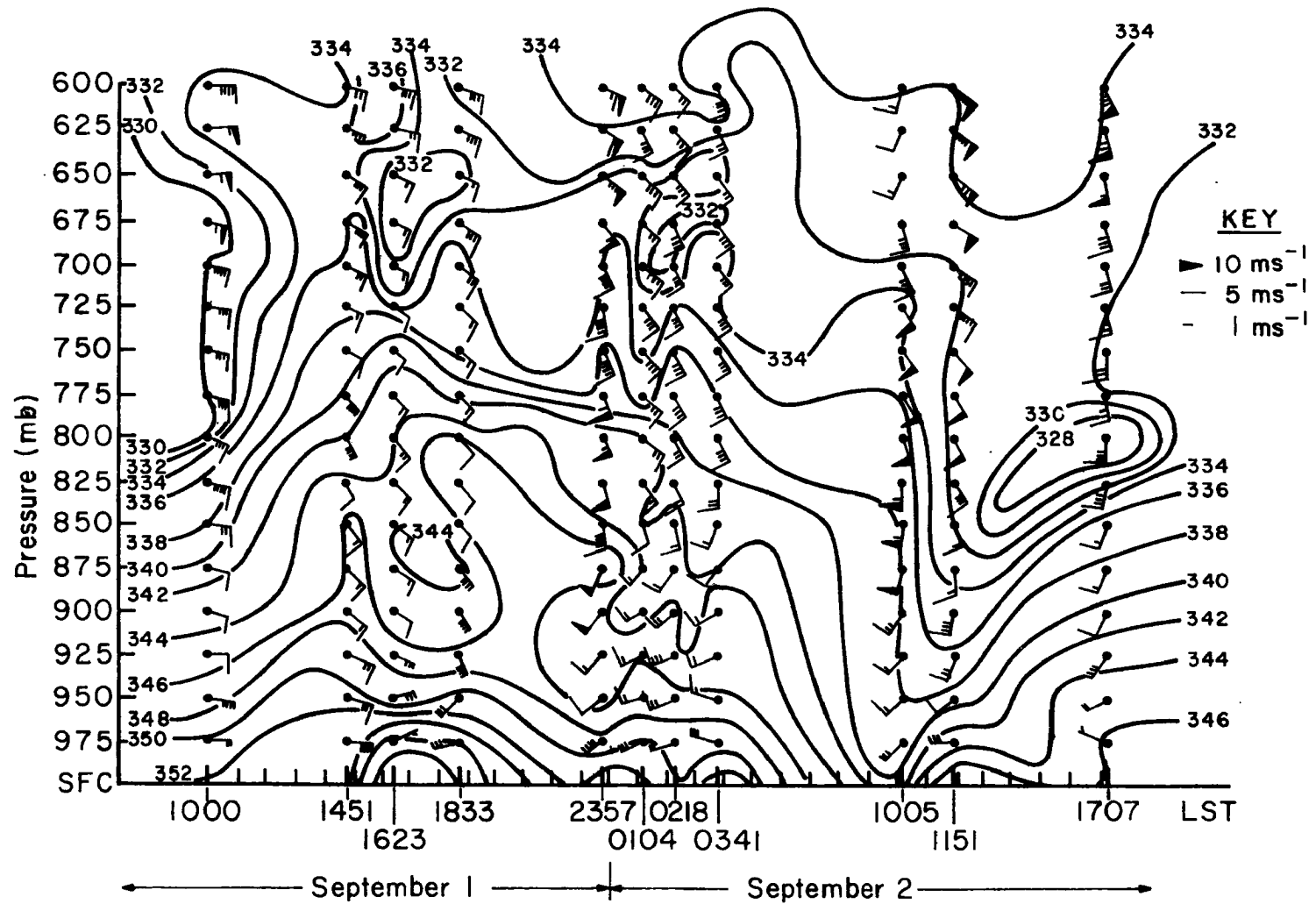


Figure 4.11 Time cross-section at Carrizal from 1000 LST (September 1) to 1707 LST (September 2).

It is believed that the systems present prior to 2115 LST were growing and dying in a different environment from that of the system which developed at 2357 LST (storm 108).

The research aircraft made a cloverleaf pattern around Carrizal through this zone of the convective system from 1420 to 1745 LST. A portion of the flight data, consisting of streamline analysis and isopleths of specific humidity along four legs, at an altitude of 1540 m, is presented in Fig. 3.15. From that figure, the following features are noted:

- i) A large variability in the direction of the wind although a general southeast circulation is predominant.
- ii) Low values in the velocity of the wind.
- iii) Increase in the specific humidity with time.
- iv) Warm wet atmosphere with a θ_e of 348°K and a θ of 307°K. The above features correspond to the legs mentioned above (from 1635 to 1745 LST).

4.6.2 Structure After the Rainy Period on September 2

On September 2, the research aircraft flew from 1221 to 1646 LST through the east-west trough centered just south of Maracay (Fig.2.1) by flying north-south runs at various levels between Cata (10°50'N -67°00'W) on the coast line and San Fernando de Apure (SR) (7°54'N - 67°25'W) (see Fig. 4.12).

At SR, the flight proceeded three minutes further south and reversed direction for a wind check northbound at 800 m. Then a climb to 1500 m was made before leaving SR northbound to Cata. At Cata, at 1500 m, the flight proceeded north for about 1-2 minutes, then reversed and climbed

en route to 2900 m. This altitude was held all the way from just south of Cata to SR. At SR, a descent was made to 1500 m, reached just prior to starting northbound to "El Libertador" for termination (the tape ran out shortly before reaching "El Libertador" near the end of the mission).

From this flight, the following features can be noted:

At 720 mb,

- i) The wind was mainly from the south.
- ii) Dry atmosphere with a θ_e of 338°K and a θ of 312°K.

At 840 mb,

- i) The wind was mainly from the south.
- ii) Cool, dry atmosphere with a θ_e of 337°K and a θ of 306°K.

At 938 mb,

- i) The wind was from the southwest and weaker than the wind at 720 mb, indicating a wind shear and a cyclonic wind shift.
- ii) Cool, wet conditions, with a θ_e of 344°K and a θ of 302°K.

These values agree very well with those given by the time-cross section. The above features indicate the extension of the downdraft air (see below) and confirming the events thought to occur from the time-cross section. The large dimensions in space are also confirmed by the above chart.

4.7 The Large Scale Downdraft and Its Associated Convective Systems

The clearest evidence of the rain-cooled nature of the low level air behind the storms 108 and 109 comes from the time-cross section of Carrizal rawinsonde observations (Fig.4.11) and from the plotted values of θ and θ_e at 1451 LST of September 1, and at 1005 LST of September 2, in a tephigram (Fig.4.13). The rain-cooled air arrives at Carrizal at 1005 LST

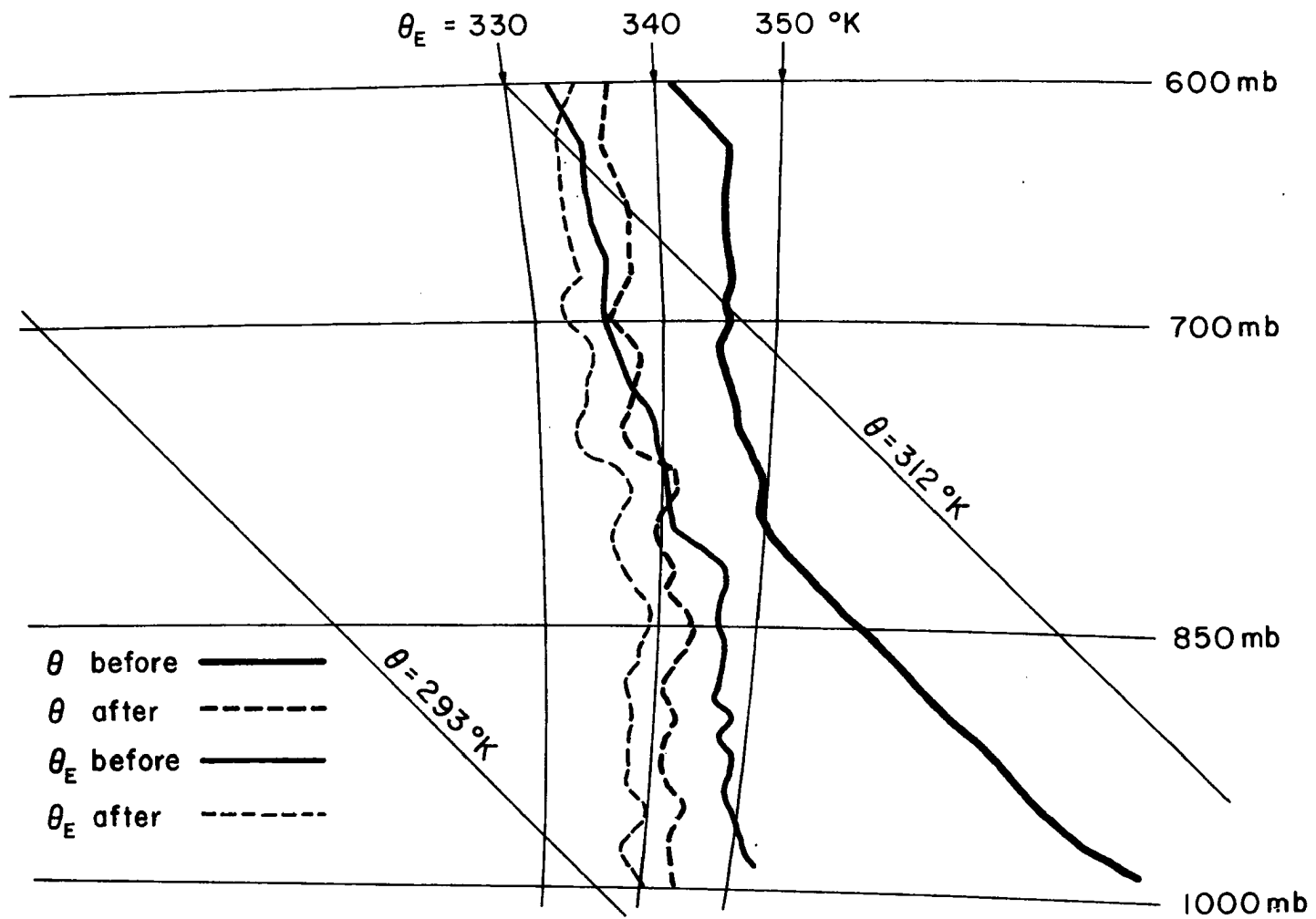


Figure 4.13 Vertical and time variation of θ and θ_E before and after the September 1-2 mesosynoptic disturbance in a tephigram.

on September 2. This sounding with those at 1151 and 1707 LST show the strong southeasterly wind below 750 mb. These winds are associated with a remarkable low equivalent potential temperature (θ_e). The 330° isotherm extends below 825 mb. The θ_e distribution prior to the direct influence of the disturbance is about normal for the tropical atmosphere; a high θ_e region in the low troposphere, with a minimum of θ_e in the middle troposphere. It appears that air descends in an unsaturated downdraft to the low troposphere, where pressure forces (note the pressure rise at Carrizal (Fig 4.10a) as the cool air arrives) accelerated it out of the rain area.

An illustration of the above features can be seen in the tephigram (Fig.4.13). It shows the variation of the potential temperature and the equivalent potential temperature before precipitation starts (1451 LST on September 1) and after the main disturbance (1005 LST on September 2).

The potential temperature shows a definite cooling below 500 mb. The large cooling near the surface (13.4°K) reflects the evaporation of precipitation falling through the sub-cloud layer as well as the convectively induced downdraft of cooler air. The changes in the profile represent changes in the stability of the atmosphere. Precipitating convection acts to stabilize the initially unstable layer below 700 mb. The entire layer below 700 mb is much more stable after precipitation than it was before (see also, the half-hourly average temperature at the surface). Since potential temperature and saturation equivalent potential temperature are both functions of temperature and pressure only, a change in temperature at a specified pressure level can be expected to produce similar changes in θ_{es} and θ . Changes in θ_{es} are an amplification of the changes in θ , thus, the profile of θ_{es} has not been plotted.

The equivalent potential temperature shows a decrease below 610 mb and a net decrease at surface of 13.0°K. The observed decrease results from a sinking of air in downdrafts from higher levels, where θ_e is lower. The structural changes above 610 mb result from the transport of high θ_e air from near the surface into the middle troposphere. This air (which is also very moist) mixes with the relatively low θ_e air aloft causing a net increase in θ_e (and moisture content). The moisture increase just above the surface is due, largely, to the evaporation of precipitation from the surface (see the half-hourly average relative humidity at surface). Whether the sinking occurred in convective scale downdrafts or by larger scale sinking under raining middle cloud decks, or both, is not certain. Strong sinking in the rain-cooled air is consistent with many other observations. All radar echoes disappear from the scope at Carrizal by 1400 LST on 2 September and after that not one cumulus cloud could be seen until 1600 LST when some very low cumulus began developing. This was confirmed by the aircraft mission. This large-scale downdraft is very similar to that reported by Zipser (1969) during the Line Islands Experiment.

It was mentioned in section 4.7.1 that the relative small mesoscale systems reported by the aircraft on September 1, prior to storm 108, were growing and dying in different environments so that the large scale and long duration of the downdraft system suggest that a mechanism was operating which permitted unsaturated, rain-cooled, rapidly sinking air, to develop on a larger scale in space and time, than the convective systems present before 2115 LST around Carrizal.

A structure of the system that seems to meet these requirements is proposed next.

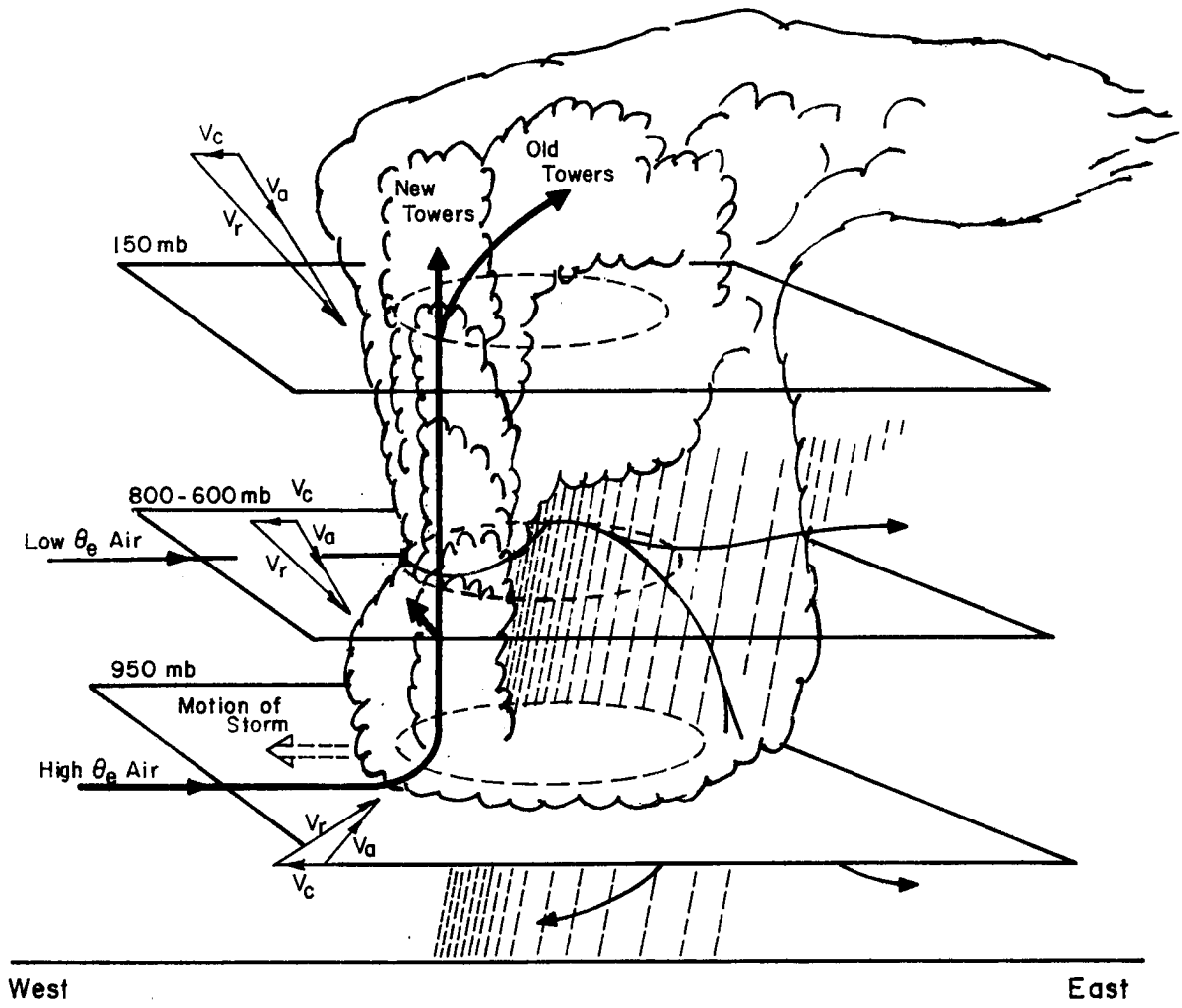
In this organized convection situation, the wind veers with height, as in Fig. 4.14. The figure shows both the actual wind V_a and the wind relative to the cloud V_r . The motion of the ambient air relative to the cloud is into the left flank in lower levels, and away from that flank in upper levels. This might favor growth on that flank (Fig. 4.14) and help explain the drift of the storm toward the left. This explanation is consistent because it provides for the growth of new and vigorous convection on the left side.

Although very slowly, the convective clouds associated with storms 108 and 109 moved westward. The air with high θ_e , forming active cumulonimbus towers must have positive buoyancy and must come from the subcloud layer. Note that the environment winds were from south-southwest with a speed of about $8-10 \text{ m s}^{-1}$, and had relative winds with a westerly component of about $10-12 \text{ m s}^{-1}$. These values indicate the quasi-non-propagating nature of the above storms. Figure 3.8 shows storms 108 and 109 at 2245-0645 LST respectively, close to their time of maximum area.

It is of interest to note that both the beginning and the end of 108 and 109 were recorded on film and at no time did the system travel beyond radar range.

The mentioned air with high θ_e , having risen in cumulonimbus towers, passes out in the anvil or in associated middle and upper clouds. Some evidence of this feature appears on the Carrizal time-cross section above 500 mb after the arrival of the downdraft at low levels.

The associated low θ_e values at 1005 LST on September 2 compared with the high θ_e values at 1451 on September 1, indicate considerable vertical exchange in the environment has taken place.



V_r = Relative wind
 V_a = Actual wind
 V_c = Mean motion of the storm

Figure 4.14 Schematic structure of cloud system illustrating the mechanism of production of large scale downdrafts.

The air which takes part in the downdraft comes from the 800-600 mb layer where θ_e is lower and the environment winds are from south-southeast at $8-10 \text{ m s}^{-1}$; this gives a wind relative to the system from south-southwest at $7-9 \text{ m s}^{-1}$. This air can be entrained into individual convective towers and form downdrafts on a convective scale or mesoscale as well as diluting the buoyancy of the towers. It can also flow freely under the raining anvil on a large scale and sink in the direct circulation to the lower troposphere, remaining highly unsaturated as suggested by Zipser (1969). This low θ_e air can arrive at a position under the anvil either directly or by passing around individual cumulonimbus towers.

5. SUMMARY AND CONCLUSIONS

The aim of this study was to describe the mesoscale structure of the tropical sub-cloud layer for undisturbed and disturbed conditions. Of the six days selected, four were characterized as undisturbed and two as disturbed. The data used in order to obtain some insight into the mesoscale structure of the sub-cloud layer consisted mainly of aircraft, radar and sounding data and a network of raingauges extending 60 km around the experimental area. Conventional data such as synoptic and pilot balloon information were also used. The above combination of data sources allowed the investigation of mesoscale disturbances present during the days chosen.

In general, all storms present during the time period of study traveled from east to west and showed boundary layer changes in temperature and equivalent potential temperature (downdrafts).

The aircraft measurements show that a suitably equipped aircraft can make wind measurements of good quality near the top of the sub-cloud layer, especially after the appropriate corrections were applied. In addition, aircraft have the distinct advantage of being both highly mobile and flexible, for example, aircraft are not restricted to along-wind sampling as are fixed position systems. However, there were limitations to the aircraft measurements because the data used were based on minute averages, which reduced the horizontal resolution.

Horizontal divergences calculated on undisturbed days could only be determined at one level, i.e. 850 mb, but the values obtained using the Queen Air, even after applying wind corrections, were as small as the errors in the measurement. It was also doubtful if the vorticity estimates for the same days were significant. However, these results do give good observational support to the applied corrections of the wind in the sense

that small values of divergences on the order of $5 \times 10^{-6} \text{ s}^{-1}$ reflect the high accuracy of the corrected winds. Although the above measured divergence values are not significant considering the residual errors in the winds; clearly during undisturbed periods the low level divergence on this scale is small (the residual winds errors would probably give errors in the divergence for a triangle on the order of 10^{-5} s^{-1}). In spite of the above remarks, it is the author's belief that large values of convergence may be found in the lower troposphere in tropical regions only when disturbed conditions are present, or in the vicinity of large cumulonimbus clouds.

From measurements taken by the aircraft near the top of the subcloud layer, it was found that in cloudy areas, the wind, mixing ratio and temperature are well correlated. An interesting conclusion reached was that large wind variations occur with cloudy areas, simultaneously with an increase in the mixing ratio and equivalent potential temperature as well as a decrease in the potential temperature. Presumably on scales $\lesssim 20 \text{ km}$, convergence values must be much larger than those quoted above. The mixing ratio variations were such that they described "wet" and "dry" regions, the time interval between them varies from 5 to 7 minutes (20 to 30 kms horizontal distance on the ground).

The variability of the potential temperature, equivalent potential temperature, mixing ratio and wind (direction and speed) determined for the top of the sub-cloud layer is probably representative of the mesoscale patterns in the tropics. They also indicate that caution is needed in interpreting a single rawinsonde sounding as representative of a large area.

Results derived from cloud-scale study give some indication of the varied and complex processes which occur under and through clouds and rain. They show that the associated variations in temperature, humidity and wind are significant and measurable even in relatively undisturbed conditions.

The results of 850 mb level flights support the hypothesis that coupling between the cloud layer and the sub-cloud layer is more common than was previously believed for undisturbed atmospheric states, and that it becomes more frequent and more intense for disturbed states. The fact that the mechanism responsible for this coupling is not observed more often may be because the subsiding air rarely penetrates the full depth of the sub-cloud layer. This is not the case during disturbances, such as was shown from the studied meso-synoptic disturbance on September 1-2. This well documented example of the heaviest precipitation event of the summer of 1972 clearly shows dramatic vertical transports through cloud-base. The duration, intensity size, and lack of propagation of the storms observed during the above two days can be attributed to the "special" synoptic situation present. Of significance was the change in the wind (direction and magnitude) from undisturbed to disturbed days.

Results from the study of the above disturbance indicate the transformation of the dry sub-cloud layer by precipitation; and its stabilization, caused by the low level cooling and the simultaneous reduction in equivalent potential temperature by deep convective downdrafts.

A structure of the system which permitted unsaturated, rain cooled, rapidly sinking air to develop on a larger scale in space and time, than the convective systems present before heavy precipitation starts, was also proposed. The schematic structure of the cloud system illustrating the mechanism of the production of a large scale downdraft as well as movements of

storms (Fig. 4.14) showed the main features of the above mechanism at lower, middle and upper levels. The explanation proposed (to it) is consistent because it provides for the growth of new and vigorous convection on the left side where severe weather tended to be concentrated during the meso-synoptic disturbance on September 1-2, 1972, over Carrizal, Venezuela. The system appears to have many similarities with that documented by Zipser (1969) over the Western Pacific.

REFERENCES

- Arakawa, A. and W. Schubert, 1974: Interaction of a Cumulus Cloud Ensemble with the Large-Scale Environment. Part I. J. Atmos. Sci., 31, pp. 674-701.
- Ball, F. K., 1960: Energy Changes Involved in Disturbing a Dry Atmosphere. Quart. J. Roy. Meteor. Soc., 86, pp. 483-494.
- Betts, A. K., 1971: Relating the Non-Precipitating Convective Boundary Layer to the Large-Scale Motion Field. Presented at the 52nd Annual Joint Meeting of the AGU and AMS.
- _____, 1973a: Non-Precipitating Cumulus Convection and Its Parameterization. Quart. J. Roy. Meteor. Soc., 99, pp. 178-196.
- _____, 1973b: A Composite Mesoscale Cumulonimbus Budget. J. Atmos. Sci., 30, pp. 597-610.
- _____, F. J. Dugan, and R. W. Grover, 1974: Residual Errors of the VIZ Radiosonde Hygristor as Deduced from Observations on Subcloud Layer Structure. Bull. Amer. Meteor. Soc.
- _____, 1974: The Scientific Basis and Objectives of the U.S. Convection Subprogramme for the GATE. Bull. Amer. Meteor. Soc., 55, pp. 304-313.
- _____, and M.A. Stevens, 1974: Rainfall and Radar Statistics. Venezuelan International Meteorological and Hydrological Experiment 1972. Atmospheric Science Report. Colorado State University, 152 pp.
- _____, 1974: Thermodynamic Classification of Tropical Convective Soundings. Mon. Wea. Rev., 102, pp. 760-764.
- Carson, D. J., 1973: The Development of a Dry Inversion Capped Convectively Unstable Boundary Layer. Quart. J. Roy. Meteor. Soc., 99, pp. 450-467.
- Deardorff, J.W., 1972: Parameterization of the Planetary Boundary Layer for Use in General Circulation Models. Mon. Wea. Rev., 100, pp. 93-106.
- Dugan, F. J., 1973: The Thermodynamic Structure of the Cumulus Subcloud Layer. Atmospheric Science Paper No. 205. Colorado State University, 97 pages.
- Friedman, H. A., R. Merlin, and H.W. Davis, 1969: The ESSA Research Flight Facility: Data Processing Procedures. ESSA Tech. Report ERL 132-RFF2, Research Labs., Environmental Science Services Admin., U.S. Department of Commerce.
- Fujita, T., 1963: Analytical Mesometeorology: A Review. In Severe Local Storms. Amer. Meteor. Soc., Boston, Massachusetts, pp. 77-125.

REFERENCES - Continued

- Fujita, T., 1950: Microanalytical Study of Thunder-Nose. Geophys. Mag. Tokyo, 22, pp. 78-88.
- _____, 1951: Microanalytical Study of Cold Front. Geophys. Mag. Tokyo, 22, pp. 237-277.
- Garstang, M. and A. K. Betts, 1974: A Review of the Tropical Boundary Layer and Cumulus Convection: Structure, Parameterization, and Modeling. Bull. Amer. Meteor. Soc., 55, pp. 1195.
- Grant, D. R., 1965: Some Aspects of Convection as Measured from Aircraft. Quart. J. Roy. Meteor. Soc., 91, pp. 268-281.
- Grover, R. W., 1974: Characteristics of Tropical Squall-Lines Over Venezuela. Colorado State University, Atmospheric Science Paper No. 228, 79 pages.
- Ligda, M.G.H., 1951: Radar Storm Observation. Compendium of Meteorology, Boston, Amer. Meteor. Soc., pp. 1265-1282.
- Lilly, D. K., 1968: Models of Cloud Topped Mixed Layers Under a Strong Inversion. Quart. J. Roy. Meteor. Soc., 94, pp. 292-309.
- Newton, C. W., 1963: Dynamics of Severe Convective Storms. In Severe Local Storms. Amer. Meteor. Soc., Boston, Mass., pp. 33-58.
- Pennell, W. T., and M. A. LeMone, 1974: An Experimental Study of Turbulence Structure in the Fair-Weather Trade Wind Boundary Layer. J. Atmos. Sci., 31, pp. 374-382.
- Riehl, H., and J.S. Malkus, 1958: On the Heat Balance in the Equatorial Trough Zone. Geophysics, 6, pp. 503-538.
- _____, and A. K. Betts, 1972: Humidity Observations with the 1972 U.S. Radiosonde Instrument. Bull. Amer. Meteor. Soc., 53, pp. 887-888.
- Seguin, W. R., 1972: A Study of the Tropical Oceanic Sub-Cloud Layer. Ph.D. Dissertation. Dept. of Meteorology, Florida State University, 221 pp.
- Tennekes, H., 1973: A Model for the Dynamics of the Inversion Above a Convective Boundary Layer. J. Atmos. Sci., 30, pp. 558-567.
- Tepper, M., 1959: Mesometeorology - The Link Between Macroscale Atmospheric Motions and Local Weather. Bull. Amer. Meteor. Soc., 40, pp. 56-72.
- Warner, J., and J.W. Telford, 1967: Convection Below Cloud-Base. J. Atmos. Sci., 24, pp. 374-382.

REFERENCES - Continued

- Williams, D. T., 1948: A Surface Micro-Study of Squall Line Thunderstorms. Mon. Wea. Rev., 76, pp. 239-246.
- Zipser, E. J., 1969: The Role of Organized Unsaturated Convective Downdrafts in the Structure and Rapid Decay of an Equatorial Disturbance. J. Appl. Meteor., 8, pp. 799-814.

APPENDIX 1

The true air speed and drift angle correction determination program (written in Fortran IV Language) was used to determine the corrections applied to the true air speed vector (Tc) (i.e., the magnitude of the true air speed vector) and to the drift angle (δc) to correct the wind data measured by the Doppler system.

The analytical expressions used to determine Tc and δc in the winds program follow; see also Fig. 2.10

It should be noted that:

$$|\vec{\delta c}| \approx \delta c / 57.296 |\vec{GS}| \quad (1)$$

The direction of

$$|\vec{\delta c}| \approx TR \pm (\delta c^\circ + 90^\circ) \quad (2)$$

$$|\vec{\delta c}| > 0 \quad \text{for right error}$$

$$\delta = \delta m + \delta c \quad (3)$$

$$TR = THdg + \delta m \quad (4)$$

$$THdg = MDdg + MVAR \quad (5)$$

$$\text{from } \vec{W} = \vec{GS} - \vec{TAS}$$

we see that

$$\vec{W}_1 = \vec{GS}_1 - \vec{TAS}_1 \quad (6)$$

and

$$\vec{W}_2 = \vec{GS}_2 - \vec{TAS}_2 \quad (7)$$

$$\text{where } |\vec{TAS}| = |\vec{IAS}| \left(\frac{\rho_0}{\rho}\right)^{1/2} = |\vec{IAS}| \left(\frac{TP_0}{T_0P}\right)^{1/2}$$

W_1 can also be expressed as

$$\vec{W}_1 = (\vec{GS}_1 - \vec{TAS}_1) = (\vec{GS}_{m1} + \vec{\delta c}_1) - (\vec{TAS}_{m1} + \vec{Tc}_1) \quad (8)$$

and after rearranging the terms

$$\vec{W}_1 = (\vec{GS}_1 - \vec{TAS}_1) = (\vec{GS}_{m1} - \vec{TAS}_{m1}) + \vec{\delta c}_1 - \vec{Tc}_1 \quad (9)$$

similarly for leg "2"

$$\vec{W}_2 = (\vec{GS}_2 - \vec{TAS}_2) = (\vec{GS}_{m_2} - \vec{TAS}_{m_2}) + \vec{\delta c}_2 + \vec{Tc}_2 \quad (10)$$

from the basic assumption,

$$\vec{W}_1 = \vec{W}_2 \quad (11)$$

therefore,

$$\vec{GS}_{m_1} - \vec{TAS}_{m_1} + \vec{\delta c}_1 - \vec{Tc}_1 = \vec{GS}_{m_2} - \vec{TAS}_{m_2} + \vec{\delta c}_2 - \vec{Tc}_2 \quad (12)$$

Breaking the vectors into \vec{i} , \vec{j} components where \vec{i} and \vec{j} are orthogonal unit vectors in a rectangular cartesian coordinate system, the "u" and "v" components of the vectors are obtained.

u = component in \vec{i} direction; v = component in \vec{j} direction.

$$\vec{GS} = u_{GS} \vec{i} + v_{GS} \vec{j} \quad (13a)$$

$$\vec{Tc} = u_{Tc} \vec{i} + v_{Tc} \vec{j} \quad (13b)$$

$$\vec{TAS} = u_{TAS} \vec{i} + v_{TAS} \vec{j} \quad (13c)$$

$$\vec{\delta c} = u_{\delta c} \vec{i} + v_{\delta c} \vec{j} \quad (13d)$$

The \vec{i} component of (12) becomes

$$\vec{i} (u_{GS_{m_1}} - u_{TAS_{m_1}} + u_{\delta c_1} - u_{Tc_1} = u_{GS_{m_2}} - u_{TAS_{m_2}} + u_{\delta c_2} - u_{Tc_2}) \quad (14)$$

similarly, the \vec{j} component of (12) is given by

$$\vec{j} (v_{GS_{m_1}} - v_{TAS_{m_1}} + v_{\delta c_1} - v_{Tc_1} = v_{GS_{m_2}} - v_{TAS_{m_2}} + v_{\delta c_2} - v_{Tc_2}) \quad (15)$$

These relationships then follow.

$$u_{GS_m} = GS_m \sin (TR) \quad (16a)$$

$$v_{GS_m} = GS_m \cos (TR) \quad (16b)$$

$$u_{TAS_m} = TAS_m \sin (TH_{dg}) \quad (16c)$$

$$v_{TAS_m} = TAS_m \cos (TH_{dg}) \quad (16d)$$

$$u_{\delta c} = \delta_c / 57.296 \text{ GS}_m \cos (TR) \quad (16e)$$

$$v_{\delta c} = -\delta_c / 57.296 \text{ GS}_m \sin (TR) \quad (16f)$$

$$u_{Tc} = T_c \sin (TH_{dg}) \quad (16g)$$

and

$$v_{Tc} = T_c \cos (TH_{dg}) \quad (16h)$$

Appropriate substitution of (16a) through (16h) into (14) and (15) yields:

$$\begin{aligned} T_c [\sin (TH_{dg2}) - \sin (TH_{dg1})] + \delta_c / 57.296 [GS_{m1} \cos (TR_1) \\ - GS_{m2} \cos (TR_2)] = [GS_{m2} \sin (TR_2)] - [TAS_{m2} \sin (TH_{dg2})] \\ - [GS_{m1} \sin (TR_1)] + [TAS_{m1} \sin (TH_{dg1})] \end{aligned} \quad (17)$$

$$\begin{aligned} \text{and } T_c [\cos (TH_{dg2}) - \cos (TH_{dg1})] + \delta_c / 57.296 [GS_{m2} \sin (TR_2) - \\ GS_{m1} \sin (TR_1)] = [GS_{m2} \cos (TR_2)] - [TAS_{m2} \cos (TH_{dg2})] \\ - [GS_{m1} \cos (TR_1)] + [TAS_{m1} \cos (TH_{dg1})] \end{aligned} \quad (18)$$

Equations (17) and (18) are of the form,

$$AX + BY = C \quad (19)$$

and

$$DX + EY = F \quad (20)$$

where

$$A = [\sin (TH_{dg2}) - \sin (TH_{dg1})] \quad (21)$$

$$B = \left[\frac{GS_{m1} \cos (TR_1) - GS_{m2} \cos (TR_2)}{57.296} \right] \quad (22)$$

$$C = [GS_{m2} \sin (TR_2) - TAS_{m2} \sin (TH_{dg2}) - GS_{m1} \sin (TR_1) + \\ TAS_{m1} \sin (TH_{dg1})] \quad (23)$$

$$D = [\cos (TH_{dg2}) - \cos (TH_{dg1})] \quad (24)$$

$$E = \left[\frac{GS_{m2} \sin (TR_2) - GS_{m1} \sin (TR_1)}{57.296} \right] \quad (25)$$

$$F = [GS_{m2} \cos (TR_2) - TAS_{m2} \cos (TH_{dg2}) - GS_{m1} \cos (TR_1) + \\ TAS_{m1} \cos (TH_{dg1})] \quad (26)$$

$$X = Tc \tag{27}$$

$$Y = \delta c \tag{28}$$

and

$$\text{DELTA} = AE - BD \tag{29}$$

Solving these simultaneous equations by determinants, if

$$\text{DELTA} \neq 0$$

then

$$X = Tc = \frac{(CE - BF)}{\text{DELTA}}$$

and

$$Y = \delta c = \frac{(AF - CD)}{\text{DELTA}}$$

BIBLIOGRAPHIC DATA SHEET	1. Report No. CSU-ATSP-237	2.	3. Recipient's Accession No.
4. Title and Subtitle MESOSCALE STUDY OF THE TROPICAL SUB-CLOUD LAYER		5. Report Date September 1975	6.
7. Author's Omar Ruiz		8. Performing Organization Rept. No. CSU-ATSP-237	
9. Performing Organization Name and Address Department of Atmospheric Science Foothills Campus Colorado State University Fort Collins, Colorado 80523		10. Project/Task/Work Unit No.	
12. Sponsoring Organization Name and Address Office of Climate Dynamics National Science Foundation, GARP 1800 G. Street, N.W. Washington, D. C. 20550		11. Contract/Grant No. NSF OCD72-01406	
15. Supplementary Notes		13. Type of Report & Period Covered M.S. Thesis	
16. Abstracts - Aircraft, rawinsonde, radar, rainfall, and synoptic data acquired during the 1972 Venezuelan International Meteorological and Hydrological Experiment (VIMHEX 1972) are used to study both undisturbed and disturbed conditions. Horizontal divergences calculated from aircraft wind measurements on undisturbed days at 850 mb were as small as the errors in the measurements. In the cloudy areas penetrated by the aircraft, the wind, humidity and temperature were found well correlated and their variability are probably representative of mesoscale patterns in the tropics. The associated variations in the above parameters were significant and measureable even in relatively undisturbed conditions. They show evidence for coupling between the cloud layer and the sub-cloud layer. A meso-synoptic disturbance on Sept. 1-2, 1972 centered on the data network area is analyzed in detail. Serial rawinsondes combined with research aircraft data show dramatic vertical transports through cloud base; and the drying and stabilization of the sub-cloud layer by downdrafts. A structure of the system which permitted unsaturated, rain cooled, downdrafts, similar to that documented by Zipser, 1969, is proposed.		14.	
17. Key words and Document Analysis. 17a. Descriptors Mesoscale Structure Sub-Cloud Layer Aircraft Measurements Cumulus Convection VIMHEX 17b. Identifiers/Open-Ended Terms 17c. COSATI Field/Group			
18. Availability Statement		19. Security Class (This Report) UNCLASSIFIED	21. No. of Pages 133
		20. Security Class (This Page) UNCLASSIFIED	22. Price